Fabrication of AuPd bimetallic nanoparticles and their effects on hydrogenation reactions

José Jorge B. F. Pinto, MSci

Thesis submitted to the University of Nottingham

for the degree of Doctor of Philosophy

August, 2020

Declaration

This thesis is the result of my own investigations and is not being concurrently submitted in candidature for any degree.

Signed_____(candidate)

Date_____

Acknowledgements

Firstly, I would like to thank my supervisor Peter Licence, for taking me into his group, mostly when he was not my main supervisor from the beginning. Thank you for all the insightful meetings and support. An immense acknowledgement for Jesum Alves Fernandes, that started here as a postdoc and I had the pleasure of seeing him become a fellow and my supervisor. Your contribution for this project is immense. Thanks you for all the hours and support in getting everything to work. I would also like to take this opportunity to thank Jairton Dupont and Victor Sans for their initial supervision in this project and for always having an open door for any research discussions.

I would also like to thank Aitor, Isabel, Israel, Andreas, Carmen, Ana and Calum, whose numerous contributions made this project viable and possible, the best postdocs one could ever have. To Rhys for the TEM images and all the help. I would like to thank the School of Chemistry, the NMRC, the CDT in sustainable chemistry, the EPSRC, Perislava Williams, Amanda Broniewski, Chris Moody and Mark Guyler.

I would like to thank all the present and past members of the Licence and JAF groups and my coworkers: Lais, Meike, Stelios, Lewis, Ben, Davi, Eimear, Maria, Marko, Carol, Ania and all the others (I am really afraid of forgetting someone!!) for their daily camaraderie and being my family away from home.

To my parents and brother, whose daily sacrifice gave me strength and inspired to continue in my path and to fight for everything I ever wanted to accomplish. And finally, to Vera, my better half, for the patience, I mean, a lot of patience to endure me. You are the family I chose.

Publications

- Valdebenito, C.; Pinto, J.; Nazarkovsky, M.; Chacón, G.; Martínez-Ferraté, O.; Wrighton-Araneda, K.; Cortés-Arriagada, D.; Camarada, M. B.; Alves Fernandes, J.; Abarca, G. (2020). Highly modulated supported triazolium-based ionic liquids: direct control of the electronic environment on Cu nanoparticles. *Nanoscale Advances,* 2(3), 1325-1332.
- Qadir, M..I.; Zanatta, M., Pinto, J., Vicente, I., Gual, A., Smith, E., Neto, B..A.D., de Souza, P..E.N., Khan, S., Dupont, J. and Alves Fernandes, J. (2020), Reverse Semi-Combustion Driven by Titanium Dioxide-Ionic Liquid Hybrid Photocatalyst. ChemSusChem. Accepted Author Manuscript. doi:10.1002/cssc.202001717

Abstract

As catalytic reactions reach nearly 40 % of the world GDP, enhancing the catalytic properties of scarce metals, generating highly active, selective and durable catalysts is critical. Bimetallic AuPd NPs present enhanced activity and selectivity in hydrogenation reactions. However, the mechanisms behind their improved catalytic properties when compare to their monometallic counterparts and the enhancement effect of Au in the alloy remains ambiguous. This thesis elucidates the synergetic effect in AuPd NPs leading to their enhanced catalytic properties towards the selective hydrogenation of CAL. The AuPd NPs were first co-deposited in IL ($[C_4C_1Im][NTf_2]$) by magnetron sputtering and their structural and electronic properties characterised. Evidence of the interaction of both metals with the disruption of the Au surface plasmon resonance in the presence of Pd (UV-vis) was observed and the absence of the Au-IL interaction with the increase of Pd content (XPS). XAS experiments confirmed the presence of a core-shell structure in the AuPd NPs with the preferential interaction of the SO_2 groups in the IL anion with the sputtered Pd atoms leading to an ordering of the NP structure during growth and nucleation. Highest conversion was obtained after 24h with $Au_{0.5}Pd_{0.5}$ (85%) in comparison to Pd_1 (36%). The effect of the both the reagents and products on the catalytic activity of the $Au_{0.5}Pd_{0.5}$ and Pd_1 catalysts was evaluated using VTNA determining a Langmuir-Hinshelwood mechanism and differences in stability of both catalysts over time. The presence of Au in the AuPd NP in IL, leads to an increase in the robustness of the catalyst, increasing the H_2 activation on the catalyst surface and decreasing the dependency on the [CAL] and [H_2].

Abbreviations and Acronyms

$[C_1C_4Im]$	1-butyl-3-methylimidazolium
$[NTf_2]^-$	bin(trifluoromethanesulfonyl)imide anion
Å	Ångström
ATR FT-IR	Attenuated total reflectance Fourier transformed infrared
AuPd	Bimetallic Gold and Palladium
CAL	Cinnamaldehyde
Cat.	Catalyst
COH	Cinnamyl alcohol
Conv.	Conversion
ESI-MS	Electron spray ionization mass spectrometry
EXAFS	Extended X-ray Absorption Fine Structure
Exp	Exponential
GC	Gas chromatography
GC-MS	Gas chromatography - mass spectrometry
GDP	Gross domestic product
HCAL	hydrocinnamaldehyde
HCOH	Hydrocinnamyl alcohol
HOMO	Highest occupied molecular orbital
ICP-OES	Inductively coupled plasma optical emission spectroscopy
ILs	Ionic liquids
LUMO	Lowest unoccupied molecular orbital
MOF	Metal organic framework
NPs	Nanoparticles

P	Pressure
PGM	Platinum-group metals
PPE	1-phenyl-1-propene
PPR	Phenyl propane
R.T.	Room temperature
Sel.	Selectivity
Subst.	Substrate
T	Temperature
t	Time
TEM	Transmission Electron Microscope
THF	Tetrahydrofuran
XANES	X-ray Absorption Near Edge Structure
XAS	X-ray Absorption Spectroscopy
XPS	X-ray Photoelectron Spectroscopy

Table of Contents

CHAPTER ONE

Introduction

1. Introduction

1.1 Catalysis

Catalysis plays an essential role in the production of the vast majority of chemicals used by modern society. In fact 80% of chemical reactions in industry are of catalytic nature, showing the importance of catalysts in manufacturing.[1, 2] A catalyst is a compound that can reduce the activation energy required for a given transformation, thus creating an alternative reaction pathway and increasing the reaction rate (Figure 1.1).[1, 3]

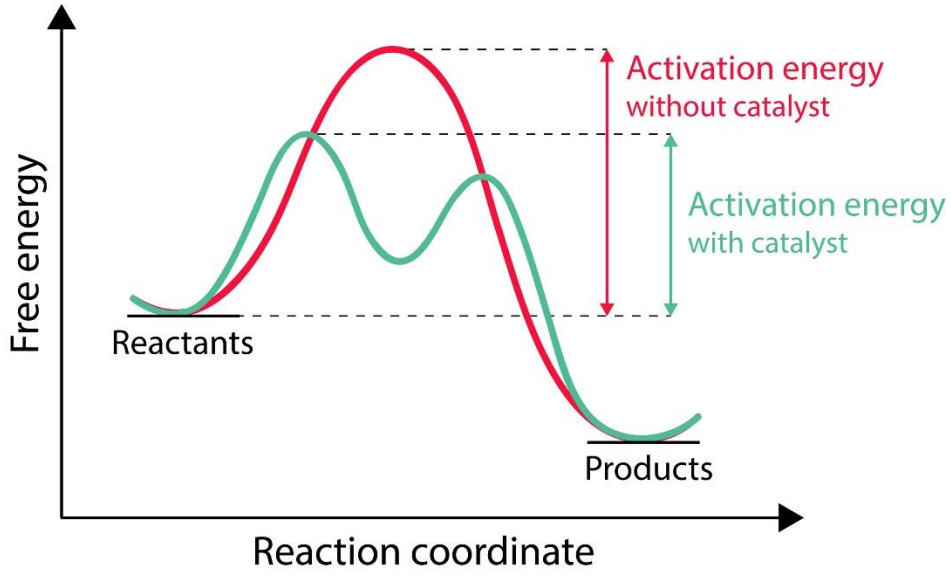

Figure 1.1 – Reaction profile with or without the presence of a catalyst.

While the catalyst contributes to the reaction, it is not consumed and can participate in many reaction cycles. Consequently, the catalyst presence is required only in "catalytic amounts" and would be sufficient catalyse large quantities of reactant molecules. [1, 2]

Catalysts can catalyse reactions due to their ability to interact between the catalyst active site and the reactants, thus creating a partial bond or shared

bond, which lowers the energy and stabilises the transition state. This allows for geometry optimisation every step along the reaction coordinate, enabling the stabilisation before the new bond is formed, and leading to a system that moves the electrons and the atoms until it finds the most stable geometry. Nonetheless, full initial dissociation of the reactant molecule is not essential for catalysis to occur. This way, the new bonds can start to form before the previous bond is broken.[1, 4] Given that both the forward and the backward reaction can be catalysed by the catalyst in the reaction media, this indicates that both reactions go through the same minimum energy pathway and have the same transition state. This way, the reduction on the activation energy of the backwards reaction and of the forwards reaction will have the same reduction and the equilibrium constant will be equal to the ratio of both forward and the backward reaction constants.[1, 4]

Given the importance of catalysts in industry processes, their utilisation must be optimised towards the highest efficiency their optimisation and improvement, such as, choice of metal used, support, phase, type of coordination, reactions conditions, among others, must always be taken into consideration and evolve, mostly when using scarce transition metals, such as, Pd, Pt, Rh, Ru, among others. The scarcity of rare transition metals is a factor that weights in considerably on the sustainability of catalytic processes. Therefore, in cases where the use of such scarce elements cannot be avoided. Therefore, increasing the usable surface area of a catalyst, enhancement of their properties using an alloy and increasing their recyclability must always be taken into consideration.[5, 6]

1.2 Homogeneous versus heterogeneous: advantages and disadvantages

Catalysis can be divided into three main categories: heterogeneous, homogeneous and biocatalysts.[4] In a heterogeneous catalysis, the catalyst is in a separate phase from the reactants. Typically, reagents are gases or liquids that are passed over a solid catalysts. As for the homogeneous catalysis, both reagents and catalyst are all in the same phase; typically in solution. Enzymes (proteins) and ribossomes are very specific catalysts with the ability to catalyse reactions inside living cells. When extracted and purified, they can catalyse reactions outside living cells (biocatalysis). Homogeneous catalysts are usually more difficult to recycle / reuse, have lower stability and are expensive. Nonetheless, they provide high activity and selectivity and have clearer mechanisms. Heterogenous catalysts are in a separate phase of the reagents and products thus have higher reuse, stability, are usually cheaper and easier to separate. However, they have lower activity and selectivity and their mechanistic understanding is poorer. Nonetheless, they are usually preferred given they increase their recoverability, which is critical for a chemical manufacturing industry process and aligns with the principles of green chemistry, such as, generating low energy routes to products.[7]

Catalysis using a heterogeneous catalyst occurs at the surface level and through three main steps: (i) the substrate or substrates must adsorb on the catalyst surface, (ii) the catalytic reaction, from substrate to intermediate (or intermediates) and product, and (iii) desorption of the final products. [1, 3, 4] In the end of the cycle, the catalyst must be in the same chemical state as before adsorption, leaving it available to assist in subsequent catalytic

transformations. During step two, as the formation of an adsorption complex between the catalyst and the reactant molecule occurs, a transient bond is formed. This alters the electron distribution of the metal catalyst, favouring the formation of new bonds with the substrate molecule. Due to close proximity, the substrate is hold by the catalyst and kept in a relative orientation that will favour the intermediate state and the breaking of existing bonds. As the reaction path progresses, the bond strengths and consequently the electron density distribution change. The catalyst local flexibility to allow localised geometry alterations, facilitated by low frequency vibrations, helps with the reaction progress. This flexibility is provided by defects on the catalyst surface, such as, kinks, edges and corners of clusters or crystals that allow energy lowering. Over the years, it became clear that the roughness of the surfaces in the catalyst's surfaces (crystal facets, and corners and edges of crystals) would deliver far improved catalytic activity in comparison to a perfect single crystal surfaces.[8]

Therefore, surface area is of utmost importance to their efficiency. Decreasing the size or amount of the catalyst used, such as, in the case of platinum-group metals (PGM) is not only beneficial from an economical point of view, but also more sustainable. By creating smaller particles with a larger fraction of their atoms on the surface, a larger fraction of the atoms present in the catalyst will be participating in a given reaction.[9, 10] Furthermore, the surface atoms on small particles possess electronic properties, which are considerably different in comparison to the atoms on the surface of larger particles and tend to be more active in catalytic reactions.[11] In addition, flexibility of clusters of atoms and nanoparticles (NPs), which possess irregular surfaces and variable

shapes, allow for continuous rearrangement in order to adapt to adsorbates often leads to much more efficient catalysts in comparison to single crystal surfaces.[8] An ideal catalyst should be able to catalyse thousands of transformations and remain unaltered. If the catalyst is altered or permanently modified during the reaction, then it cannot be termed as catalyst.[1, 2, 4]

1.3 NPs and their properties

NPs under 2 nm are typically called nanoclusters. These nanoclusters stand at the border between homogeneous and heterogeneous catalysis and have attracted great interest in recent years.

It is generally anticipated that the efficiency of a NP catalyst growths with decreasing particle size, due to the higher surface area and better utilisation of materials. Nonetheless, the decrease in size, will also lead to poor organisation and structure of clusters and nanoclusters yielding higher reactivity of the metallic atoms towards substrates.[11] Nonetheless, this dependence not always is encountered. For instance, in the case of Au/SiO_2, the size of the Au NPs over 6 nm does not affect their catalytic performance, due to the stability of Au.[12] Au NPs, require harsh conditions to be catalytic active with most catalytic activity performed by low coordination atoms present in kinks and edges of the NPs, hence discrete NPs (≤ 3 nm) are usually more active given their disorganised structures.[12-15]

As the particle size decreases, their properties and stability become greatly influenced by their environment. When they reach single atoms, their electronic structures are strongly connected to their coordination environment, being mainly dependent on solvents and ligands and their catalytic properties

are difficult to predict.[16, 17] Also, as NPs reaches 2 nm, their energy levels become continuous, mostly in the cases of metals, such as, Cu, Ag and Au, and shows their characteristic plasmonic resonance properties.[18] Thus, their optical properties will similarly be affected by the size of the particles and linked to their effect of their catalytic performance.[19] In addition, Pd, Pt and Au NPs with sizes ranging from 2-3 nm have shown optimised catalytic properties in hydrogenation reactions and selective oxidation of alcohols.[9, 10, 20, 21]

In the case of Pd based catalytic systems, wide application was found in catalysis involving hydrocarbon hydrogenation[22-25], alcohol oxidation[26-29] and C-C coupling reaction[30-32]. The established versatility of Pd can be credited to its ability to stabilise a wide range oxidations states in different types of catalysts (homogeneous / heterogenous) and using different supports (MOFs, SiO2, ionic liquids, among many others). By carefully fine-tuning of conditions and type of support, the catalyst can be tailored towards its application.[21, 33, 34] Pd-catalysts can extend from NPs to organometallic complexes, surfaces and polymetallic materials.[9, 35, 36] The extended application of Pd catalysts in hydrogenations rises from the ready absorption and activation of H_2 onto Pd surfaces. Hereby, size, electronic and atomic arrangement highly influence the adsorption strength of H_2 and other subtrates.[33, 37, 38]

Zhang *et al.* described the effect of the size Pd NPs in their activity in the oxidation of benzyl alcohol (Figure 1.2).

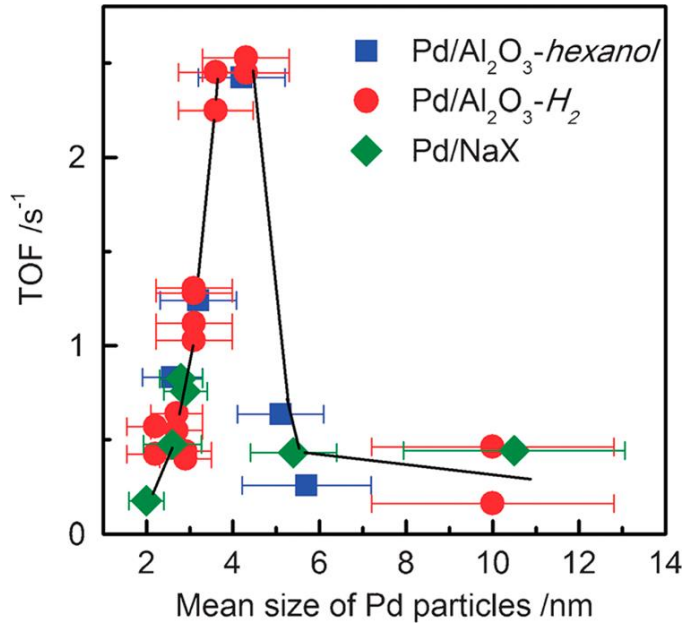

Figure 1.2- Size dependence effect of TOF on the mean size of Pd NPs for the selective oxidation of benzyl alcohol using different supports. Adapted with permission from reference 37. Copyright 2011 The Royal Society of Chemistry.

On a mechanistic point of view, the oxidation of the alcohol on the NP surface follows the expected pathways for a heterogeneous catalyst, yielding the ketone or aldehyde product by desorption from the catalyst.[39] The difference in size of the Pd NPs present a strong effect on the overall reaction rate, the adsorption of alcohol and the kinetics of the reaction. The maximum performance can be attained on Pd NPs around 4 nm yielding the peak activity for oxidation of benzyl alcohol. The size of the NPs strongly affects the adsorption strength of substrates (reactants) and products yielding a delicate balance between unreactivity and poisoning of the catalyst.

This way, it can be concluded that the number of variables that affects the catalytic behaviour of both Au and Pd catalysts is tremendous with intrinsic electronic change and adsorption strength of substrates and products changes in NPs and materials should be tested and optimised to achieve their maximum potential.

1.4 Bimetallic NPs

Bimetallic catalysts have been widely applied, due to the effects on their respective electronic properties and how they translate into their catalytic performance. Specifically, the production of AuPd alloys have been widely developed due to the enhanced catalytic properties for the production of H_2O_2 from the oxidation of H_2 by O_2 at mild temperatures[40-44] in comparison to monometallic catalysts.[45-47]

Bimetallic catalysts have also been extensively used in aerobic oxidation of primary alcohols[20] and hydrogenation reactions.[41] Nonetheless, to the current moment, investigations of these catalysts have been focused mainly in their catalytic properties with few studies on their properties and their effect on the catalytic activity.[20, 48] Understanding the alloy impact over these catalysts stability, reactional mechanisms and effects on the H_2 activation / H transfer remain unidentified.

Mostly, the catalytic properties of the alloy can be related to the d-band centre relative to the Fermi level, which represents the averaged energy of the density states in metal surfaces. The d-band centre is dependent on the overlapping of the d-orbital with adsorbates and the tensile strain to which surface atoms are subjected. Hence, the centre of the d-band can be linked to the interaction with the adsorbates, thoroughly dependent on the nature of the alloy and its core-shell structure.[20, 48-50] Furthermore, bimetallic Pd NPs, such as AuPd NPs, have found to have superior catalytic properties compared to their monometallic counterparts. The superior catalytic properties have been related to their composition and structure, producing specific electronic effects due to the synergy between both metals.[9, 33] The electronic effects rise from the

charge transfer between Au and Pd, altering the electronic structure and the width of the d-band, thus increasing catalytic activity for both Pd and Au in bimetallic composites.[51, 52] This electronic effect can also affect the catalytic activity by altering the interaction with the adsorbates, and products.[49] In hydrogenation reactions, these effects lead to differences in the strength of H binding on the AuPd bimetallic surface and consequently in increased rates of activating of H_2.[52] Furthermore, the stability of the adsorbed hybrid species H_{ads} is greatly improved on bimetallic AuPd surfaces. In combination with increased rates of H_2 activation this leads to greatly increased concentrations of H_{ads} on the bimetallic surface.[52] Indeed, both experimental and theoretical results have shown an increased activity when using AuPd NPs catalysts compared to monometallic Pd. Consequently, the careful and highly controlled design of alloy catalysts is required.[33, 53]

The enhanced control of catalytic activity and selectivity with AuPd has been exploited for a wide range reactions, including the hydrogenation of levulinic acid to gamma-valerolactone,[54] the selective hydrogenation of cinnamaldehyde (CAL)[48] and the oxidation of benzyl alcohol.[40] A fundamental example of the harmony and delicate balance required in catalysis is perfectly described by the Sabatier's principle of optimum adsorption.[55] Sabatier's principle states that if the adsorption energy of a substrate (or the heat of formation of transition metal state) is too low it will lead to low catalytic activity. Nonetheless, if the values are too high, this will lead to blockage of the surface by a product that will not desorb. This can be termed as catalyst poisoning due to the impact it has on the catalyst performance. This way, maximum activity by a catalyst is presented with intermediate heat of formation of the products.

Zhu et al., report the production of AuPd NPs in SiO_2 for the oxidation of primary alcohols and how the d-charge maximum gain, when using a composition with 33–50 at% Pd in the AuPd alloy can lead to up to 9 times improvement in the reaction rate compared to pure Pd catalysts.[20] This change on the d-orbital charge sharpens of the d-band energy and leads to an upshift in its average energy. The change in alloy content allows for different d-orbital overlap on the surface of the catalyst leading to the tuning of the d-band gain and to an evident enhancement in the adsorption strength of primary alcohols and H_2 activation observable by the kinetic gain towards the oxidation of alcohols.[20] The ability to understand the thermodynamic favourable structures of bimetallic NPs can lead to the directed design of catalysts, how the catalyst interacts with substrates and solvents.[56, 57]

In order to evaluate AuPd catalysts behave during reaction, Yang et al., studied their segregation mechanisms to assess how their surface composition changes during reaction.[58] In this report, the importance of vacancy sites on the surface and their role on the segregation of Pd and Au is discussed. These unoccupied metal atoms on the surface of the catalyst can considerably stress the distribution of subsequent atomic layers and enable atomic rearrangement between layers. The segregation of the top layers of the NPs can be controlled by the CO coverage (substrate) during reaction and is intrinsically related to NPs size and shape. The CO adsorption can rearrange the surface atoms, leading to a Pd enrichment on the surface and diffusion of Au to the inner layers.[58] As CO is adsorbed and interacts with the unoccupied atoms of the surface and neighbouring metal atoms at the second layer, stress is created which leads to significantly change the second layer atomic distribution. This

rearrangement of the top layers is due to the decrease of the thermostability of the alloy by the adsorped CO, which leads to the increase of kinetic activity. Hence, surface unoccupied metal atoms migrate into the second layer, and vice versa. This will ultimately lead to atomic exchange between the top two layers and layer by layer rearrangement.[58] Hence, alloying Au and Pd leads to the enhancement for catalytic properties of the catalyst, nonetheless, this structures are not impervious to segregation effects that can lead to the rearrangement of the atomic structure leading to the formation of a coreshell structure with an outer layer of Pd and inner layer of Au. This atomic rearrangement leads to a further increase in catalytic activity and adsoption of reactants.

1.5 Stability of NPs

In the preparation of heterogeneous catalysts, one of the most important roles is related to the stabilisation of the metal species produced, thus circumventing their sintering. The sintering of the NPs is a common phenomenon throughout their synthesis and application. This phenomena affect mostly NPs between 1 to 6 nm. Stability increases steadily up to 6 nm, over this size, the NPs become moderately stable towards sintering.[59, 60] Furthermore, the enthalpy of adsorption ($\Delta H_{ad}°$) of substrates and intermediates on single crystal oxide supported NPs greatly decreases with the size of the NPs, hence affecting the reactivity and reaction rates of the catalysts.[60]

The coarsening and general increase of size distribution of NPs can be related to two mechanisms: particle migration and coalescence (PMC) and Ostwald ripening (OR). In Ostwald ripening, small NPs or clusters are fragmented into

adatoms that can migrate and redeposit into larger structures. This phenomena is spontaneous and thermodynamically driven and it happens due different localised adatom concentrations, their free energy and to larger NPs being more energetically stable in comparison to smaller NPs or clusters.[9, 10, 61] Atoms on the surface of a NP are less stable than inner atoms, this way, the increase of the surface area and the fraction of surface atoms, leads to the decreased stability of smaller particles. PMC comprises the mobility of the NPs or clusters in a Brownian-like motion, with following coalescence leading to NP growth.[62]

The increase in the size control of the NPs and clusters and their impact on the stability was described by Wettergren *et al*., with the production of a narrow size distribution of Pt nanoclusters and subsequent comparison to a broad size distribution of Pt nanoclusters.[63] The broad distribution of Pt nanocluster evidenced significant Ostwald ripening after thermal treatment. Nonetheless, the Pt_{22} and Pt_{68} clusters presented good thermal stability after thermal treatment and little evidence of Ostwald ripening.[63] Hence, these processes are more predominant in wider distributions of NPs, leading to the reorganisation of the atoms in larger NPs, the loss of activity and surface area. This way, these processes can be supressed by the formation of nanoclusters with narrow size distributions and avoiding the presence of larger NPs that would induce the dissolution of the nanoclusters to re-deposit on the larger structures. [62, 64-67]

Also, the adsorption process during catalysis leads to orbital hybridization between the adsorbed molecule and the participating atoms on the cluster or NP. This process leads to geometric deformation, dependent on the size of the

NP or cluster. Structural changes imposed on Pt NPs by adsorbed molecules were studied by Lei *et al.*, in which they report the effect of molecules interacting with NPs of 1-3 nm.[68] The adsorption of H_2 and CO on the surface of Pt NPs with ~1 nm leads to significant Pt-Pt relaxation due to the orbital hybridization between the NP and the adsorbed molecules. As the size of the NPs increases to the range of 2−3 nm, the lattice relaxation induced by the adsorption of the reactant molecules is much smaller due to the lower fraction of poorly coordinated surface atoms on the Pt NP.[68] These dynamic structural transformations of the catalyst are also observable in other metals species, such as, Au and Cu.[69, 70] The control and understanding of these dynamic processes, can not only help controlling the size and reactivity of a catalyst, but prevent the sintering of the NPs.[71, 72]

Another consideration is that the majority of the NPs synthesis is obtained through wet chemistry, in which a soluble metallic NP precursor is used. This usually require careful control of the size and distribution of the NPs formed by the use of stabilizing agents, such as, surfactants, polymers, dendrimers and ILs.[73-76] The use of stabilizers and capping agents is the most efficient method to control the growth and nucleation of recently formed NPs. The increase of temperature and concentration of certain substrates or products can lead to their aggregation. Nonetheless, this will lead to the blockage of active sites on the surface of NPs decreasing their activity.[77, 78]

Therefore, the choice of methodology and stabilisation strategy for the production of the NPs is of great importance, with drastic effects on their activity, conversion and stability of the produced materials.

1.6 Ionic liquids on catalysis and stabilization of NPs

Nowadays, efforts are invested at academic and industrial level towards the creation of alternative solvents for greener and more sustainable processes with reduced environmental impact.[79] Some of this effort, over the last 30 years, lead to a pronounced development of ionic liquids (ILs), most due to their tunable properties where both cation and anion can be changed with an almost unlimited range of possibilities and for a wide-range of applications.[80-82] They were initially designated as the future of "green solvents" mostly due to their negligible vapour pressure and recyclability and widely tunable solvent interactions ranging from Coulombic, hydrogen bonding, dipole-dipole, electron pair donor / acceptor, van der Waals, among others.[82] Nonetheless, recent biodegradability studies[83, 84], toxicology[83, 85, 86] and life cycle analysis[87, 88] presenting their real environmental impact and energy requirements. However and despite the ILs drawbacks, systems containing ILs, due to their remarkable properties, enable the optimisation of scarce materials usage without compromising their catalytic properties and increasing their stability. For example, the stabilisation of discrete NPs with high surface area and reactivity, decreasing the usage of rare earth materials.[89-93] Furthermore, their utilisation in catalytic systems should be carefully taken into consideration, optimised and strategies that enable their recyclability developed, such as, the use of the supported ionic liquid phases (SILPs) after the optimisation of the catalytic system in pure ILs.[92, 94-100] Typically, ILs are composed by alkylated amines cations, among them, imidazolium cations, extensively applied in catalysis due to its superior performances and stability (Figure 1.3- Commonly used cations and anions in

the synthesis of ionic liquids.[106]).[101] Imidazolium containing ILs are among the most versatile to allow stabilisation of metallic NPs, owning organized structures maintained by hydrogen bonds that induce physical and structural directionality unlike most ILs charge-ordering structures. These create an extended structure of cations and anions held together by hydrogen bonding that do not compromise the catalytic activity of introduced metallic NPs.[91, 102-105]

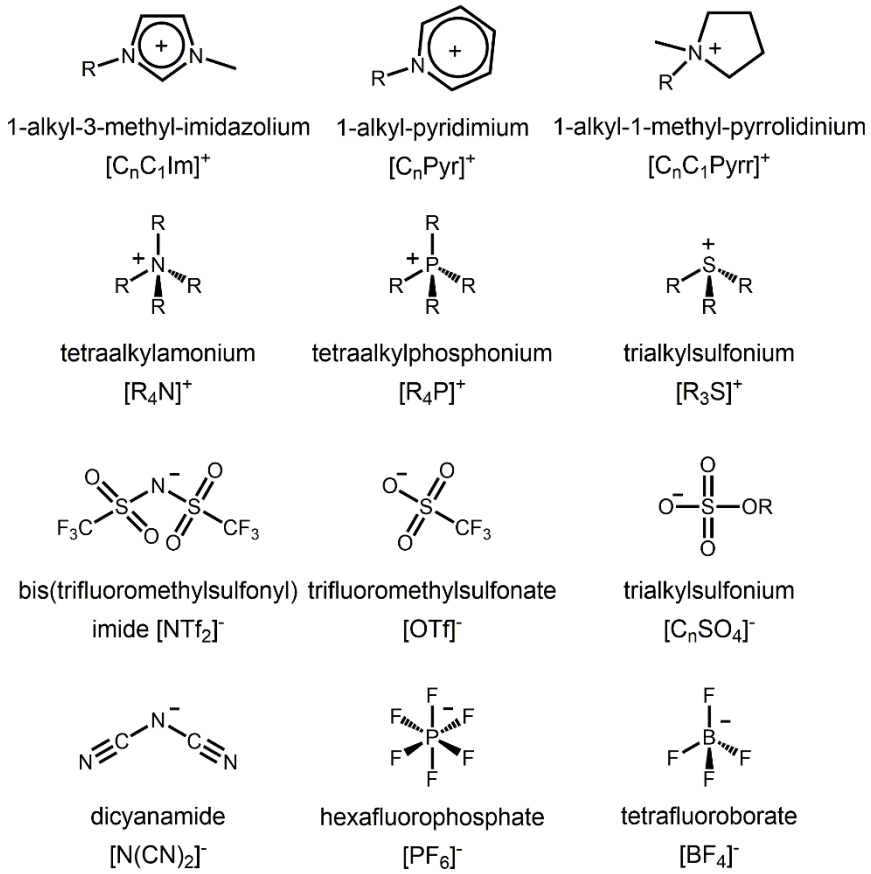

Figure 1.3- Commonly used cations and anions in the synthesis of ionic liquids.[106]

The choice of anion is also of great importance. The $[NTf_2]^-$ anion, a relatively weakly coordinating and low basicity anion is a preferred anion choice for hydrogenation reactions and stabilisation of Pd and Au catalysts by avoiding stronger interactions, charge transfer and bonding to the active sites of the

NPs.[13, 14, 107-109] The use of a highly basic anion, such as, Cl^- instead of a non-coordinating $[NTf_2]^-$ anion, would, in many cases, lead to the deactivation and loss of activity of Pd NPs in IL, presenting lower TOFs in Suzuki cross-coupling reactions.[91, 110] Therefore, use of ILs as stabilising agents and reaction media is an alternative to the stabilisation of Pd and Au catalysts. Nonetheless, the wet chemistry methodologies would require the use of capping agents and, in many cases, the use of VOCs as solvents in the synthesis of the NPs. The produced NPs would then require to be transferred into the ILs. A way to circumvent this complex methodology is through direct magnetron sputtering of NPs into ILs without the use of stabilisers.

1.7 Magnetron sputtering

Recently, magnetron sputtering has demonstrated its potential as a greener and sustainable way to produce high purity NPs.[107] In comparison with the traditional chemistry routes, it is able to deliver highly reproducible, narrow size distribution and homogenous dispersion of NPs. In addition, it is capable to produce NPs without requiring the use of capping or stabilising agents, thus being able to produce highly active catalysts.

The sputtering process consists in the bombardment of a target surface with energetic gas ions causes the physical ejection of surface atoms or clusters.[111] This physical process will be further explained in chapter 2 along with the equipment used to generate the catalysts.

The production of very uniform and small NPs (1 to 10 nm) with high purity by sputtering deposition can be directly performed into ILs.[112, 113] Their size will

be dependent upon the sputtering parameters and/or of the IL nature, mostly viscosity. [112, 113]

Several reports attempt to uncover the effect for magnetron sputtering deposition of NPs into ILs. Typically, these reports relate the experimental sputtering parameters along with the surface tension, viscosity and surface composition of the ILs present.[35, 114-117] Suggesting that nucleation and NP growth appears to occur on the IL surface, with the interaction between incoming NPs and IL surface determining the NP size and distribution.[35, 114-117] As viscosity in ILs plays an important role, the less viscous ILs, such as imidazolium containing ILs with $[NTf_2]^-$ anion, prevent the accumulation of NPs on the surface and the formation of a film on the surface of the IL.[115]

The production of alloyed NPs using magnetron sputtering was already achieved using a binary target with mixed compositions of Au/Pt in single deposition mode[118] or by co-deposition using separate targets, nonetheless, the mechanisms leading to their stabilisation and the link between the alloy properties and the benefits in catalysis remain highly debated.[119-122] Suzuki *et al.*, was able to obtain bimetallic NPs from binary targets with mixed compositions presenting similar composition to the target and alike the co-deposition using separate targets demonstrated by Deng *et al.*, both demonstrated that the stabilisation of the NPs is mostly dependent on the liquid support. PtAu bimetallic NPs deposited onto liquid PEG displayed stronger interaction of the O groups of PEG with the Pt atoms of the NPs, inducing faster stabilisation with the increase of Pt content. This lead to the stabilisation of smaller nanoclusters with the increase of Pt content. Nonetheless the

mechanisms leading to this stabilisation or the initial formation of NPs remain highly discussed.[115, 118, 119]

1.8 Hydrogenation of cinnamaldehyde

CAL can be used as a model substrate for the hydrogenation of unsaturated aldehydes, and thus developments with this model compound can be used for more complex substrates. Consequently, the ability to chemo-selectively hydrogenate to either the vinyl or carbonyl double bond is of great importance. Furthermore, one of the main products of CAL hydrogenation, hydrocinnamaldehyde (HCAL) is a crucial compound for the fragrance[123, 124], polymer[125-127] and pharma industry.[128, 129] For instance, HCAL has been used as a precursor in drug formulations, such as, for the treatment of HIV.[130]

The targeted and highly selective hydrogenation of unsaturated aldehydes (UA) to saturated aldehydes (SA) and/or to unsaturated alcohols (UOH) is an essential process for the manufacturing of fine chemicals. UOH is reasonably more difficult to obtain because the C=C hydrogenation is thermodynamically favoured over the C=O hydrogenation; consequently, research have been focusing on improving the selectivity towards UOH.[131]

In general, the hydrogenation of CAL can yield 5 products (Figure 1.4), whereby the selectivity and activity depend on the applied reaction conditions and the catalysts used for the discussed transformation. These products can be divided by the oxidation state and functionality.

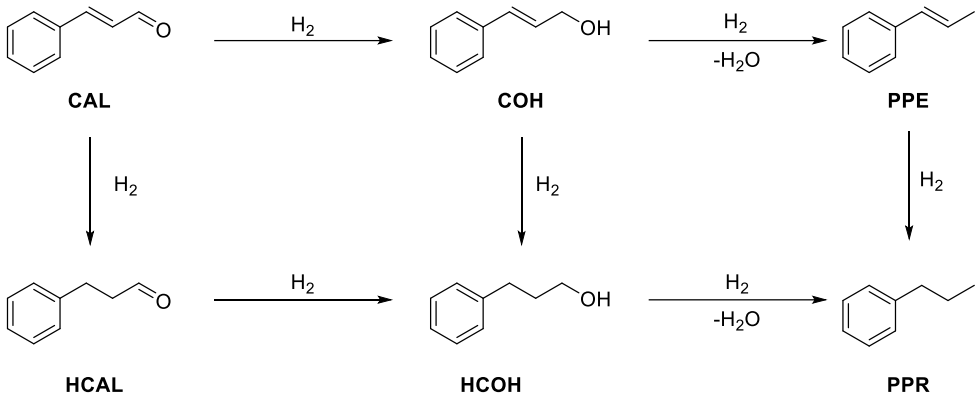

Figure 1.4 - CAL hydrogenation pathways.

For instance, the addition of 1 eq. of H_2 can lead to the formation of HCAL and cinnamyl alcohol (COH). Both, HCAL and COH can be further reduced to hydrocinnamyl alcohol (HCOH). Alternatively, COH can be dehydrated to phenyl propene (PPE) and reduced to phenyl propane (PPR). It is important to note that HCOH can also be dehydrated to PPR, representing an alternate route to PPR. The obtained intermediates, HCAL and COH, are valuable substrates for industry and their purity is highly desired.[21] Hereby further hydrogenation / hydrogenolysis to products such as HCOH and PPR, respectively and other undesired side products should be avoided. Hence, a catalyst with high specificity towards HCAL and COH is regarded as highly desirable.

There are a vast amount of examples to direct the selectivity of hydrogenations with different functional group, nonetheless, they can be summarised into three major strategies: designing electrophilic sites in catalysts, confinement/steric effect or by modifying electronic properties of the catalysts produced, such as in the case presented in this thesis with the use of ILs.[21] Another pathway for increasing selectivity in the hydrogenation of CAL is regarding the activation of hydrogen, as presented bellow.[132-137]

1.9 Hydrogen activation pathways and strategies

A crucial aspect in the selective hydrogenation of a compound is the adsorption and activation of H_2. The manner of activation and the species produced (i.e., $H^{\cdot}$, $H^{\cdot}$, H^-, H^+) profoundly impacts the selectivity of the catalyst. The cleavage of H_2 can produce H^+ /H^- (heterolytic) or $H^{\cdot}$ / $H^{\cdot}$ (homolytic), which can alter the preferential side of reduction.[138-140] In this way, a heterolytic activation of the H_2, would lead, in the case of the selective hydrogenation of CAL, to the reduction of the C=O bond, whereas a homolytic activation would reduce the C=C bond leading to HCAL (Figure 1.5). Hence, the type of H_2 activation will affect the selectivity and the products obtained.

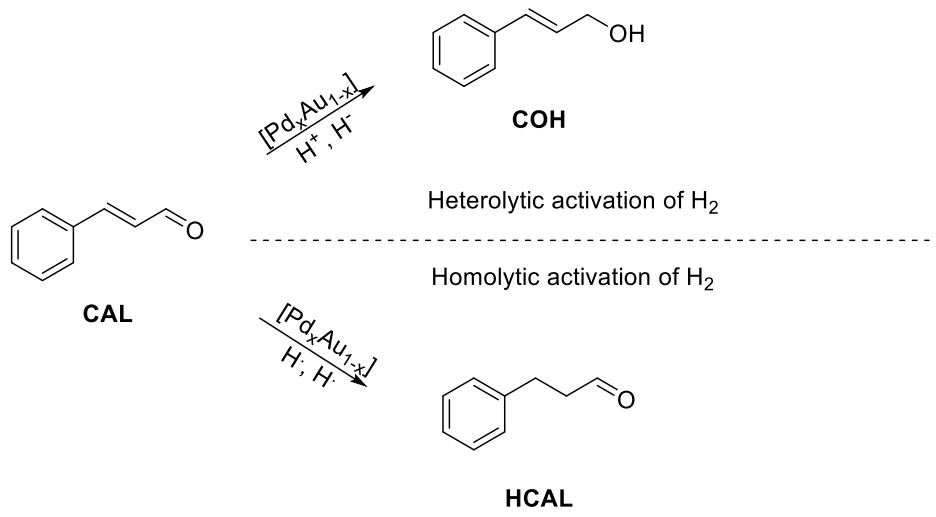

Figure 1.5 - CAL hydrogenation pathways accordingly to different H_2 activation mechanisms.

Numerous examples of both types of activations have been reports over the years using both homogeneous and heterogeneous catalysts. Given the importance of both types of catalysts and the remarkable approaches used to obtain the different mechanisms of activation, selected examples of each with be provided subsequently. A relevant example of heterolytic activation by homogeneous catalysts in the selective hydrogenation of CAL is presented in

the form of air-stable AuNPs employing tert-butyl(naphthalen-1-yl)phosphine oxide as supporting ligand. In this mechanism, the activation of H_2 is different, producing charged species (i.e., H^-, H^+). These will target the selective reduction of the polar bond, C=O on the CAL molecule. Secondary Phosphine Oxides (SPO) in these catalysts play a crucial role in giving the highest activity (>99% conversion) and selectivity (>99% COH) in the catalytic hydrogenation of α,β-unsaturated aldehydes to date by NPs.[139, 140] In a similar way, Triphos ruthenium Catalysts are able to selectively hydrogenate CAL to COH with over 99% conversion and selectivity up to >99% with a TON as high as 100000. Nonetheless, Ru-triphos represents a homogenous catalyst which present reusability and economical challenges despite their great activity in comparison to Pd and Au in NPs form. [34, 141, 142,143] These catalysts explore the electronic properties of the metal sites, hence the adsorption affinities towards C=C and C=O bonds change and due to the unique way that the C=C and C=O bonds interact and adsorb into metal sites. This is one of the main strategies towards chemo-selectivity.

In contrast to the previously discussed, heterogeneous catalysts in the form of Pt NP capped with secondary phosphine oxides can be used to achieve C=O hydrogenation.

The use of Pt NPs is when immobilized in non-porous Al_2O_3 with aspartic acid exhibiting superior performance than mesoporous Al_2O_3. The presence of aspartic acid molecules resulted in enrichment of electrons on the metal surfaces, which is favourable for the activation of the electrophilic C=O group, enhancing its adsorption and leading to a higher activity and selectivity to the

unsaturated alcohols.[144] This example presents a model of how designing electrophilic sites can modify the selectivity of a catalyst.

This strategy is also used in metal–organic frameworks (MOFs) by using electrophilic sites with lone electron pairs, such as O near the active sites to allow the preferential activation of the C=O bond. The activated C=O can then be hydrogenated by H adsorbed on a nearby active site.[145] This strategy to exploit synergetic effect between active sites and electrophilic sites leads to an improved hydrogenation activity of the C=O bond. Another approach to enhance the selectivity towards a desired product is to design catalysts that exploit confinement/steric effect, hence preventing the C=O or the C=C bond from interacting with the catalyst active centres.[21]

Dissimilarity to heterolytic activation, homolytic activation, presented in this thesis, is widely demonstrated with metallic NPs.[9, 21, 33, 34] In this mechanism, two identical H· are produced which are then stabilized on the surface of the catalyst or incorporated into the catalyst struture.[52, 146] In general, these will target the selective reduction of the non-polar bond, C=C on the CAL molecule yielding HCAL. Pt NPs stabilized in MIL-101 produced a conversion of 100% with over >99.9% selectivity to HCAL due to the synergetic effect between highly dispersed Pt NPs and Lewis acid sites of the MOF. Hereby the Lewis acidic sites inhibited the hydrogenation of C=O sites due to their strong interaction with the C=O bond.[147] As addresses previously, Pd NPs are among the most active and selective catalysts for the partial hydrogenation of CAL.[9, 21] For instance Pd-NP sputtered into IL hybrid organosilica achieve high activity and selectivity towards HCAL in the hydrogenation of CAL.[109]

In a similar process, the stabilisation of Au NPs presents the expected low coordination number of the surface sites able to chemisorb/activate simple molecules and H_2.[14] Nonetheless, given the Au lower reactivity, the activation of H_2 is performed only on these lower coordination sites, such as, edges and vertices of the NP.[13, 14]

Nonetheless, the presence of a support, such as, TiO_2, Al_2O_3 and CeO_2, the support presents a synergetic affect by bridging with the low-coordinated Au atoms and leading to the dissociative chemisorption of H_2 through heterolytic activation. This effect was tested by the presence of IL. The presence of IL would impede the activation of H_2 on bridging sites between the Au NP (metal atoms in close proximity with the support) and the support, thus preventing this mechanism and leading to the homolytic activation of H_2.[14] Similar systems are also reported by Mitsudome *et al*., the coverage of Ag NPs with basic material (AgNPs-BM), minimized the interface area of the AgNPs–BM and enabling the heterolytic activation of H_2 due to the combined effect between Ag NPs and basic sites, suppressing the formation of homolytically activated H_2 species.[138] The high influence of supports on the selectivity of the catalyst is further exemplified by Shi *et al.* reporting that Au NPs stabilized by PVA and impregnated on SiO_2, produced over 94% selectivity towards HCAL, nonetheless, when supported in ZrO_2, it presented low selectivity towards HCAL.[148] hence, the selectivity of the metallic NPs can be changed and adapted towards the desired process.

The catalytic performance of bimetallic AuPd NPs on ILs ($C_1C_4Im][PF_6$] is presented by Dash *et al.*. Bimetallic AuPd NPs were first stabilized using PVC followed by their transfer into the IL while suspended on volatile solvent. The

ratio of 1:3 Au:Pd had the highest catalytic activity and selectivity for all the tested substrates and in the case of the hydrogenation of CAL, the main product observed was HCAL with further hydrogenation occurring to HCOH. The COH product was not observed.[149] More recently, Cattaneo *et al.,* reported the fabrication of AuPd NPs using wet chemistry and their stabilization on TiO_2.[48] The optimum catalytic activity for the hydrogenation of CAL was observed for $Au_{0.50}Pd_{0.50}/TiO_2$, while the monometallic Pd/TiO_2 as the most selective towards HCAL. Nonetheless, further hydrogenation to HCOH was also present.

Most interestingly, in most cases, the enhancement of selectivity comes with detrimental cost to the catalytic activity. Consequently, there are still considerable challenges in the development of catalysts that combine highly selectivity and with a high activity. Also, catalyst design by tuning the electronic properties of the active site and achieve effective electron transfer using an electro-positive promoter is of utmost importance. Overall, from the later examples, the understanding of bimetallic catalysts, their mechanisms and properties is of utmost importance in order to produce more sustainable and targeted catalysts combining high selectivity, activity and stability.

1.10 Mechanistic studies of the hydrogenation of CAL

1.10.1 Kinetic investigations methodology

Most kinetic investigations contain complex reaction pathways with multistep reactions and several products. These tend to be extremely difficult to investigate hindering the understanding of most complex reactions and eluding the mechanisms and reaction pathways underlying their behaviour.

The nature of a reaction and its kinetics can be explained by following the initial rate (r_0) of a given reaction and changing the concentration of compound [A]. If the initial rate of the reaction is proportional to the change in concentration of $[A]_i$, then it can be can assumed that compound A is involved in the rate determining step (RDS). However, if the r_0 is not altered by the $[A]_i$, then the reaction is no affected by the [A], hence the reaction is independent of the [A]. Nevertheless, the reaction mechanism is considerably more challenging to demonstrate since concentrations have a different effect and adsorption, desorption and transport limitations of compounds should be taken into consideration. Hence, the analysis of experimental data is usually complex. This way, simplified methods of representing experimental data (kinetic data) are often sought after and indispensable. A remarkable example of such importance is presented by the double-reciprocal plot established by the double linearization from Lineweaver and Burk.[150, 151] This methodology quickly became an important graphical tool to make sense of kinetic parameters in both enzymatic and nonenzymatic catalytic systems and the original report become the most-cited paper in the Journal of the American Chemical Society (JACS) due to its unprecedented value. Therefore, a readily available and easy to use methodology to assess impenetrable experimental kinetic profiles through a graphical approach, would allow to evaluate the effect of small changes in reaction conditions in the kinetic traces obtained and the dependencies of the reactants. Such tools usually require fewer experiments and can provide greater mechanistic insight in a comparative approach. Aligned with *in situ* reaction progress methodologies coupled these simple data manipulations can help to unveil aspects of catalytic performance.

In order to evaluate the effects of the different reagents into the reaction kinetic traces, variable time normalized analyses (VTNA) can be applied according to methods proposed by Bures and co-workers, allowing for a comparative quantification of rate orders for reagents, products and the order of catalyst.[152, 153] Using this methodology, the normalisation of the time component towards the investigated component allows for a visual overlay of the kinetic traces, evaluating the use of different concentrations and their effect on the kinetic traces. When the substrate being studied is raised to the correct order, thus removing the investigated reagent from the kinetic trace, an overlay of the kinetic traces normalised is obtained. This will produce an overlay of the kinetic traces normalised if the substrate is raised to the correct order, and if no substantial degradation of the given catalyst is present.[152-154] It will also allow the study of the reaction dependencies on the given substrate concentration and evaluate their importance and dependency on the RDS of the reaction. Therefore, allowing the evaluation of the mechanism behind the hydrogenation of CAL.

1.10.2 Kinetic investigations mechanisms

Evaluating the interaction of the different substrates with the catalyst is of utmost importance for kinetic studies. The adsorption of a specific substrate into the surface of the catalyst might determine their participation on the rate determining step for the given reaction and their mechanism by which the catalytic reaction occurs.[155, 156]

In heterogeneous bimolecular reactions, the two most commonly accepted mechanisms are: the Eley–Rideal and the Langmuir–Hinshelwood mechanisms.[157] These will be further explained in chapter 5. In the case of the

Eley–Rideal, one of the reactants is required to be chemisorbed on the surface of the catalyst, whist the other reacts from the gas phase *via* collision with the chemisorbed reactant. In the Langmuir–Hinshelwood mechanism however, both reacting species are required to be chemisorbed on the catalyst surface for the reaction to take place.[157]

In Figure 1.6, both mechanisms are exemplified using the selective hydrogenation of CAL as an example.

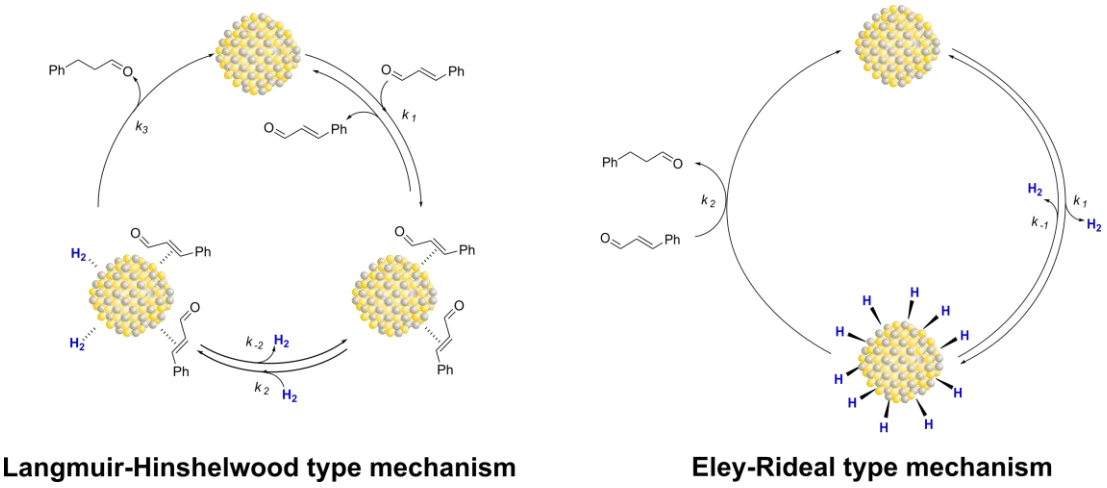

Figure 1.6 – Langmuir-Hinshelwood (left) and Eley-Rideal (right) mechanisms adapted for the selective hydrogenation of CAL.

Using VTNA, the dependencies of both H_2 and CAL, the initial absorption and activation of H_2 can be evaluated.[33, 34] The presence of catalyst poisoning can also drastically modify the surface or block the access to catalytic active sites by the reactants. By adding increasing amounts of HCAL, the effects of a possible product poisoning can be investigated by the kinetic traces obtained. The presence of a possible catalyst deactivation can be observed, if no poisoning is observed and if the catalyst presents decreased activity. These dependencies will be further explored towards the final chapter of this thesis.

1.11 Aims and objectives

The aims and objectives of this thesis are based in the investigation of the synergic effect obtained in bimetallic AuPd NPs sputtered into ILs and the enhancement of their catalytic properties. The set objectives for this thesis are:

- Production of AuPd NPs by MS deposition in IL
- Characterisation of the AuPd NPs in IL by TEM, UV-vis, XPS and XAS
- Develop a model for the AuPd NPs in IL structure and stabilisation in IL
- Optimisation of reaction conditions evaluating the dependency of temperature, pressure, solvent and metal ratio on the conversion, activity and selectivity of the catalysts.
- Understanding the reaction mechanistics through kinetic measurements

Usually, in literature, the mechanism leading to the stabilisation of co-deposited bimetallic NPs obtained by magnetron sputtering is not quite well understood. In addition, the catalytic properties of AuPd catalysts are only reported to be superior to their Pd counterparts, nonetheless, with reduced knowledge of their stability, stabilisation and effect of the alloyed metals in their catalytic properties. Hence, the work presented in this thesis addresses the gap of knowledge in the mechanisms leading to the formation of the bimetallic NPs by magnetron sputtering from the atomic ejection to their stabilisation in the IL. Furthermore, the effects of the addition of Au to the already active Pd catalysts in terms of performance enhancement / stability of the catalyst are investigated and the mechanisms for the selective hydrogenation of CAL evaluated. The unique system used for the production of the AuPd NPs is

described in chapter 2 along with the techniques used. The main objectives were divided into chapters, as presented:

Chapter 3 proposes the calibration of the equipment for both the deposition of Pd and Au into IL, in single deposition and co-deposition mode and evaluate the bimetallic materials obtained. The characterisation is obtained by TEM, UV-Vis, XPS, and XAS. This would enable to understand the mechanisms leading to the formation and stabilisation of AuPd NPs in IL.

Chapter 4 aims at evaluating the catalytic performance of the obtained AuPd NPs. The effects of reactional parameters, such as, temperature, solvent and pressure in the catalytic activity will be evaluated comparing the materials produced with similar materials described in the literature. The influence of the Au/Pd ratio in their catalytic properties is evaluated.

Chapter 5 aims at further elucidate the apparent rate orders, poisoning effect of both substrate / product and deactivation patterns in order to capture the mechanistic aspects of both catalysts and determine the effect of the addition of Au.

CHAPTER TWO

Experimental and methodology

2. Experimental and methodology

In this chapter, the experimental procedures are presented, firstly detailing the magnetron sputtering deposition equipment and the main characterisation techniques used. Secondly, the synthesis of the ILs and the deposition of AuPd NPs are detailed. Finally, the catalytic experimental set up is described within this chapter.

2.1 Magnetron sputtering

Conventionally, magnetron sputtering process is used for coating solid substrates in order to modify their surface properties. Recently, it has been shown that sputtering deposition can also be performed in liquid substrates with lower pressure vapour.[117] For instance, several groups have shown the production of very uniform metal clusters/NPs (1 to 10 nm, depending on the sputtering parameters and/or of the IL) by magnetron sputtering deposition in ILs.[112, 158, 159] This approach overcomes all the concerns of the chemical synthesis of NPs enabling to synthesize NPs in a more environmentally friendly way. The magnetron sputtering process consists in the bombardment of a pure metal target surface with energetic gas ions causing the physical ejection of surface atoms or clusters from the target into a substrate as presented in Figure 2.1 - Schematic description of the sputtering process.[160-162]

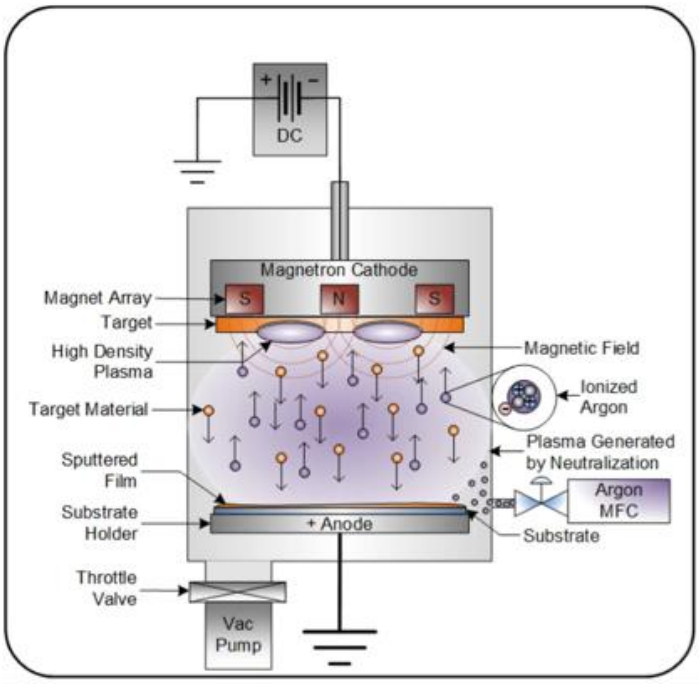

Figure 2.1 - Schematic description of the sputtering process.

In the magnetron sputtering process, the background pressure and the purity of the target are essential parameters to assure the purity of the deposited material.[107, 163] The background pressure in the sputtering chamber it is the lowest value possible (in our system: 10^{-9} torr) in order to remove all possible contaminants, that can react with the target and sputtered metal atoms, thus contaminating the obtained materials. After this, an inert gas (*i.e.* argon) is introduced in the chamber in a controlled flux and pressure (*i.e.* 10^{-2} to 10^{-3} mbar - work pressure). A voltage is applied between the cathode (target) and anode (substrate) in order to ionise the gas. The magnetrons coupled to the target have a function to confine the plasma near to the target increasing the sputtering yield, which represents the number of target atoms eject per argon ion striking under specific condition of deposition. This parameter is unique to the surface binding energy of the target material, on the power applied, angle of the incident ion, atomic mass of the ion, target and work pressure. It is

important to mention that the thickness and amount of the material deposited on the substrate will depends on a multitude of factors, such as power, target material, duration of deposition among others.[112, 159, 163]

In this work, the production of AuPd NPs in IL was carried out using a bespoke magnetron sputtering system. As this approach is a non-conventional way to produce metal catalysts, the system in UoN was specifically designed for production of metal NPs in a vast array of supports (substrates) and therefore it is described.

2.1.1 Magnetron sputtering specifications

The materials studied in this thesis were produced using an AJA magnetron sputtering chamber coupled to a glove box (MBRAUN UNIlab eco, see Figure 2). The main chamber (a) where the catalysts deposition takes place is fitted with 3 targets, substrate holder able to spin up to 100 RPM, whose distance to the targets is adjustable and able to heat up to 800 °C. To avoid breaking the high vacuum inside the main chamber, the samples can be inserted via a load lock mechanism using a transfer arm (b). The transfer occurs through a gate valve controlled to transfer the sample holder from either the load lock (b) or the glove-box into the main chamber and vice versa. In this work, the IL was introduced into the main chamber from the glove-box. The system's main chamber, which can hold up to 5 different targets (Figure 2.2), can be used for: *i* - individually for simple depositions; *ii* - sequential deposition mode where different material is deposited on a substrate each time, *iii* - co-deposition mode, in which two or more targets are used at the same time. This system is currently equipped with three power supplies connected to 3 individual targets that allow for their co-deposition with independent control of the parameters.

The deposition parameters and valves are controlled by a “LabVIEW” based software “Apex”.

Figure 2.2 - AJA magnetron sputtering system composed of the main chamber (a) with inset presenting the 3 target currently fitted into the system, load lock mechanism for transferring the samples (b) and a glove-box for storage and handling of air sensitive samples (c).

Each target possesses a shutter mechanism (Figure 2.2, right inset) capable of physically interrupt the path between the sputtered metal atoms and the substrate during deposition. This can be used during initial stabilisation of the plasma, and decrease of power during the final stages and therefore providing an accurately control of the deposition time. Also, each target possesses an arm mechanism capable adjusting its position and changing the angle of deposition. This tilting mechanism allows directionally into the flow of metal atoms and clusters being ejected from the target, which is crucial for multi-metallic NPs production, by setting the sputtered atoms path to intercept from

before reaching the IL. This system can use adaptable sample holders, as presented in Figure 2.3.

Figure 2.3 - Main chamber view while transferring a sample holder from the load lock into the main chamber (left) and liquid sample holder (right).

The liquid sample holder used in this work is presented in Figure 2.3 (right), which can be inserted via load lock or through the glove box. It holds a central position for the placement of a petri dish (⌀ =4 cm) containing a liquid substrate. The substrate holder distance (Figure 2.4) relative to the target can also be adapted controlling the height of the substrate holder mechanically and the rotation speed.

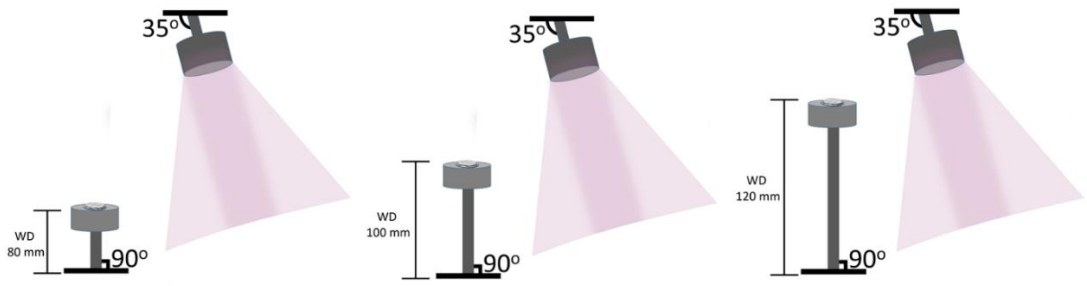

Figure 2.4 - Substrate holder distance towards the targets.

2.1.2 Introducing sample in the main chamber:

The magnetron sputtering system (Figure 2.5) is fitted with a load lock pre-chamber (a) with independent pressure transducer (b) and height adjustment for sample holder transfer (c) thus preventing the need of bringing the main chamber to atmospheric pressure to insert a sample.

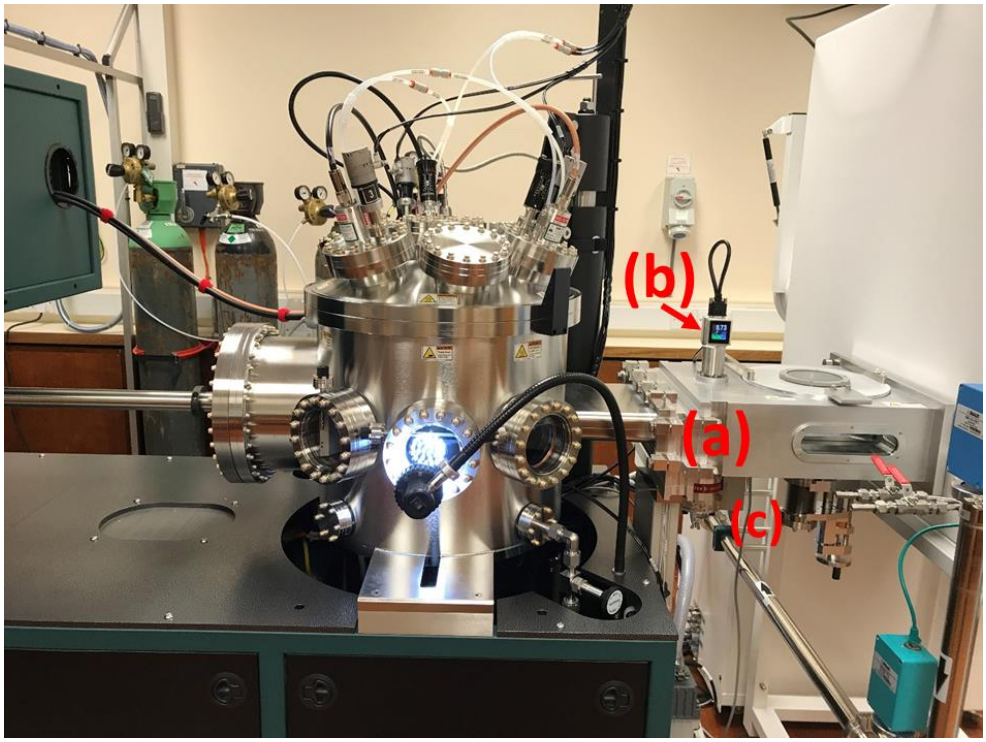

Figure 2.5 - Main chamber and load lock mechanism (a) with pressure transducer (b) and height control (c).

The load lock can be accessed via a lid on top to load air stable samples (Figure 2.5) or through the opening to the glove box, which is a special feature of this designed equipment. This way, air sensitive or hygroscopic samples can be prepared and inserted into the load lock via glove box without being exposed to air. During this work, all samples were introduced via glove box due to the nature of the IL used and to avoid the presence of moisture in the sample. The IL then, is transferred to the load lock and after ca. 2 hours

reaches the background pressure of 10^{-7} torr. With the gate valve between the main chamber and the load lock opened, a transferring arm can take the sample from the load-lock into the main chamber. All samples, after deposition, were maintained inside the glove box, with only the necessary quantities being weight into a vial and taken out for characterisation or catalysis.

A portion of the parameters, such as the tilt of the targets, the substrate holder distance towards the targets and the rotation speed, are manually fixed. Nonetheless, the majority of the deposition process parameters are controlled by the software “APEX” (Figure 2.6). This software can control the rotation of the sample holder – ON/OFF (a), the flow of the sputtering gas (b), the work pressure inside the chamber (c) and the power output of the sources (d). Direct current and pulsed direct current are available for conductive target materials and a RF source for insulating target materials. All these parameters and the length of the depositions are programmed, increasing the reproducibility of the system.

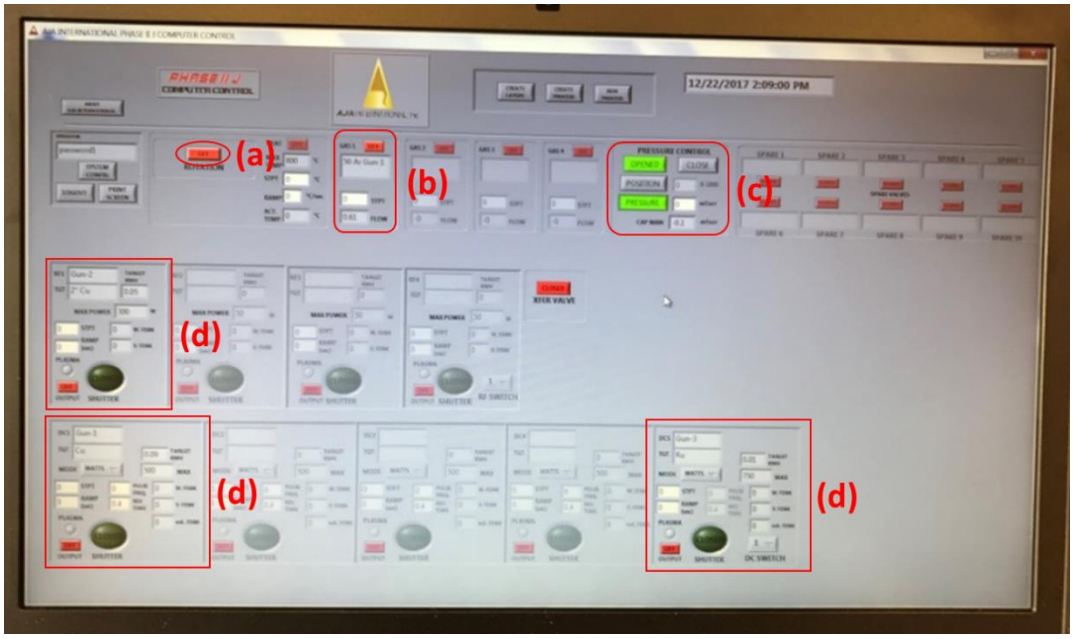

Figure 2.6 - LabVIEW based "Apex" software.

2.2 TEM principles

TEM is one of the most powerful techniques in nanotechnology and material science, granting the ability to characterise materials with a high spatial resolution of 0.05 nm.[164] TEM provides information of NPs size distribution, chemical composition and crystalline structure. TEM techniques can be divided in three main categories: scanning transmission electron microscopy (STEM); high resolution TEM; and 3D electron tomography technique. [165, 166]

In a TEM microscope, an electron emission source produces a beam of electrons which are focused and accelerated by series of electromagnetic lens before and after passing through the specimen. The electrons that can permeate and be transmitted through the specimen will reach the electron detector and magnified. The received image can be transformed into a 2D

electron density contrast map image using the Fourier transform.[164] As the electron penetrate the sample, they can be scattered (elastically or inelastically) and the detector form an image with the transmitted or scattered electrons. These are termed dark field imaging and bright field imaging, respectively. Although atomic resolution is theoretically possible, it is difficult to achieve due to defects in the lenses on HRTEM or probe size in STEM.[167-171] These can be overcome by an aberration corrector probe that corrects the spherical and chromatic aberration.[172] Nonetheless, in this specific case, the nature of the sample, with the presence of IL in the TEM grid, reduces the resolution of the imaging due to the loss of contrast between the NPs and the several layers of IL present.

2.3 XPS principles

XPS is considered one of the most invaluable and powerful techniques towards analysis of near-surface chemical composition and chemical environments of materials. Given the ILs low vapour pressure, UHV-based investigations in AuPd@IL samples can be carried out without experimental set-up modifications and avoiding the risk of significant samples loss and chamber contamination.[36, 173-175] XPS can be used to detect impurities in the order of 0.1% atomic, evaluate the surface composition of an IL/NPs and understand the IL interactions with metallic NPs.[176]

As for the technique, XPS is based on the photoelectric effect occurring when high energy photons (hv = 1486.6 eV for Al K_α) hit a compound producing an emission of photoelectrons. This photoelectron kinetic energy can be calculated by Equation 1:

$$KE = hv - BE - \phi s \qquad \text{Equation 1}$$

Where KE is the kinetic energy of an emitted photoelectron (not impacted by energy loss due to inelastic collision), *hv* is the energy of the incident X-ray photon, BE is the binding energy and ϕ_S is the work function of the spectrometer.

When an incident photon is sufficiently energetic, it is able to ionise different levels of the sample's core electrons and produces a spectrum displaying the accessible energy levels and a distribution of photoelectrons with kinetic energies measure relative to the Fermi level (highest occupied quantum level) and is both element and orbital specific.[177] The energy required to remove an electron form the Fermi level to the vacuum level in a spectrometer is described as the work function (ϕ_S).[177]

2.3.1 X-ray photoemission spectra

The XPS analysis provides semi-quantitative analysis of each element at a minimum of one core level line per element (excluding hydrogen and helium) from these photoemission lines and peak position can be obtained as binding energy. This allows for element analysis detecting elements at atomic percentages of 0.1%. This value is referenced to elements with low photoelectron cross-section of the core levels, other elements can be detected at lower atomic percentages.[178]

Data provided by XPS analysis can be obtained in the form of survey scans (or wide scans) or in the form of high resolution scans. Survey scans, as presented in Figure 2.7, displays the photoemission emitted from the entire energy range covering 0 – 1400 eV. These are often recorded with a pass

energy of 80 eV and a step size of 0.5 eV. These conditions allow for high signal intensity, nonetheless, decrease the resolution spectra obtained. This scan is particularly important in determining the qualitative elemental composition of the sample and the presence of impurities.

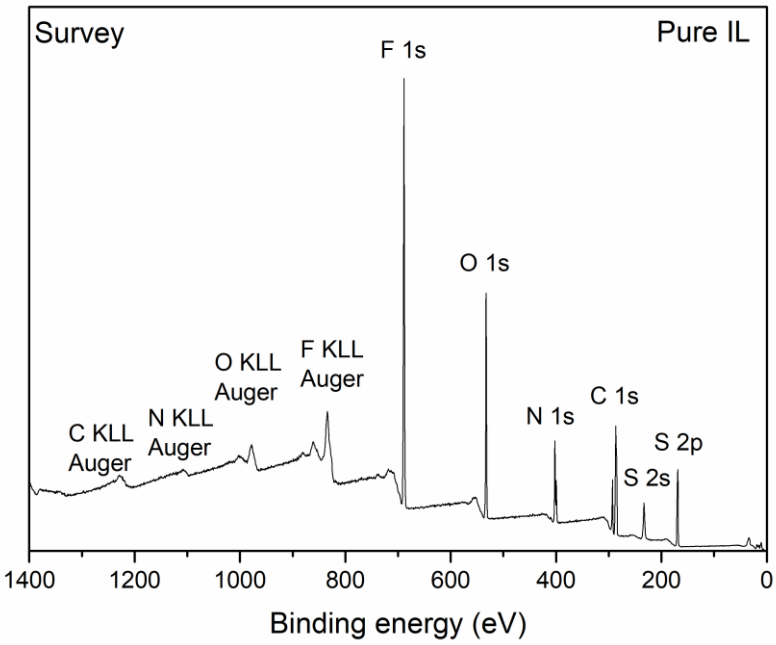

Figure 2.7 - Survey scan from the [C_4C_1Im][NTf_2] IL substrate acquired with Al Kα X-rays. Sample was charge corrected to the F 1s photoemission peak to 688.9 eV.

The wide scan can be divided into the main photoelectron lines, between 35 – 800 eV with well-defined and sharp peaks in which each elements present a distinctive set of spectral lines (element and orbital specific).[179] Valence band peaks appear between 0 – 35 eV and provides insight on the electronic density of electronic states in the valence band of the elements present on the sample. Over 800 eV and to 1440 eV are present in the Auger peaks. These occur due to the de-excitation of electrons from a higher level to a recently vacant level produces sufficient energy to eject a lower energetic electron.[179]

After the determination of the elements present, high-resolution scans (Figure 2.8) can be used to focus in a specific region of the spectra obtaining spectra with higher resolution. These scans have high counts and are typically longer, with lower pass energy (20 eV) and smaller energy steps (0.1 eV). High-resolution spectra are focused in a defined binding energies range with high precision to obtain high quality data (counts) on the element electronic environment and chemical state.

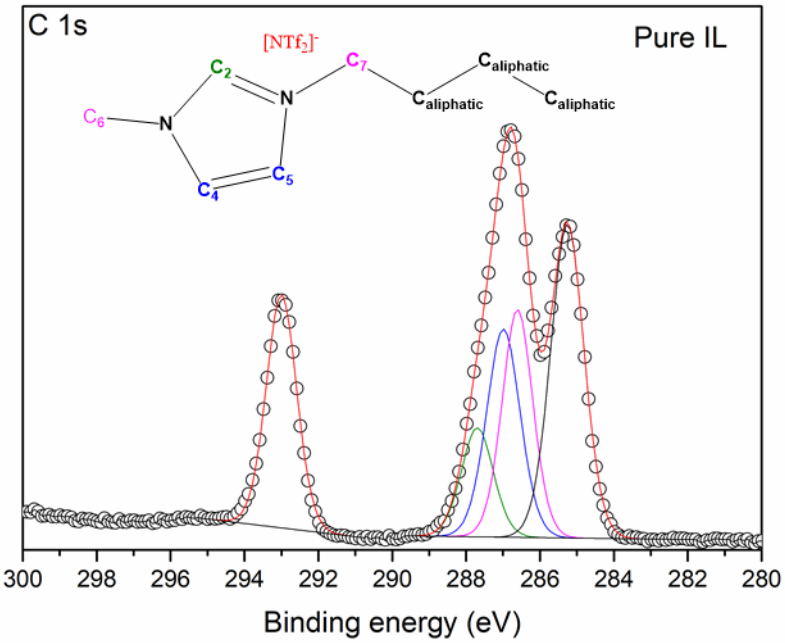

Figure 2.8 - High-resolution of the C 1s region from the [C_4C_1Im][NTf_2] IL substrate with the "balls" (○) representing data points acquired with Al Kα X-rays and the red line the sum of all mathematical fittings. Individual lines were fitted for the different C 1s components of the IL with the C_2 (green), C_4 and C_5 (blue), C_6 and C_7 (pink) and $C_{aliphatic}$ (black). Sample was charge corrected to the F 1s photoemission peak to 688.9 eV.

In Figure 2.8, the C 1s region from the [C_4C_1Im][NTf_2] IL is presented. In most ILs, the C 1s region presents a photoemission spectra with different chemical environments that are particularly close and difficult to differentiate. In these cases, fitting models needed are available and established, to describe the

different chemical environments present.[180] In all the spectra presented in this thesis, the “balls” (○) will represent data points, the red line the envelope which is the sum of all the mathematical fittings presented in diverse colours with the baseline in black.

2.4 XAS principles

XAS is a powerful technique, allowing to probe the local structure in chemically disordered matter and obtain information about the electronic structure, oxidation state and coordination environment of the alloys/NPs, being able to characterize both bulk, to nanoscale materials and even a single atom dispersions.[181, 182] Hence, providing information on the stabilisation of metal atoms in their support material. A high powerful source of x-rays (synchrotron) produces photons that interact with deep-core electrons. These deep-core electrons can be promoted to an unoccupied state above the Fermi level when the incident energy is higher than their binding energy. This excitation leaves a core-hole or vacancy that requires filling by a higher-lying electron. As this electron decays to fill the vacant core-hole, a photon is emitted. Due to the high flux of photons, XAS is able to analyse very dilute samples using a localised beam (spot size ≈ 50mn) and with fast acquisition times. This way, XAS is able to analyse the absorption coefficient (μ) as a function of photon energy. As described by equation 2. This absorption coefficient is a decreasing function with the exception of localised jumps (absorption edges), when the incident energy is higher than their binding energy of a core electron.

$$I = I_0 \exp\left[-\mu t\right] \qquad \text{Equation 2}$$

This phenomena is termed the X-ray absorption near edge structure (XANES) and provides information of the valence electrons, speciation and local geometry of the metal present (Figure 2.9).[183]

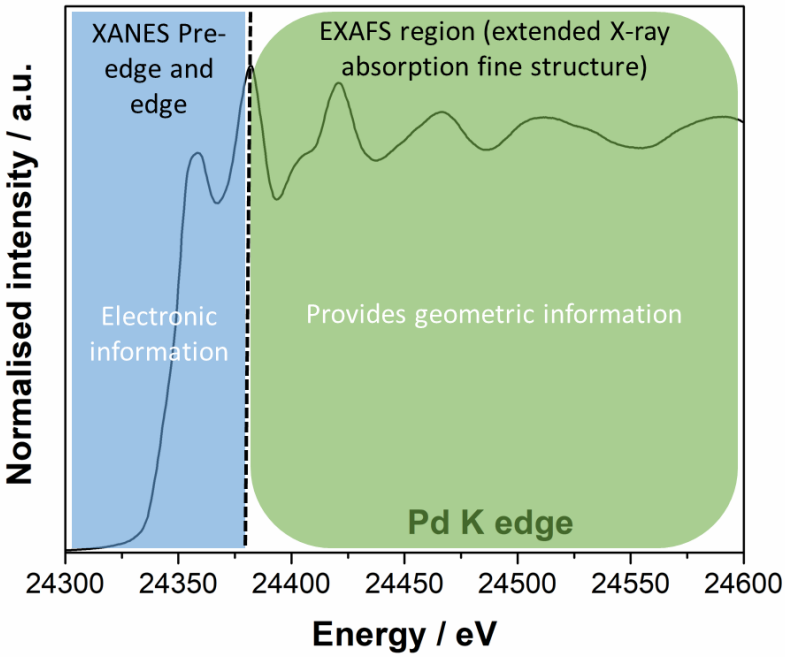

Figure 2.9 - X-ray absorption spectroscopy presenting the regions observed and the information obtained.

As the energy increases, the core electrons are excited into a continuum state, due to the constructive or deconstructive interference of the scattering wave with neighbouring atoms in the photoelectron phenomena. As the photoelectron, behaving as a wave, interacts with the electronic potential of the neighbouring atoms, it creates the oscillatory behaviour of the outgoing photoelectron and the backscattered wave (Figure 2.10).

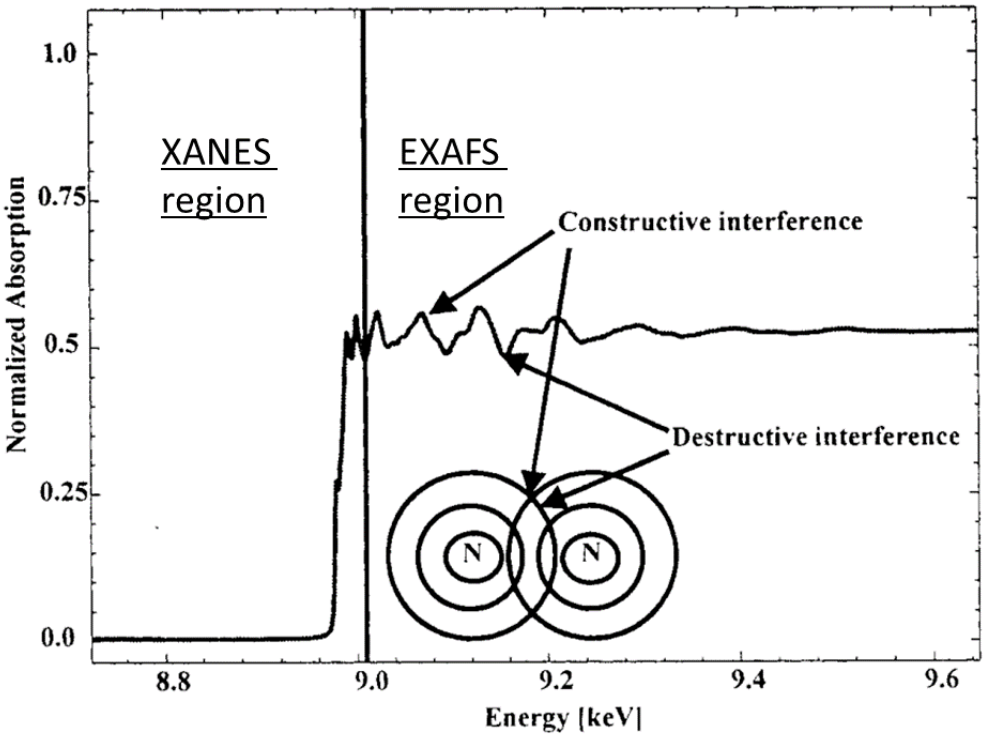

Figure 2.10 - k-edge XANES spectrum of Cu(0) foil. Adapted from literature.[184]

This region is called extended X-ray absorption fine structure (EXAFS) region and gives information on the coordination number and bond distance.[181, 185, 186]

2.5 Materials and Instrumentation

All reagents were purchased from Sigma Aldrich and, if not stated elsewise, used without further purification. All solvents were of analytical grade, and all water used in this work was Millipore Milli-Q 18 MΩ ultrapure and deionised. Lithium bis(trifluoromethanesulfonyl)imide was acquired from IoLiTec GmbH. All solvents used for the catalytic experiments were of HPLC / GC grade. Research grade hydrogen (99.999%) was supplied by BOC – LINDE GROUP. All ILs investigated herein were prepared in our laboratory using modified literature procedures.[187, 188]

All synthetized ILs were dried *in vacuo* ($p \leq 10^{-3}$ mbar) at 50 °C for 24 hours and stored under argon. The synthesized materials contained no detectable impurities and chemical structure desired that were evaluated using ^{13}C and ^{1}H NMR, mass spectrometry, IR, Ion Chromatography and XPS. Nuclear magnetic resonance (NMR) measurements were performed at room temperature in a NMR Bruker Ascend^{TM} 400 MHz Spectrometer; the chemical shift was referenced respect the Tetramethylsilane (TMS at 0 ppm) and the solvent position ($CDCl_3$ at 7.24 ppm and 77.23 ppm, DMSO solvent at 2.5 ppm and 39.5 ppm) for the ^{1}H and ^{13}C NMR, respectively. The coupling constants (*J*) are presented in Hz and the nomenclature used for the description of the multiplicity of the NMR signals is the following: singlet (s), doublet (d), double doublet (dd), triplet (tt) and multiplet (m). Other characterisation methods included: mass spectroscopy measurements, carried out in a Bruker ESI-TOF MicroTOF II. Infrared (IR), conducted using a Bruker Alpha (Fourier transform infrared) FTIR spectrometer with an ATR attachment. Data collection utilised 128 cumulative scans with a resolution of 4 cm^{-1} for the baseline and 256 cumulative scans with a resolution of 4 cm^{-1} for sample analysis. Ion Chromatography was used to evaluate the anion exchange and the presence of Chloride from precursor IL using a Dionex ICS-3000 fitted with AS20 analytical column and AG20 guard column. UV-vis absorbance spectroscopy was measured using a Cary 5000 UV-vis spectrophotometer (Agilent), equipped with a UV-Vis Internal Diffuse Reflectance sphere (Internal DRA-2500 PMT/PbS) using quartz cuvettes with a 1 mm path length. All ILs were then stored in a glove-box along with all metal containing samples.

2.5.1 Magnetron sputtering deposition

In a typical experiment, a round bottom flask containing IL inside the glove box is connected into a degassing mechanism for 2 hours. A small petri dish is tared and anhydrous IL (0.750 g) is weight into the petri dish. The load lock is filled with in an atmospheric pressure of nitrogen and the liquid sample holder containing the petri dish with IL is then transferred from the glove box into the load lock. The load-lock is pumped-down to a base pressure of 10^{-7} Torr for ca. 2 hour. After this, the sample holder is transferred to the main chamber where it rest for another 2 hours while the main chamber reaches the base pressure of 10^{-9} Torr. The target angle was set to 35° angle and the work distance to 120 mm. Then a flow of Argon is inserted into the main chamber until it reaches a working pressure of 3 mTorr. This working pressure was used in all depositions. The power sources potential and the length of deposition are programmed accordingly and the values used are presented in Chapter 3, after the calibration of the system. After the deposition, the sample is transferred back into the load lock and an atmospheric pressure of nitrogen is introduced to allow the transfer of the sample into the glove box. The sample is transferred into a vial, weighted and stored inside the glove box.

2.5.2 Inductively coupled plasma optical emission spectrometry

Inductively coupled plasma optical emission spectrometry (ICP-OES) was used to determine the amount of palladium and gold sputtered into the samples (%wt), metal content analysis was performed on a Perkin Elmer Optima 2000 DV Inductively Coupled Plasma Optical Emission Spectrometer. HCl (37% v/v) and HNO_3 (69% v/v) are ARISTAR™' grade and purchased from VWR Chemicals.

Calibration curves:

Calibration curves were prepared fresh using standard solutions of concentrations between 0.5 and 100 ppm prepared by dilution of commercially available ICP TraceCERT® palladium (10000 mg/L Pd in 5% HCl solution (% v/V in ultrapure water) and gold (1000 mg/L Au in 5% HCl solution (% v/V in ultrapure water) standards from Sigma Aldrich.

Analysis of samples:

Approximately, 20 mg of a sample (depending on predicated concentration of metal in sample) was accurately weighted in a flask, per each sample, in triplicate (3 X 20 mg). 300 mg of a solution of one part concentrated nitric acid and three parts concentrated hydrochloric acid (aqua regia) was added to each flask. After 24 h, the metals were completely dissolved in the solution. Afterwards, the obtained solutions were diluted and transferred into a 10 mL volumetric flask using a 5% HCl solution (% v/v in ultrapure water). The volumetric flasks were filled to the mark with this 5% HCl solution and the analysed using calibration curves with the appropriate calibration standards. Each sample was measured in 2 different wavelengths, with high sensitivity for each element. Wavelengths used for the determination of gold content in solution were 267.595 nm and 242.795 nm and for palladium 340.458 nm and 363.470 nm. The obtained values for the triplicates were averaged and then the error was determined using the standard deviation of the measures obtained.

2.5.3 TEM Sample preparation

TEM measurements were always (otherwise stated) carried out at the Nanoscale and Microscale Research Centre (NMRC) in a JEOL 2100F FEG-TEM with Oxford Instruments ISIS EDS analysis system operating at 200 kV. The samples were analysed in TEM and STEM modes. The samples were prepared by deposition onto a “Holey Carbon Films” on 300 mesh copper grids from Agar Scientific Ltd. TEM grids were prepared by altering the surface of the TEM grid by glow discharge (Agar Turbo Coater, 0.2 mbar, 5 mA, 10 secs) before the addition of the desired sample (1 µL). The sample was kept on the grid for 30 seconds before the excess was removed using filter paper. This alteration to the normal methodology enabled the formation of ‘pools’ of IL within the holes of the holey carbon, providing an effective contrast free region to observe the palladium structures. The size distributions and histograms were determined by measuring a minimum of 300 NPs on several images (maximum of 50 per image) using Gatan Microscopy Suite Software.

2.5.4 XPS Instrumentation

X-ray photoelectron (XPS) measurements were performed using a Kratos AXIS Ultra spectrometer instrument with a focused monochromated Al Kα source ($h\nu$ = 1486.6 eV) equipped with hybrid magnetic lens (magnetic/electrostactic), concentric hemispherical analyser (CHA), and a multi-channel plate and delay line detector (DLD). The X-ray gun power was set at 10 mA and 12 kV (120 W) in an incident angle of 30° relative to the sample holder. The energy range for each “pass energy” (resolution) was calibrated using the Kratos Cu $2p_{3/2}$, Ag $3d_{5/2}$, and Au $4f_{7/2}$ three-point calibration method. The transmission function was calibrated using a clean

gold sample method for all lens modes and the Kratos transmission generator software within Vision II. Samples were mounted on the standard Kratos sample bar and pumped down to 3×10^{-7} Torr overnight before transfer into the instrument analysis chamber. Wide energy range survey scans were collected at a pass energy of 80 eV in hybrid slot lens mode using an entrance aperture of 300 µm x 700 µm and a step size of 0.5 eV during 20 min. High-resolution data on the C 1s, N 1s, O 1s, F 1s, S 2p, Pd 3d, Au 4f, Au 4d and VB photoelectron peaks were collected at a pass energy of 20 eV over energy ranges suitable for each peak and collection times of 10 min, with step sizes of 0.1 eV. The collection times of Au 4d, Au 4f and Pd 3d was increased to 40 min. The charge neutralizer filament was used to prevent the sample charging over the irradiated area. The data were captured using Kratos VISION II software and exported into *.vms* format for data processing with CASAXPS (version 2.3.17). The high-resolution spectra were analysed using a GL (30) (70% Gaussian, 30% Lorentzian) or Lorentzian asymmetric line shape depending on the element. Background subtraction was obtained using a linear or Shirley background function. The high-resolution data were charge corrected to F 1s at 688.9 eV accordingly to literature.[180] The XPS analysis provides semi-quantitative analysis of each element at a minimum of one core level line per element (excluding hydrogen and helium) from these photoemission lines and peak position can be obtained as binding energy. This allows for element analysis detecting elements at atomic percentages of 0.1%. This value is referenced to elements with low photoelectron cross-section of the core levels, other elements can be detected at lower atomic percentages.[178]

2.5.5 XAS Instrumentation

The XAS measurements were conducted at B18, at Diamond Light Source, Didcot, UK of the AuPd NPs in IL. The samples were placed in an Eppendorf tube, as presented in Figure 2.11.

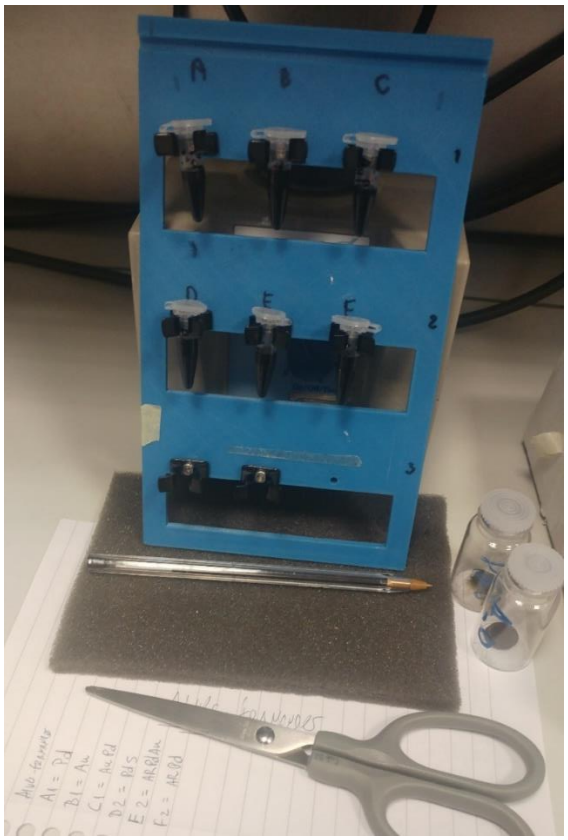

Figure 2.11 - XAS sample holder containing the AuPd NPs in IL samples placed in Eppendorf tubes without any pre-treatment.

XAS measurements were performed at the Pd K-edge in transmission mode equipped with an in-house build and designed four-bounce monochromator consisting of double (2X2) counter-rotating crystals Si(311) monochromator. The XAFS spectra were acquired using a Pd_{foil}, PdO, Au_{foil} and AuO as reference. Time resolution was 21 s spectrum^{-1} with k_{max} = 15.9 (maximum energy of the Pd K-edge photoelectron.[189]

EXAFS analysis was performed using IFEFFIT with the Horae package (Athena and Artemis). Athena software was used to calibrate, align, and normalize the spectra with respect to the Pd_{foil} standard (E_0 set at 24358 eV) and Au_{foil} standard (E_0 set at 11919 eV).

2.5.6 Catalytic tests

The catalytic tests were performed in a Fisher-Porter reactor system build in-house, in the School of Chemistry workshop and equipped with a sampling loop of 0.1 mL enabling the collection of reaction aliquots over time without depressurizing the reactor (Figure 2.12).

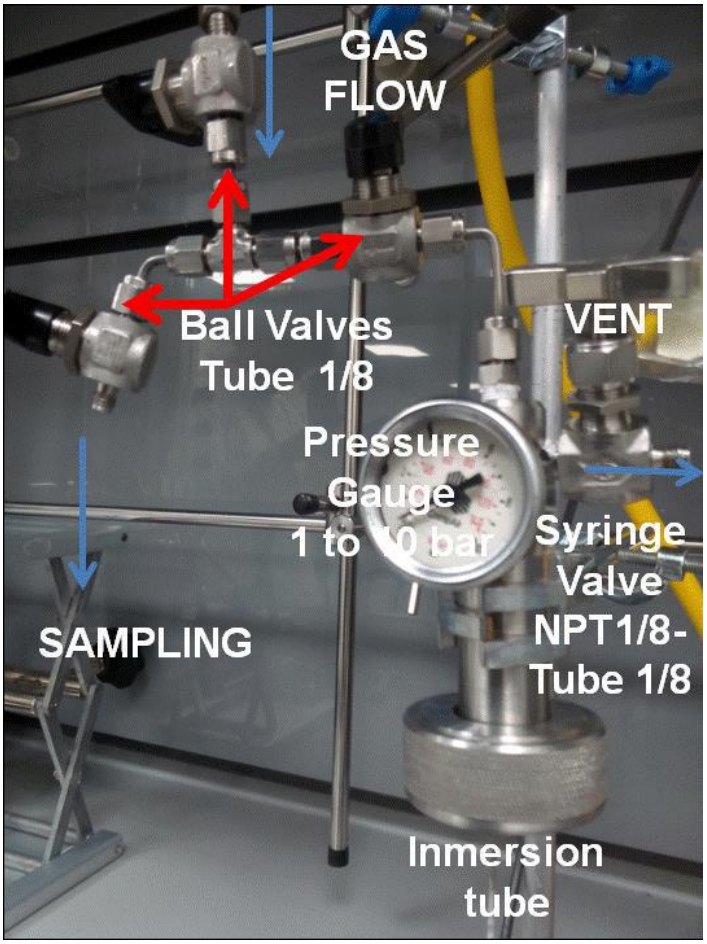

Figure 2.12 - Fisher-Porter reactor used to carry out the catalytic tests equipped with sample loop.

The Fisher-Porter reactor system has a maximum volume of 22 mL and was rated to a max pressure of 22 bar. During the initial testing of the system (temperature, pressure, solvent) a reaction media volume of 2 mL was used, whereas for the subsequent reaction which required sampling (kinetic tests), 10 mL reaction media were used. The hydrogenation reactions used 0.1% mol catalyst and tridecane as internal standard was added to the reaction media to enable the accurate quantification. All reactions were performed, between 1 - 10 bar of hydrogen, between R.T. to 50 ˚C and stirred at 600 r.p.m. Dried solvents were used for the reactions and added to a vial containing the catalyst, in inert atmosphere. Substrate and internal standard were inserted into the vial using a weight syringe. The reaction media was inserted into the reactor and flushed 3 times with H_2 before setting the desired pressure. Aliquots were taken in frequent intervals by the sampling loop without allowing the pressure inside the reactor to reach atmospheric pressure. The sample loop was flushed with H_2 to avoid reaction media losses and increase accuracy. Aliquots and end-of-reaction samples were diluted 1:1 in dried solvent and were evaluated by gas chromatographic (GC) to determine the conversion, Turn-Over Number (TON) (equation 3), Turn-Over Frequency (TOF) (equation 4) and selectivity (equation 5).

$$TON = \frac{\text{moles of product formed}}{\text{number of moles of catalyst}}$$ *Equation 3 – Turnover number.*

$$TOF = \frac{TON}{reaction\ time}$$ *Equation 4 – Turnover frequency.*

$$Selectivity = \frac{\text{moles of desired product}}{\text{Sum of moles of all products}}$$ *Equation 5 – Selectivity.*

The catalytic reactions were evaluated using both a gas chromatograph equipped with a flame ionisation detector (GC-FID) and a gas chromatograph equipped with a mass spectrometry detector (GC-MS). The GC-FID analysis were used to quantify the reaction products whereas the GC-MS analysis were used to identify the products and their retention times. GC-FID analysis were performed in a Thermo Trace 1310 using He (constant flow of 20 mL min^{-1}) gas as the carrier with the TG17MS column (30 m × 0.25 mm × 0.25 μm), temperature of the injector and detector was 300 °C, and the following program of oven temperatures: 40 °C (hold 10 min) to 260 °C (hold 5 min) at a heating rate of 10 °C min^{-1}. The GC-MS analysis were performed using a Thermo Trace 1310 coupled to an ISQ LT (MS) detector. The used column on the GC-MS was identical to the column used for GC-FID analysis. All parameters were maintained when possible and MS Ion source used an ionization energy of 75 eV and a temperature of 200 ºC.

2.5.7 ILs synthesis

1-n-Butyl-3-methylimidazolium Chloride, $[C_4C_1Im]Cl$[187]

To a solution of 1-methylimidazole (10.2 ml, 128.4 mmol) in acetonitrile (25 ml), 1-chlorobutane (16.0 mL, 153.9 mmol) was added dropwise with stirring (600 RPM) at room temperature. The reaction mixture was heated to 40 °C in a round neck

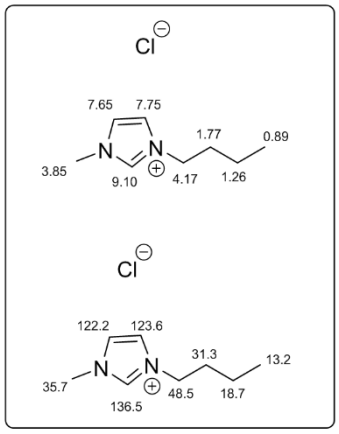

bottomed flask fitted with a reflux condenser and continuous stirring (600 RPM) for 48 h. A biphasic mixture was formed with the top layer containing unreacted material (decanted). Ethyl acetate was added (50 mL) with comprehensive mixing and left to settle before being decanted. This procedure was repeated twice to eliminate unreacted material. The crude solid was recrystallized twice using in a mixture of acetonitrile/ethyl acetate. The supernatant solvent was decanted and the obtained product was dried *in vacuo* (at 7.0 x 10^{-4} mbar) using an intermediate secondary trap (first 8 hours) at 50 °C for 48 h to yield a white hygroscopic solid (16.19 g, 72.2%) with a melting point of 70 °C.

^{1}H NMR (400 MHz, DMSO-d_6) δ (ppm): 0.89 (t, J = 7.4 Hz, 3 H), 1.26 (sxt, J = 7.4 Hz, 2 H), 1.77 (tt, J = 7.4 Hz, 2 H), 3.85 (s, 3 H), 4.17 (t, J = 7.4 Hz, 2 H), 7.65 (t, J = 1.8 Hz, 1 H), 7.75 (t, J = 1.8 Hz, 1 H) and 9.10 (s, 1 H).

^{13}C NMR (100 MHz, DMSO-d_6) δ (ppm): 13.2, 18.7, 31.3, 35.7, 48.5, 122.2, 123.6, 136.5.

IR, *v* (cm^{-1}): Bending (O-H): 1640 cm^{-1}; Stretching (O-H): 3450 cm^{-1}, Stretching (C-H): 3000-3100 cm^{-1}; Bending (C-H): 1350-1480 cm^{-1}; Stretching (C-H): 2850-3000 cm^{-1}; Stretching (C=N): 1080-1360 cm^{-1}; Stretching (C=C): 1400-1600 cm^{-1} (*Appendix 1*)

ESI-MS (+ve) $[C_8H_{15}N_2]^+$ calcd: 139.1232; found: 139.1245

Data in agreement to literature.[187]

1-n-Butyl-3-methylimidazolium bis(trifluoromethanesulfonyl)imide, $[C_4C_1Im][NTf_2]$ [187, 188]

To a stirring (600 RPM) solution of $[C_4C_1Im]Cl$ (10 g, 57.2 mmol) in ultrapure water (70 mL), a solution of Lithium bis(trifluoromethane)sulfonimide (1.1 eq, 18.1 g, 62.9 mmol) in ultrapure water (50 mL) was added dropwise, at room temperature. The resulting reaction mixture was stirred for 24 hours at room temperature. Dichloromethane (100 mL) was added and the organic layer extracted by liquid/liquid separation and washed with ultrapure water (4 x 20 mL) to remove unreacted material. The solvent was removed under *vacuo* (7.0 x 10^{-4} mbar) at 50 °C for 48 h using an intermediate secondary trap yielding a colourless liquid (45.5 g, 94.6%).

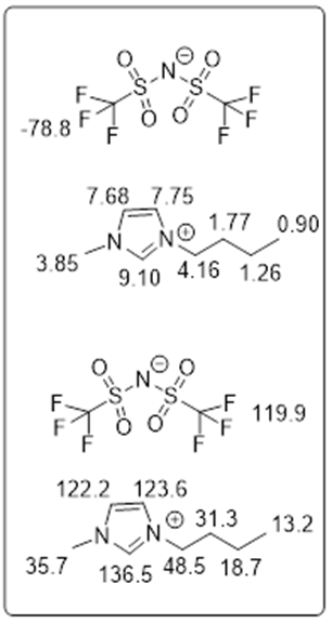

^{1}H NMR (400 MHz, DMSO-d_6) δ (ppm): 0.90 (t, J = 7.4 Hz, 3 H), 1.26 (sxt, J = 7.4 Hz, 2 H), 1.77 (tt, J = 7.4 Hz, 2 H), 3.85 (s, 3 H), 4.16 (t, J = 7.4 Hz, 2 H), 7.68 (t, J = 1.8 Hz, 1 H), 7.75 (t, J = 1.8 Hz, 1 H), 9.10 (s, 1 H).

^{13}C NMR (100 MHz, DMSO-d_6) δ (ppm): 13.2, 18.7, 31.3, 35.7, 48.5, 119.9 (q, J = 322 Hz, -CF_3), 122.2, 123.6, 136.5. **^{19}F NMR** (377 MHz, DMSO-d_6) ($[C_4C_1Im]$ $[NTf_2]$) - δ (ppm): -78.8 (s, 6 F)

IR, *v* (cm^{-1}): Stretching (C-H): 3000-3100 cm^{-1}; Bending (C-H): 1350-1480 cm^{-1}; Stretching (C-H): 2850-3000 cm^{-1}; Stretching (C=N): 1080-1360 cm^{-1}; Stretching (C=C): 1400-1600 cm^{-1}; Stretching (S=O): 1060 cm^{-1}; Stretching (C-F): 1200 cm^{-1}.

ESI-MS (+ve) $[C_8H_{15}N_2]^+$ calcd: 139.1232; found: 139.1245

ESI-MS (-ve) $[C_2F_6NO_4S_2]^-$ calcd: 279.9173; found: 279.9180

Karl Fischer Titration: 8.5 ppm of water.

Ion Chromatography: < 1% Chloride

Data in agreement to literature.[187, 188]

CHAPTER THREE

Characterisation and mechanisms leading to the formation of the AuPd NPs in IL

3. Characterisation and mechanisms leading to the formation of the AuPd NPs in IL

3.1 Introduction

The size, shape and composition of a NP plays a significant role in their catalytic activity, selectivity and stability. It is well-known and accepted that the chemical properties of bimetallic NPs are often different from those of the monometallic constituent metals present.[190] In bimetallic AuPd NPs, a comprehensive study of the chemical state and electronic structure is crucial to bridge these properties to their catalytic performance on chemical reactions.[191] The deposition of bimetallic NPs directly into liquid supports by magnetron sputtering has attracted extensive attention in recent years.[107, 192-194] Torimoto and Kuiwabata deposited PtAu NPs into ILs using a binary target with a wide range of compositions,[118] with PtAu NPs being sputtered from the target directly into the IL, being able to obtain bimetallic NPs with good distribution and with similar composition to the target from which it was originated. PtAu bimetallic NPs with varied composition have been synthesized by co-deposition using independent targets onto liquid PEG.[119] However, the mechanisms leading to the formation of bimetallic alloy NPs using magnetron sputtering remain poorly understood.[120-122] For instance, whether the bimetallic formation occurs in the gas-phase or in the IL surface/near-surface is still debated. In this thesis, the formation of bimetallic NPs is carried out using co-deposition mode, where two targets are sputtered simultaneously at independent power. The use of this methodology enables a high level of control of bimetallic NPs composition.[119] In the first section of this chapter, the calibration of both Pd and Au on the magnetron deposition system

is described and the steps taken to obtain the bimetallic AuPd NPs in $[C_4C_1Im][NTf_2]$. The AuPd NPs in IL were characterised by electron microscopy, UV-Vis, XPS, and XAS in the follow section. By the end of this chapter a model for the formation of the AuPd NPs using magnetron sputtering in IL is proposed based on the characterisation results.

3.2 Magnetron sputtering system calibration

The production of bimetallic AuPd NPs requires careful calibration of the deposition rates of each metal separately, as different target composition (i.e. gold, palladium) will behave differently due to their distinct sputtering yield. The sputtering yield for a given target material is described as the number of atoms ejected per incident argon ion. This value depends on the atomic mass of both the sputtering gas ions and the target, on the crystalline structure of the target, on the energy they both possess at the moment of impact and on the target's composition. Hence, the momentum transfer will vary and the kinetic energy of the sputtered atoms will differ between different targets. When setting up the experiment, power (Watts) can be pre-settled. This is a function of potential (Volts) times current (amperes), where the potential translates into the kinetic energy of the Argon ions and the current on the number of argon ions with the same kinetic energy being accelerated per second. This way, the power applied into the target is known and the relation between the power and metal content introduced into the IL determined. This way, the first step in creating a co-deposition methodology was to determine the deposition rate for each metal (Pd and Au) by using different deposition times and fixing the other parameters (such as power, target angle, work distance, gas pressure and amount of IL). The metal content was measured using standard ICP

methodology, taking 3 samples from each deposition and averaging the values obtained. The system's reproducibility was assessed, producing triplicates of all depositions and their standard deviation. From previous work in our group, it is known that the rate deposition of Pd is half of the Au, which is independent of the magnetron sputtering system. Therefore, the calibration of Pd was performed using a power of 60 W, whereas for Au 30 W was used.[14, 109] The relative low power used in this system aimed to obtain a lowest deposition rate possible, creating discrete species (atoms, dimers and trimers) and minimise the in-flight collision of Au-Au or Pd-Pd sputtered atoms.[195, 196]

3.2.1 Pd calibration

The Pd calibration started with a single deposition using direct current (60 W) for 10, 30, 50 and 60 min. TEM images presented well defined Pd NPs with a narrow size distribution (Figure 3.1 a,b). The concentration of Pd in IL increased linearly with deposition time, as expected (Figure 3.1 c). The linear rate of deposition indicates high reproducibility of the system over a broad range of deposition times (R^2=0.9996) and a deposition rate of 0.017% Pd (w/w) / min in IL.

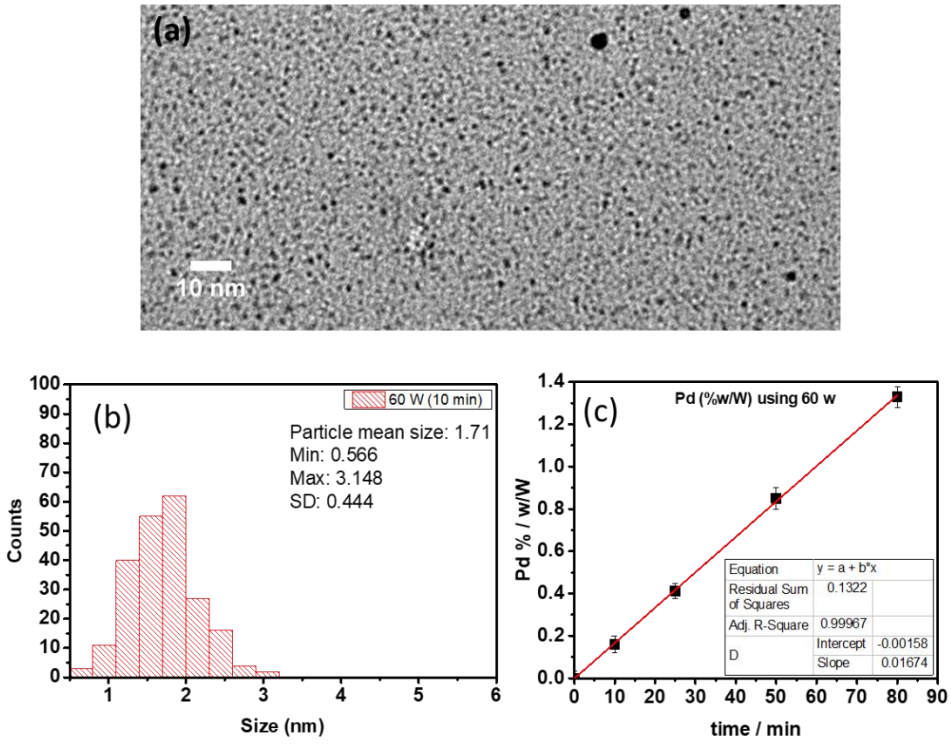

Figure 3.1 – TEM (a) and size distribution (b) of the Pd NPs present in the IL after 10 minutes of deposition at 60 W, (c) averaged % Pd (w/w) measured by ICP-EOS of the samples produced with different times of deposition and a power of 60 W.

3.2.2 Au calibration

The determination of the Au NPs deposition rate followed the same procedure as the Pd NPs. System calibration was undertaken by varying the deposition time, while maintaining other conditions.

The TEM images shows well-defined Au NPs with a narrow size distribution (Figure 3.2 a, b). Similarly to the Pd NPs deposition, the concentration of Au in IL increased linearly with deposition time as expected (Figure 3.2 c). The linear rate of deposition indicate the high reproducibility (R^2=0.9996) of the system over a broad range of deposition times and the deposition rate was determined to be 0.012% Au (w/w) / min.

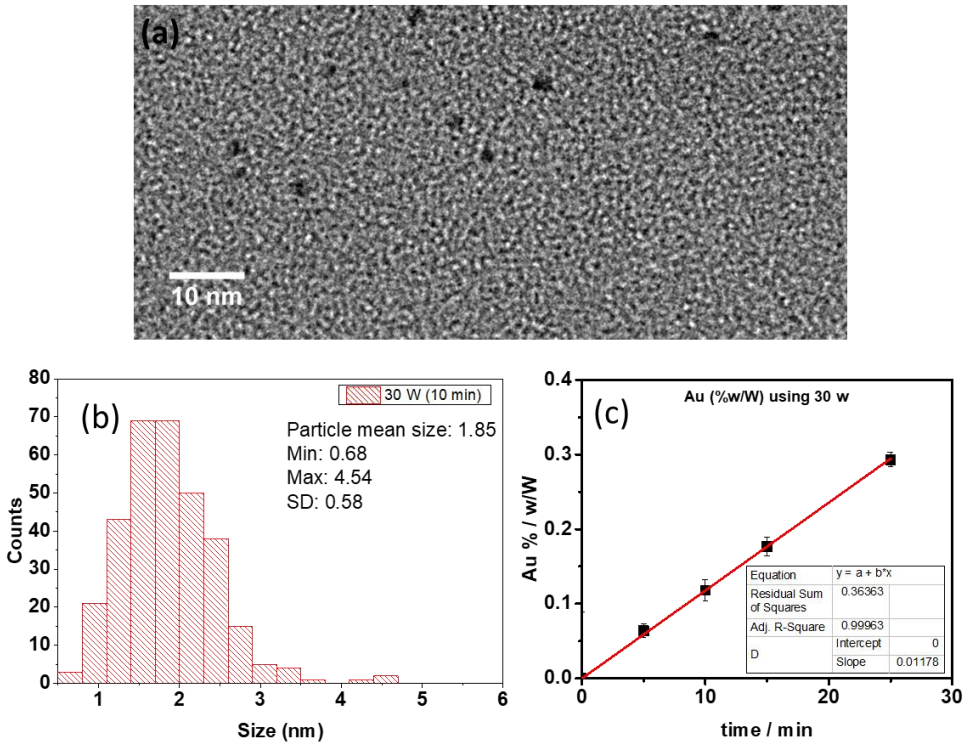

Figure 3.2 - TEM (a) and size distribution (b) of the Au NPs present in the IL after 10 minutes of deposition at 30 W, (c) averaged % Au (w/w) measured by ICP-EOS of the samples produced with different times of deposition and a power of 30 W.

3.2.3 Production of the bimetallic AuPd NPs in IL

In order to form AuPd bimetallic NPs by magnetron sputtering, two parameters are crucial: *i*- the relationship between Pd and Au deposition rates to be able to control the composition of the samples; *ii*- the angle between the two targets in order to increase the probability of in-flight collision of the sputtered atoms of Au and Pd thus forming AuPd dimers or trimers before reaching the substrate (Figure 3.3). As presented previously, the deposition rate of gold at 30 W (0.012% Au (w/w) / min) and Pd at 60 W (0.017% Pd (w/w) / min) were experimentally determined. The angle between the targets was empirically settled using a previous experience from our group.

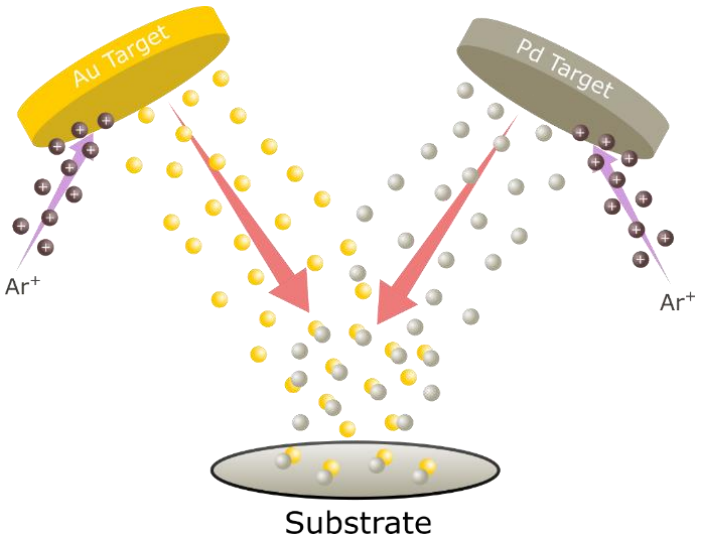

Figure 3.3 – Scheme of co-deposition of AuPd NPs by magnetron sputtering co-deposition.

In order to produce AuPd NPs, the Pd concentration was fixed, by maintaining a constant power on the Pd target and 50 min depositions. The power on the Au target was consequently varied to match different ratios of metal. In this fashion, various mono – and bimetallic AuPd NPs (Au_1; $Au_{0.75}Pd_{0.25}$; $Au_{0.50}Pd_{0.50}$; $Au_{0.40}Pd_{0.60}$; $Au_{0.25}Pd_{0.75}$; Pd_1) were produced. The magnetron sputtering NPs deposition in IL conditions can be found in Table 1. It is important to note that $Au_{0.80}Pd_{0.20}$ particles are obtained under longer deposition time (180 min), using a lower power for the Pd (30 W) target and an increased power for Au (120 W).

Table 1 - Magnetron sputtering parameters for Au NPs deposition in IL. Depositions were performed in triplicate. Voltage and current used for these deposition are presented in Appendix 2.

Sample	Au (wt%)	Pd (wt%)	Pd (At %)	Au (At %)	Power Pd (W)	Power Au (W)	Deposition time (min)
Au_1	0.94 (±0.035)	0.00	0.0	100	0	30	50
$Au_{0.80}Pd_{0.20}$	6.82 (±0.040)	0.85 (±0.041)	18.7	81.3	30	120	180
$Au_{0.50}Pd_{0.50}$	1.43 (0.035)	0.85 (±0.024)	52.4	47.6	60	90	50
$Au_{0.40}Pd_{0.60}$	0.94 (±0.022)	0.85 (±0.023)	62.6	37.4	60	30	50
$Au_{0.25}Pd_{0.75}$	0.53 (±0.015)	0.87 (±0.034)	75.3	24.7	60	15	50
Pd_1	0	0.85 (±0.022)	100	0.0	60	0	50

The low standardised error obtained showcases the high reproducibility and robustness of this approach. The characterisation of the AuPd NPs in IL materials is presented subsequently in the chapter and their catalytic properties are shown on chapter 4 and 5.

3.3 AuPd NPs deposited into IL: dispersion and size distribution

The AuPd NPs dispersion and size distribution were investigated by TEM (Figure 3.4).

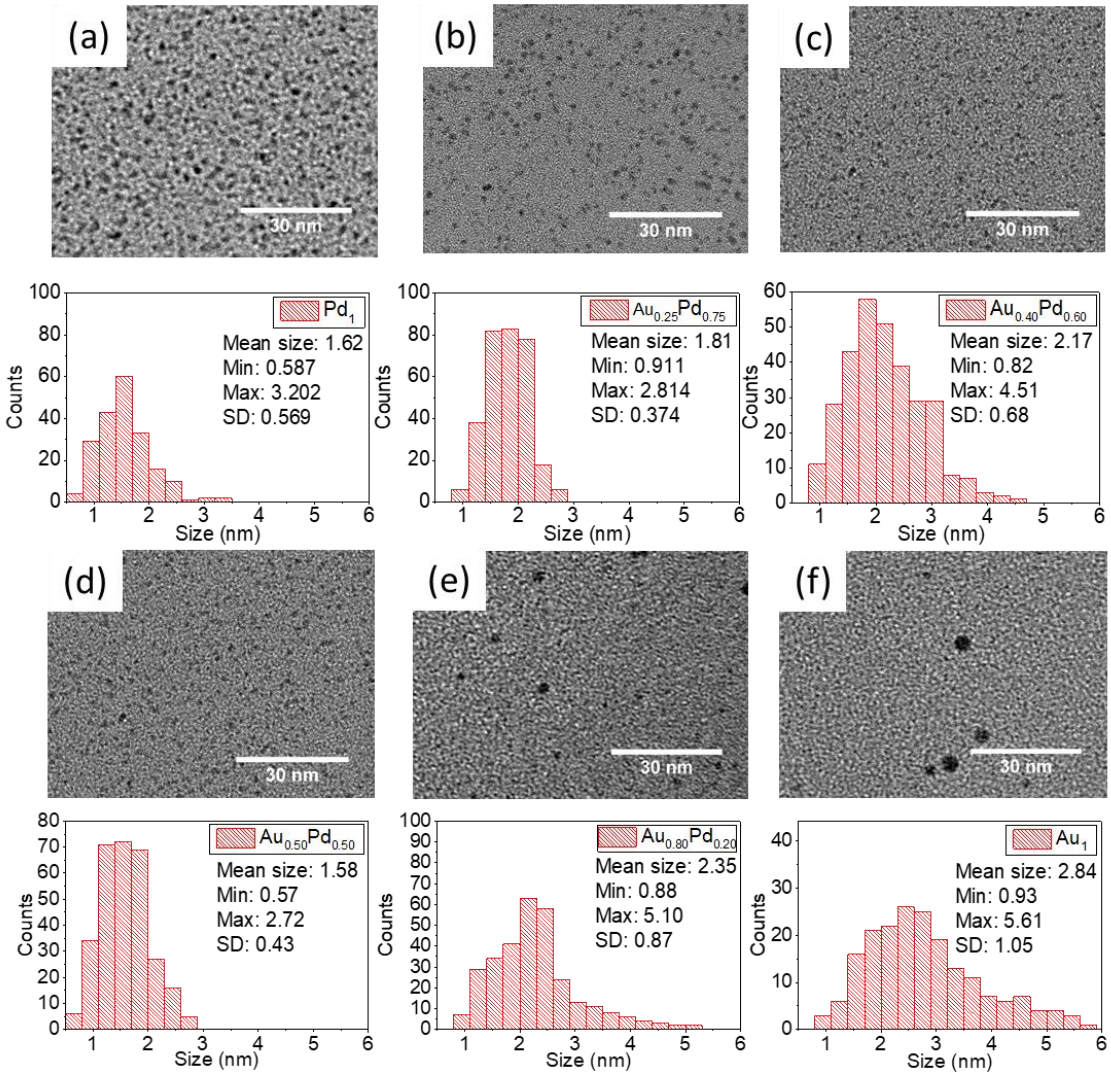

Figure 3.4 –TEM images of AuPd NPs sputtered into IL a) Pd_1, b) $Au_{0.25}Pd_{0.75}$, c) $Au_{0.40}Pd_{0.60}$, d) $Au_{0.50}Pd_{0.50}$, e) $Au_{0.80}Pd_{0.20}$ and f) Au_1. These samples were produced by magnetron sputtering according to conditions presented in table 2 of this chapter. The size distribution histogram (below each TEM image) was obtained by counting 300 NPs from a minimum of 7 images for each sample.

TEM images of the AuPd NPs sputtered into IL display well-defined, round shaped NPs in all cases. When focusing on the monometallic samples Pd_1 and

Au_1, both samples present well defined shape with Au_1 displaying a larger polidispersion and larger mean size diameter when compare to Pd_1 (± 1 nm) (Figure 3.4 a and f). This tendency is also observed for $Au_{0.25}Pd_{0.75}$, $Au_{0.40}Pd_{0.60}$ and $Au_{0.80}Pd_{0.20}$ with values in-between in the following order Au_1 > $Au_{0.80}Pd_{0.20}$ > $Au_{0.50}Pd_{0.50}$ > $Au_{0.40}Pd_{0.60}$ > $Au_{0.25}Pd_{0.75}$ and Pd_1 (Figure 3.4 b-e). The variation of the Au_xPd_{1-x} NPs mean diameter size with the increase of Au content is shown in Figure 3.5.

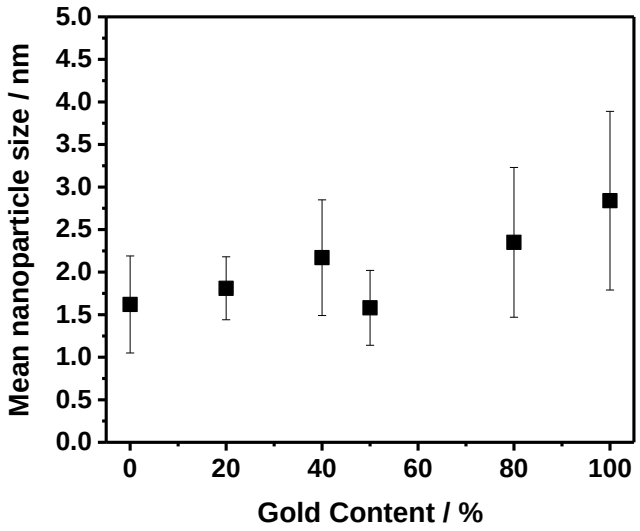

Figure 3.5 - Variation of the mean size distribution of the AuPd NPs sputtered into IL with the increase of Au content.

In Figure 3.5, the increase of the mean size distribution of the AuPd NPs sputtered into IL is presented showing the increase of the average of the NPs with the content of Au. All materials follows this trend with the exception of the $Au_{0.5}Pd_{0.5}$. The larger error bars found in Figure 3.5 for the increase of the NP size with the Au content were also observed by previous reports.[119] For instance, similar behaviour was observed for the AuPt NPs produced by magnetron sputtering into polyethylene glycol (PEG).[119] The authors report the

preferential adsorption of Pt on PEG than Au due to the higher adsorption energy of PEG-Pt (0.20 eV) in comparison to PEG-Au (0.12 eV), where Pt and Au atoms are preferentially coordinated via oxygen groups of PEG. This led to a narrow dispersion and size distribution of NPs with higher Pt concentration compared to NPs with higher Au concentration.[119] It is well-know that the stabilisation of metal NPs in IL is mainly dominated by the NTf_2 anion.[197] Therefore, it is reasonable to propose a similar mechanism for AuPd NPs deposited in IL, where a higher interaction between the oxygen containing SO_2 groups of the IL anion and Pd atoms leads to the narrow dispersion and size distribution for NPs with higher Pd content in comparison the ones with higher Au content.[58, 197] This interaction would not exclusively be responsible for the for the size distribution of the NPs, the magnetron deposition conditions should enable the formation of smaller entities (dimers and trimers), that upon arrival on the IL surface, could be stabilised by the IL-NP interaction. This IL-NP interaction was also observed by Zhu *et al.*, when evaluating AuPd alloyed catalysts produced by wet-chemistry.[20] This suggested stabilisation is further investigated by XPS and XAS.

3.4 AuPd NPs in IL: NPs composition and structure

Aberration corrected transmission electron microscopy (AC-STEM)coupled with Energy Dispersive X-Ray Analysis (EDX) produces an atomic resolved elemental composition (mapping) of the AuPd NPs. This can provide information on Au and Pd atoms distribution in the AuPd NPs, and therefore insights on AuPd NPs in IL nanostructure. AC-STEM EDX mapping measurements were performed using same sample preparation used for TEM,

where a drop of IL is deposited in the TEM grid forming a thin “ILs pools” in the carbon film holes (Figure 3.6).

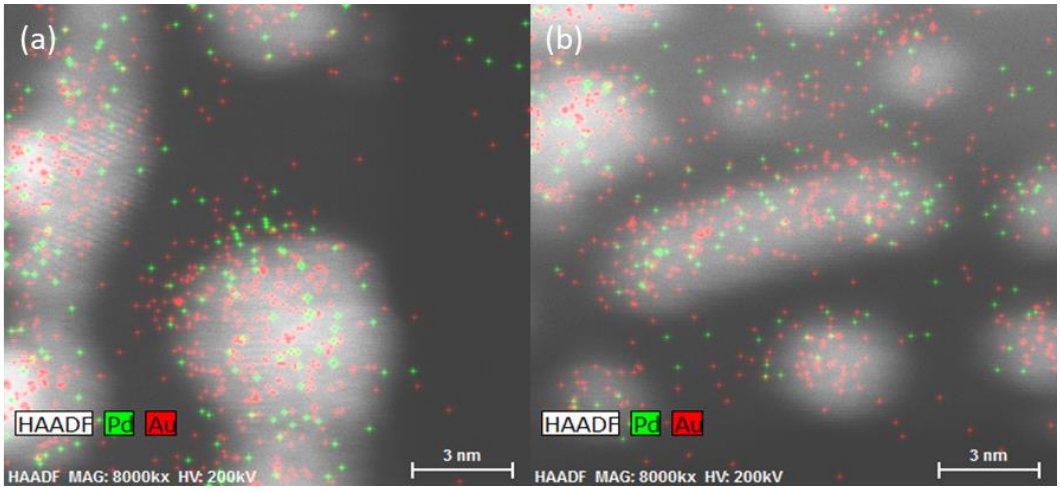

Figure 3.6 - EDX mapping of the sample $Au_{0.5}Pd_{0.5}$ overlaid with respective AC-STEM image prepared by directly adding AuPd NPs into the TEM grid, forming a film (procedure described in chapter 2.5).

In Figure 3.6, the elemental mapping (green and red dots) is not matching the position of the NPs overlaid, which was caused by the NPs drifting under the electron beam due to the excess of IL surrounding the NPs.[198 117, 199, 200] Due to the limited access to the STEM facilities, different approaches could not be extensively carried out. Moreover, certain approaches, such as washing out the IL excess, was carried out as an attempt to fix this issue. However, this could risk changing the AuPd NPs structure and stabilisation, jeopardising the experiment. Therefore, a more detailed mechanism for bimetallic AuPd NPs formation is proposed by the end of this chapter after gathering all information from UV-Vis, XPS and XAS.

3.5 AuPd NPs in IL: under UV-VIS

The formation of bimetallic AuPd NPs provides different electronic and optical properties compared to monometallic Pd_1 and Au_1.[201, 202] For instance,

when electromagnetic radiation is incident on monometallic NPs, such as Au, Ag and Cu, it leads to a localised excitation of the surface plasmon resonance (LSPR). This excitation leads to local magnetic enhancement due to the collective oscillation of surface conduction electrons – a resonance.[203] The effects of this resonance are very noticeable in Au NPs with several studies describing their size and shape dependency.[204, 205] Whereas for Pd, given the size of NPs produced in this work, the resonance contribution is not noticeable. In Figure 3.7, the obtained UV-VIS spectra for the monometallic samples Pd_1 and Au_1 is presented.

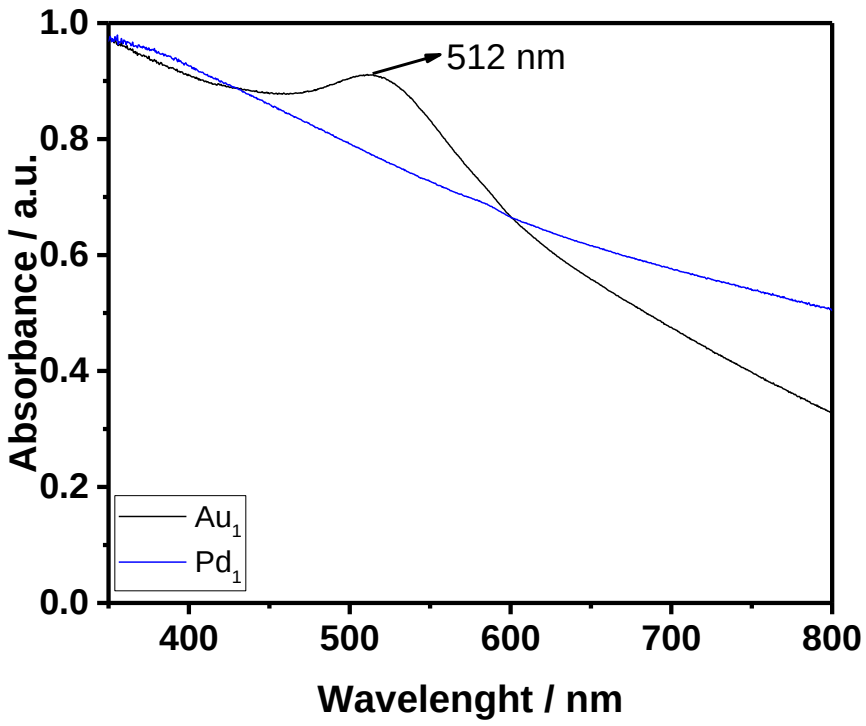

Figure 3.7 - UV-Vis spectra of the Pd_1 and Au_1 NPs in IL via transmission mode (cuvette path length of 1 mm) without addition of solvents.

In Figure 3.7, it is discernible that only the specimen Au_1, presents plasmon resonance peak between 510 and 520 nm for Au NPs,[206] whereas the Pd_1 NPs

presents no surface plasmon resonance, as expected.[206] In Figure 3.8, a UV-Vis spectra comparing all the AuPd NPs in IL is shown.

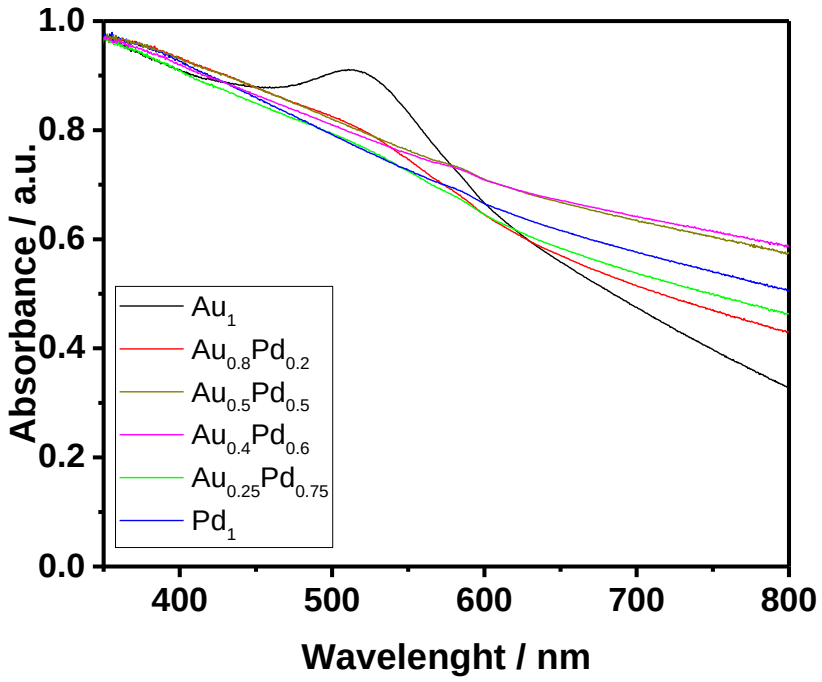

Figure 3.8 – UV-Vis spectra of the AuPd NPs in $[C_4C_1Im][NTf_2]$ via transmission mode (cuvette path length of 1 mm) without addition of solvents.

When comparing all the AuPd NPs in IL: $Au_{0.8}Pd_{0.2}$, $Au_{0.5}Pd_{0.5}$, $Au_{0.4}Pd_{0.6}$, $Au_{0.25}Pd_{0.75}$ and the respective monometallic counterparts, it is observable that the presence of Pd cancels the effect of the LSPR on the NPs, even at lower ratios. The presence of the LSPR is only observable in the Au monometallic counterpart. This indicates the formation of AuPd NPs alloy-like structure, as the addition of Pd into the nanostructures affects LSPR absorption of Au, decreasing it drastically with the cancellation of the collective oscillation of surface conduction electrons. However, the formation of core-shell structure cannot be dismissed, as the formation of an Au@Pd with an outer shell of Pd

would not possess a plasmon resonance for the presented NP size.[206, 207] Therefore, the results obtained suggest the formation of an alloy-like structure without dismissing the possible core-shell structure.

3.6 AuPd NPs in IL: electronic properties

XPS was used to evaluate the surface composition of AuPd NPs and to investigate their interactions with the IL ($[C_4C_1Im][NTf_2]$).[176] A comparison of the wide scans and high resolution scans of all elements present in the AuPd NPs deposited in IL is presented in Figure 3.9. The individual wide scans and high resolution scans for each AuPd NPs in IL are presented in Appendix 3 and 4 with the respective biding energy values and FWHM. The high resolution data was charge corrected to the reference F 1s signal at 688.9 eV due to the relative stability of the fluoride, as reported previously by our group.[180, 208]

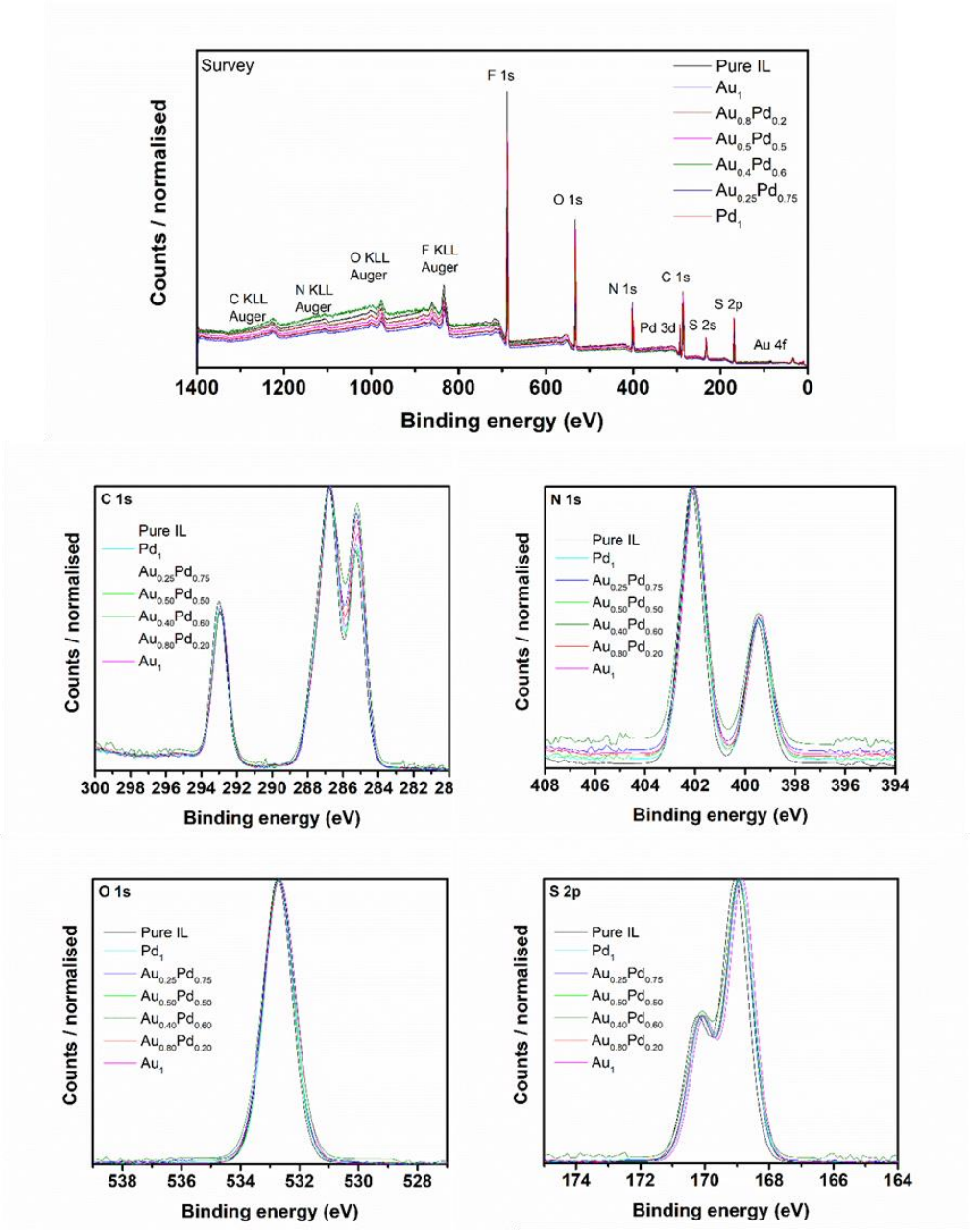

Figure 3.9 – Normalised XPS spectra of wide scan, C 1s, N 1s, O 1s and S 2p from the AuPd NPs NPs in IL overlaid for comparison. The binding values and FWHM for all elements are presented in Appendix 4.

The elements corresponding to the $[C_4C_1Im][NTf_2]$ IL present almost no alteration after the deposition of the AuPd NPs; no binding shift, broadening of the components or presence of impurities was observed (Figure 3.9). The only noticeable alteration is present on the aliphatic carbon of the cation, showing

a minimal increase in the intensity of the aliphatic carbon at the surface. This marginal variation could be associated to a surface effect leading to a rearrangement of the IL aliphatic chain due to AuPd NPs presence. Nonetheless, given the low concentration of metal in the samples (0.8 % atomic percentage of Pd), the expected impact of the introduction of metal on the considerable more abundant IL was predicated to be absent, as presented in Figure 3.9. In Figure 3.10, the Pd 3d and Au 4f spectra obtained for Pd_1 and Au_1 is presented, respectively.

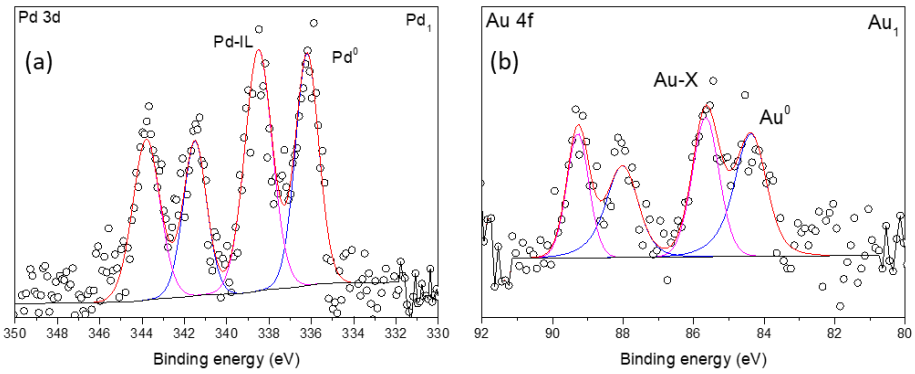

Figure 3.10 - Spectra of the Pd 3d (a) and Au 4f (b) regions of the Pd_1 and Au_1, respectively. The binding values and FWHM for all elements are presented in Appendix 4.

The XPS data of Pd 3d presented in Figure 3.10a displays the expected component for the Pd^0 at 336.1 eV (± 0.1 eV). This component presents a slight shift towards higher binding energy due to different electronic configurations between Pd bulk (metallic) and Pd NP, as the Pd bulk decreases the binding energy, as expected, from atom-like to bulk-like materials.[109, 209] This effect is due to the lower coordination number of surface atoms in small NPs which lead to an increase on binding energy.[210-213] A second component, at higher binding energy, was also observed at 338.5 eV

(± 0.1 eV). This shift to higher binding energy infers the interaction of Pd atoms with electronegative elements, resulting in higher energy required to remove a 3d electron. This second component appears to correspond to Pd interacting with the IL or sharing electron density. This Pd-X component is previously reported to represent the interaction of Pd with an oxygen containing group.[20] In the cases of Au_1 and Pd_1, this charge can only be shared by surface atoms of the IL. As previously described, the IL anion preferentially interacts with metal NPs,[214] hence we can assume the interaction of the SO_2 groups of the IL anion with the Pd. This way, the second component in both metals should be attributed to the interaction of Pd-IL and Au-IL.[58] In the Au 4f spectra of the sample Au_1, the Au also presents another component at 85.7 eV (Au-X), with similar area to the Au^0 component at 84.3 eV, hinting to the same Au-O interaction observed in the Pd 3 d spectra. In Figure 3.11, the Pd 3d and Au 4f for all AuPd NPs in IL are compared.

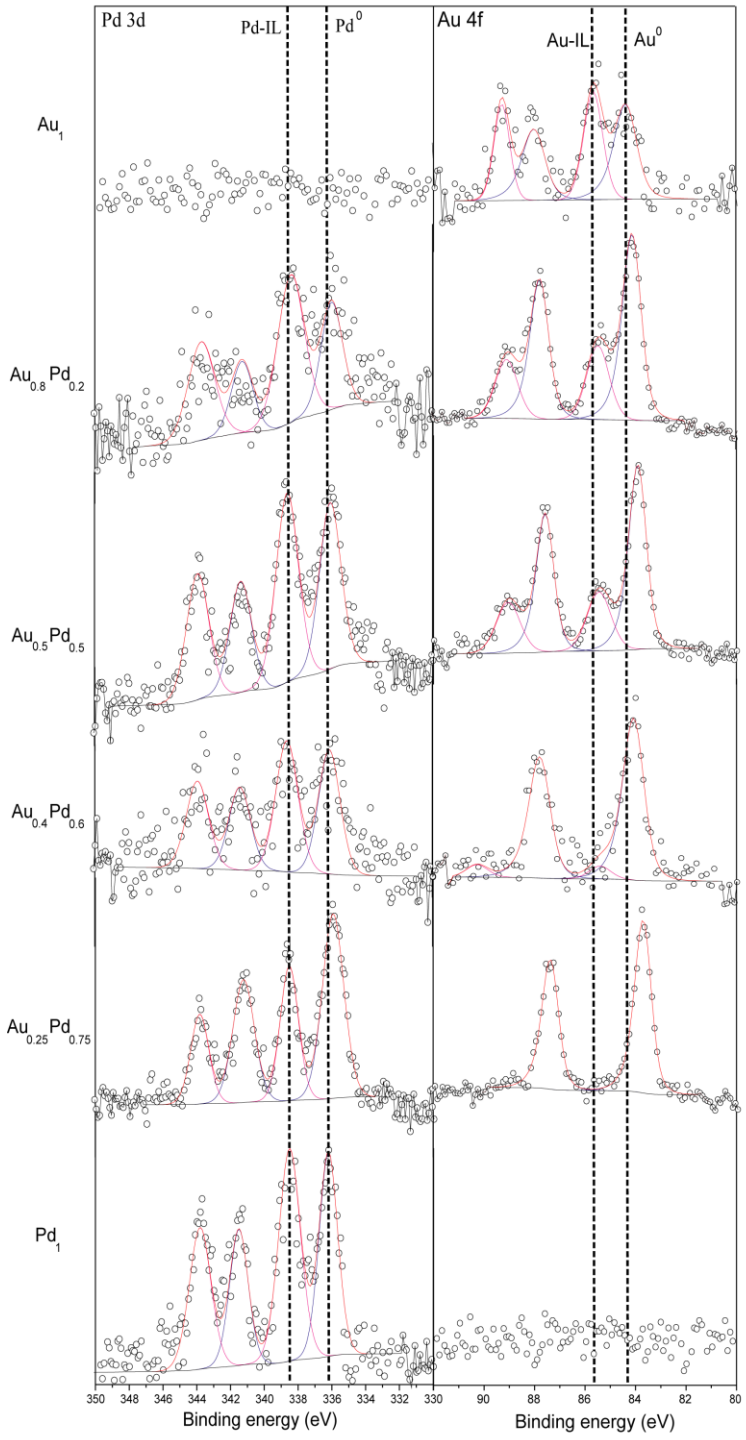

Figure 3.11 – Spectra of the Pd 3d and Au 4f regions of the AuPd NPs in IL. The binding values and FWHM for all elements are presented in appendix 4.

In Figure 3.11, as the ratio of Pd/Au increases, the second component on the Au 4f spectra, indicating the interaction of the Au with the IL anion, disappears. As for the Pd 3d spectra, the secondary component is maintained stable. The

increase of Pd ratio on the samples leads to the decrease of the second component in the following order: Au_1 > $Au_{0.8}Pd_{0.2}$ > $Au_{0.5}Pd_{0.5}$ > $Au_{0.4}Pd_{0.6}$ > $Au_{0.25}Pd_{0.75}$. The decrease of the Au-IL component with the increase of Pd content suggests the arrangement of both metals, with Pd on an outer shell and still interacting with the IL anion and Au in an inner shell, shielded from the IL. Alternatively, this behaviour could be indicative of the presence of an alloy with Pd sharing its electronic environment with Au, as referenced previously, due to the higher electronegativity of Au versus Pd.[20] A shift in binding energy of the Au^0 component (0.6 eV) to lower energies (Au metallic behaviour) is also observable with the increase of Pd content reinforcing the interaction of the Pd and Au atoms in the AuPd NPs.[20] Given Au presents higher electronegativity (2.4) in respect to Pd (2.2), Pd is expected to share its electronic density with the Au^0, thus lowering the binding energy of Au^0 to lower values.[20]

3.7 X-ray absorption spectroscopy

3.7.1 XAS for the evaluation of monometallic NPs

In order to gather more information of Pd and Au atomic environment, XAS measurements were carried out. XAS is a powerful technique, able to obtain electronic structure, oxidation state and coordination environment of NPs.[181, 182]

In Figure 3.12, Pd bulk and Pd_1 XAS spectra are shown. Figure 3.12a, presenting the comparison between Pd_{foil} (bulk) and Pd NPs in IL (Pd_1), was divided in two regions: *i*- XANES, *ii*- EXAFS.

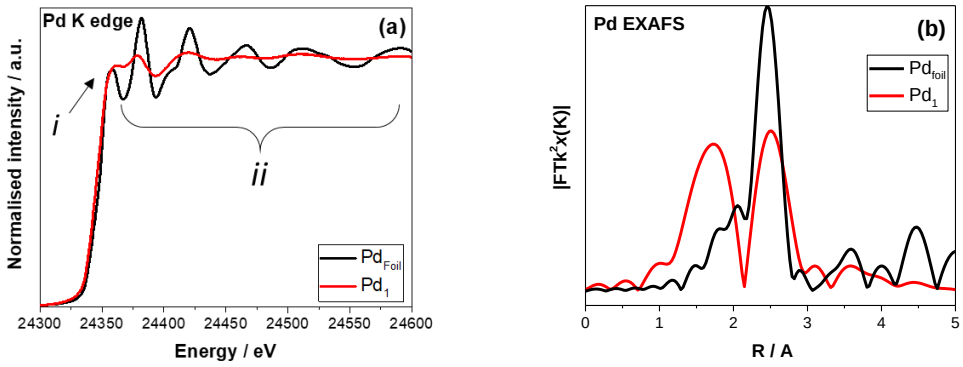

Figure 3.12 - XAS measurements displaying the (a) comparison of the behaviour of Pd_{foil} and Pd NPs in IL (Pd_1) of the Pd K-edge (XANES) and the (b) k3-weighted and Fourier transformed magnitudes of the EXAFS spectra (|FT(k2χ(k))|) of the of Pd_{foil} and Pd NPs in IL (Pd_1).

When comparing the properties of Pd_{foil} to Pd NP in IL (Figure 3.12 a), the dissimilar behaviour of both samples in XANES can be observed. The adsorption edge position tends to shift to slightly higher energy with the increase of particle size, hence the Pd_{foil} presents adsorption edge at higher energy in comparison to (Pd_1). This increase of the adsorption edge is also accompanied by the decrease of the Hw and an intensity increase past the edge. [215] This effect due to the changes in coordination, which will lead to a decrease on the edge. The increase of intensity past the edge is linked to the lattice contraction and to a higher depletion of electrons of the d-orbital (lower coordination number) of the Pd_1 in comparison to Pd_{foil}.[215, 216] Given the presence of IL stabilising the Pd_1 and the lower coordination number of the NPs, less intense H_w than Pd_{foil} were expected. Furthermore, the observation of the EXAFS region of both distinct samples, the amplitudes of the oscillations in both spectra are different. These oscillations on the EXAFS region are size dependent and are lower with the decrease of the particle size. Hence, when comparing both samples, these oscillations are greater for Pd_{foil}, as

expected.[217, 218] In Figure 3.12 b, the EXAFS of Pd_{foil} is compared to the Pd_1. The main peak observed is ascribed to the Pd-Pd bond at 2.5 Å. As the distance increases, other coordinating atoms (in outer shells), at longer bond distances is observed for Pd_{foil}. When compared to Pd_{foil}, which contain only one main peak, in the Pd_1, two main peaks are observed. As in Pd_{foil}, the peak at 2.5 Å that is ascribed to Pd-Pd bond distance, and a second peak at 1.5 Å is associated to Pd-O bond distance (surface coordinated oxygen) due to the interaction of the SO_2 groups in the IL anion with the Pd atoms on the Pd_1. This peak is ascribed in the literature to the interaction Pd-O, nonetheless the Pd interaction with C or N cannot be excluded.[219-222]

3.7.2 XAS evaluation of the bimetallic AuPd NPs

In Figure 3.13, the XANES regions of the AuPd NPs in IL is compared. It is important to mention that Pd concentration in all samples are the same (Table 1).

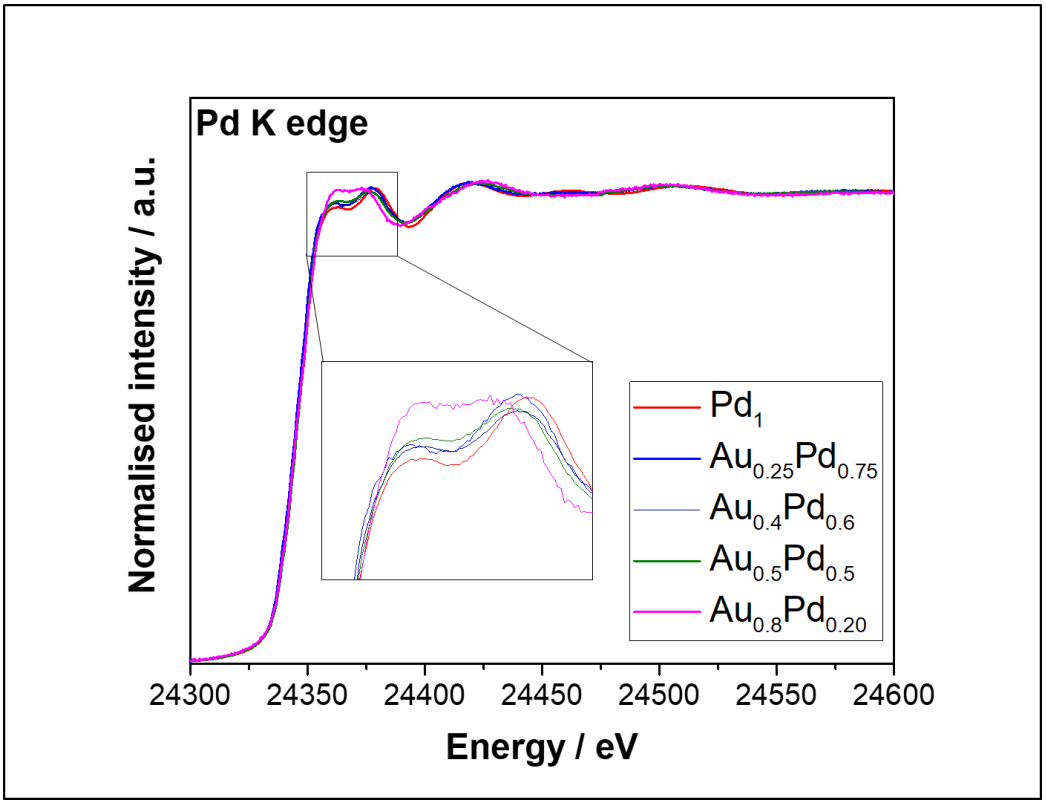

Figure 3.13 - XAS measurements of the produced AuPd bimetallic NPs and Pd_1 deposited in IL displaying the Pd K-edge x-ray absorption near edge structure (XANES).

For Au_xPd_{x-1} the increase of the Au/Pd ratio is accompanied by the increase in the H_w intensity of Pd K-edge in the following order: $Au_{0.80}Pd_{0.20}$ > $Au_{0.50}Pd_{0.50}$ > $Au_{0.40}Pd_{0.60}$ > $Au_{0.25}Pd_{0.75}$ > Pd_1. This increase in electronic depletion with the presence of Au could indicate inter-atomic charge transfer between Pd and Au or the formation of a core-shell structure with the Pd atoms present in the outer shell interacting with the IL.[223] These results are in agreement with the XPS data obtained, reinforcing the formation of AuPd NPs core shell.[20]

The k3-weighted and Fourier transformed extended X-ray absorption fine structure (EXAFS) spectra of all AuPd NPs in IL is compared (Figure 3.14).The data processing details ca be found in experimental procedure.

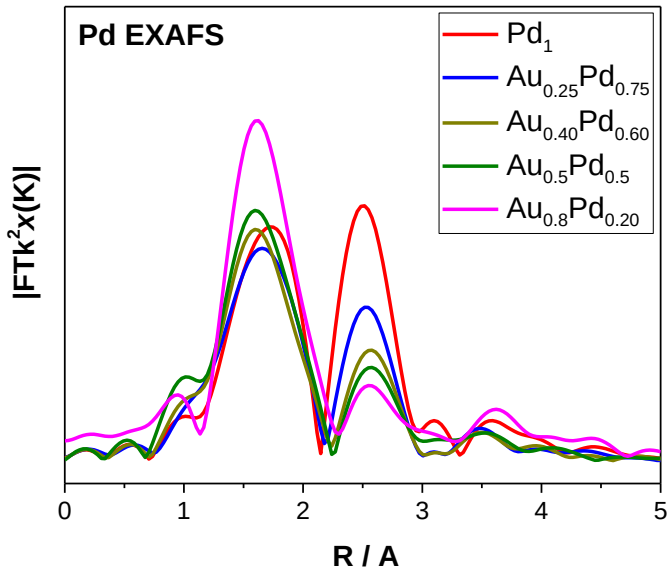

Figure 3.14 - k3-weighted and Fourier transformed magnitudes of the EXAFS spectra (|FT(k2χ(k))|) of the Pd K-edge of the AuPd bimetallic NPs and Pd_1.

The AuPd NPs in IL show a dramatic decrease of the peak intensity associate to Pd-Pd bond (ca. 2.5 Å) when compare to Pd-IL peak (ca. 1.5 Å) intensity (Figure 3.14). Moreover, the increase of Au/Pd ratio led to a shift to longer bond distances, from 2.5 to 2.7 Å, which can be relate to Pd-Au bond distance.[219] To further understand this interaction, the area of each peak was integrated (Figure 3.15 a).

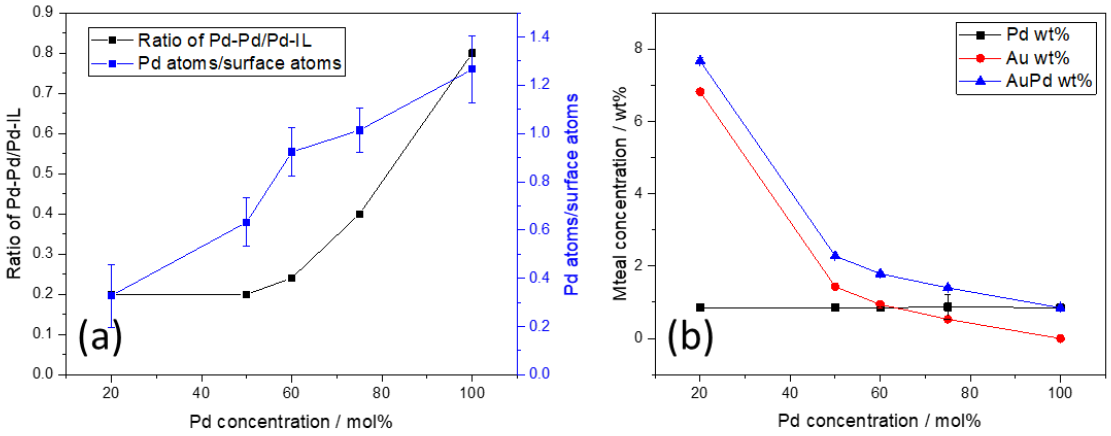

(c) ***Sample***	***Size of NPs (nm)***	***Surface atoms (%)***	***Atoms on the each NP***	***Atoms on surface***	***Pd atoms on NP***	***Au atoms on NP***
Au_1	2.84 (± 1.05)	55 (± 12)	469	258	0	469
$Au_{0.80}Pd_{0.20}$	2.35 (± 0.87)	61 (± 13)	295	180	59	236
$Au_{0.50}Pd_{0.50}$	1.58 (± 0.43)	79 (± 10)	72	57	36	36
$Au_{0.40}Pd_{0.60}$	2.17 (± 0.68)	65 (± 10)	227	148	136	91
$Au_{0.25}Pd_{0.75}$	1.81 (± 0.37)	74 (± 9)	125	93	94	31
Pd_1	1.62 (± 0.57)	79 (± 14)	87	69	87	0

Figure 3.15 – a) Ratio of the Pd-Pd interaction area/Pd-IL interaction peak area and Pd atoms / surface atoms on the NP and b) metal concentration / wt% in function of the Pd concentration (% mol), c) calculation of the surface atoms on the AuPd NPs in IL and the maximum number of Pd atoms in the outer shell of the NP assuming a face-centered cubic (fcc) and the mean size of the NPs.[224] More detail into this calculation is presented in Appendix 5.

Interestingly, this ratio of Pd-Pd/Pd-IL approaches a minimum value of 0.2 with the decrease of the Pd ratio on the samples. This value remains unchanged up to 50 mol % of Pd. These results showcases the Pd-Pd/Pd-IL ratio increasing as the Pd ratio increases, thus suggesting a non-randomised organization of the Pd atoms on the NPs. In Figure 3.15 b, the % Pd content of the AuPd NPs is plotted showing a fixed content of Pd in all AuPd NPs as the % Au content is varying, thus producing the different Au/Pd ratios. Given the fixed content of Pd in the AuPd NPs, in a case of a random distribution of

the Pd and Au atoms on the NPs, the intensity of the 2.5-2.7 Å peak should be maintained in all AuPd NPs. However, the intensity of this peak decreases with the increase of % Au content. Also, given the conservation in intensity of the Pd-IL peak, if all the Pd atoms are populating the surface of the NP, the ratio of Pd atoms on the NP/surface atoms can be calculated assuming the average mean size of of the NPs and plotted in function of % Pd concentration (ratio) in the NP (Figure 3.15 a). This ratio of Pd atoms on the NP/surface reaches a value of 1 over 50 % Pd content indicating the filling of the outer layer with Pd atoms and the increase of Pd content in the inner layers of the NPs. These results agree with the increase of the Pd-Pd/Pd-IL ratio. It is noteworthy to indicate that the Pd-Pd peak (2.5-2.7 Å) also includes the contribution of Pd-Au interaction. Thus, comparing with the ratio of the Pd-Pd/Pd-IL with the ratio of Pd atoms on the NP/surface, both are in agreement, with an increase on the Pd-Pd / Pd-IL interaction ratio with the increase of Pd atoms in the inner layers of the NP.

In Figure 3.16, the structure and interaction of the AuPd NPs with IL is presented, accordingly to the data obtained from the Pd EXAFS in agreement with XPS.

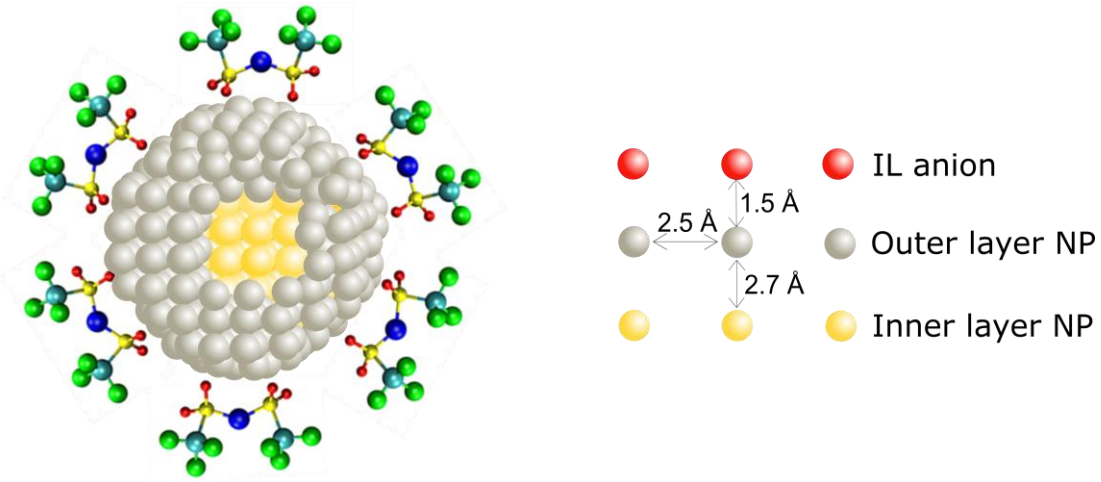

Figure 3.16 – Structure and interaction between the AuPd NP and the IL anion (cation omitted) displaying the relative bond lengths observed by the Pd EXAFS spectra. For simplicity, the geometric structure of the NP is omitted and a cavity in the NP is presented in order to display the inner atomic layers.

In the brief amount of time left in the synchrotron, measuring of Au L-edge was attempted. However, due to the large energy gap between the Au L-edge and the Pd K-edge, during the time allocated, it was not possible to tune the oscillator on the beam line yielding much lower counts and no reliable conclusion could be made.[184, 225, 226]

3.8 Mechanism proposed

The formation of the AuPd NPs in IL is initialised by the co-deposition of both Au and Pd by magnetron sputtering. The obtained materials were investigated and the presence of a core shell structure proposed for the AuPd NPs in IL. However, the formation mechanism that leads to these structures and the growth mechanism of the NP still remains unclear. It could be assumed that the bimetallic structure formation is initialised on the gas-phase with the formation of clusters of Au and Pd by co-deposition. As the gas-phase formed clusters, land on the IL surface and with the continuous income of more dimers and trimers, they increase in size until forming clusters, coalescing and forming

larger bimetallic NPs.[117, 120, 193] As formulated previously, the presence of oxygen groups on the IL anion, can impact on the stabilisation of the NPs, as presented by several other authors[58, 227, 228], leading to the interaction of the IL anion with the incoming Pd atoms and to a subsequent preferential stabilisation of the Pd atoms in an outer shell.

The TEM results showed dissimilar sizes for the NPs formed and their high dependency on the Au content. Therefore, the formation of the core shell NPs can start with the selective stabilisation of the Au and Pd dimers arriving at the surface of the IL. Thus, the initial step of the deposition requires further investigation. To better understand the effects of the co-deposition of the gas-phase formed dimers and trimers, AuPd NPs can be deposited on carbon film of TEM grid instead of depositing into the IL. It is well-know that metal NPs stick in carbon substrates and that electron beam should not cause significant NPs drift. This experiment allowed to investigate the species formed in the gas-phase without significant drift and the interference of the IL. The AuPd NPs deposition parameters were maintained except for the deposition time. A much shorter deposition time (1 sec) was used to avoid the formation of AuPd film on TEM grids. This way, if the bimetallic AuPd clusters are formed in the gas-phase, the concentration of Au and Pd in each NPs must be very similar over the entire carbon film, without segregation of the elements or the formation of monometallic NPs of Au and/or Pd (Figure 3.17).

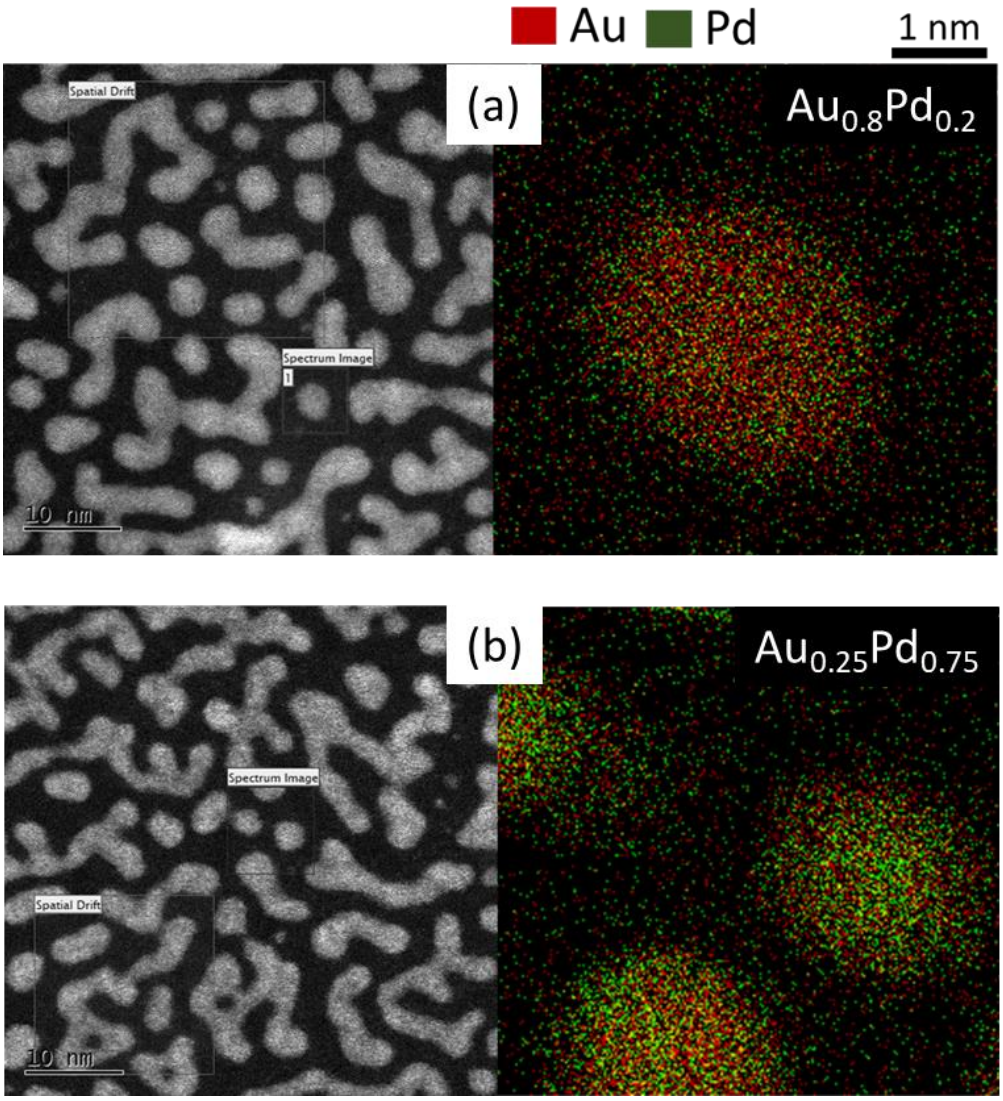

Figure 3.17 – AC-STEM images (left) of the a) $Au_{0.80}Pd_{0.20}$ and b) $Au_{0.25}Pd_{0.75}$ and their respective EDX mapping (right).

The AC-STEM images of NPs obtained by direct sputtering onto a TEM grid shows a homogenous Au and Pd concentration with random atoms distribution in each NP. No segregation of the different elements or significant agglomeration was observed. Therefore, it can be assumed that the bimetallic structure formation is initialised on the gas-phase, forming clusters that, after landing on carbon surface, may coalesce, forming larger bimetallic NPs without the presence of IL. Nonetheless, in this case, the presence of IL,

stabilise preferentially the Pd by the SO_2 groups restricting the formation of a purely alloy structure. The previous reports describing the formation of core shells during the NP formation instead of the reorganisation of an alloyed NP due to the high energy required and the entropy barrier.[120-122] With this experiment, it is demonstrated for the first time, to best of my knowledge, that the formation of a bimetallic cluster occurs in the gas-phase and therefore is independent of the support used.

Hence, the formation of the AuPd NPs in IL starts in the gas-phase with formation of dimers or trimers of both Pd and Au (Figure 3.18, step 1-2). These will land randomly on the IL surface (step 3). As the more dimers and trimers reach the surface of the IL, the size of the formed structures will increase (step 4). In the IL surface formation, the formation of clusters is highly controlled by the IL interaction with the Pd atoms, directing the Au atoms to the interior of the cluster (step 4). The increasing size of the NPs leads to overcoming the surface tension of the IL and permeating into the IL bulk where their stabilisation is controlled by the IL (step 5). The different ratios of Au/Pd affects their size and distribution as elucidated above. Inside the IL, the AuPd NPs are stabilised in a core shell structure with a Pd outer layer and an Au inner layer. This mechanism is in agreement with the characterisation results.[229, 230]

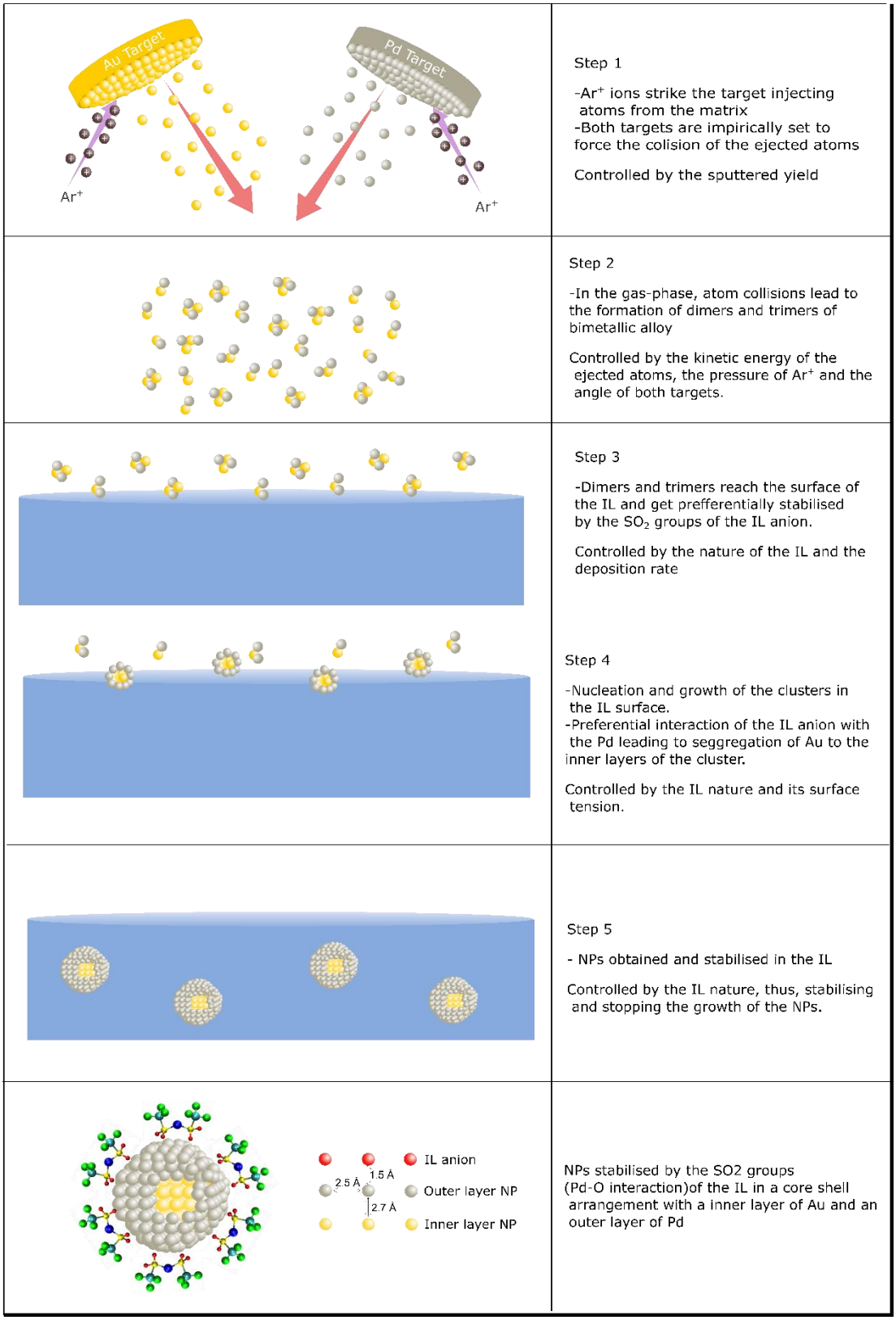

Figure 3.18 - Mechanism for the formation of the AuPd NPs in IL.

3.9 Conclusion

This chapter was outlined as a methodological approach to understand the mechanisms leading to the formation of metallic alloy NPs co-deposited using magnetron sputtering and the interaction of the produced AuPd NPs with the IL support. Both Pd and Au were calibrated for different times using a bespoke magnetron sputtering chamber and co-deposition of both metals was accomplished. The effect of the different ratios of the Au and Pd in the size of the NPs produced was evaluated by electron microscope, presenting a slight increase of the average diameter of 1 nm, with increasing gold content. UV-vis presented the first evidence of both metals interaction, with the disruption of the Au surface plasmon resonance.

Further characterisation showed no alteration on the IL components (XPS), as expected given the low concentration of metal. Nonetheless, when analysing the Au 4f and Pd 3d spectra, the interaction of both monometallic AuPd NPs with the IL anion was identified. The increase of % Pd content resulted in a decrease/disappearance of the Au-IL component, indicating that for higher % Pd content only the Pd was interacting with the IL, thus alluding for core-shell structured in the AuPd NPs.

The XAS measurements of the Pd K edge, presented higher depletion of electrons of the *d*-orbital of the Pd_1 in comparison to Pd bulk. This effect was further evidenced with an increase in the H_w intensity of Pd K-edge with the % Au content. The respective EXAFS spectra enabled to determine the structure and interactions of the Pd adjacent atoms, displaying the segregation of the Pd atoms on the surface and their respective interaction with the IL.

The AuPd NPs in IL were characterised by electron microscopy, UV-Vis, XPS, and XAS and the mechanism of their formation and stabilisation was better understood. The variation of the Pd/Au ratio lead to a significant effect of the oxidation state of the metals, their plasmon resonance and size distribution. The results obtained in this chapter allowed to gain insight on the structure of the AuPd NPs in IL, the mechanisms leading to the formation of these AuPd NPs in IL and their impact on the chemical properties of the materials obtained.

In the next chapters, the catalytic properties of the AuPd NPs will be evaluated, drawing attention to the effect of the Pd/Au ratio in their activity, selectivity and stability towards the selective hydrogenation of CAL.

CHAPTER FOUR

The effect of reaction conditions and metal ratio on the activity and selectivity of the catalysts

4. The effect of reaction conditions and metal ratio on the activity and selectivity of the catalysts

4.1 Initial screening of different catalysts produced

Optimization of any process is essential in modern technology, spreading from research and development to full-scale industrial processes, reducing by-products and co-products and increasing the profitability of the process.[231, 232] Nonetheless, a complete optimisation often requires a systematic search of all logical combinations of reaction conditions in order to determine the most favourable reaction conditions in terms of conversion and selectivity.[231-233]

As in many catalytic reactions, a successful reaction progression depends mainly on the catalyst performance: activity, selectivity and recyclability. These parameters can be considerably influenced by the composition of the reaction, solvent, temperature and pressure used, hence requiring investigation. Granting this approach is time-consuming and expensive, after an initial superficial optimisation and understanding of the effect of a well-defined set of parameters in the reaction outcome, the influence of the ratio of Au/Pd in the AuPd NPs in IL catalysts conversion and selectivity in the hydrogenation of CAL was investigated. The produced AuPd NPs in IL were compared with similar materials reported in the literature. This will enable an accurate evaluation of the AuPd NPs in IL and understanding the effect of the sputtering co-deposition in the catalytic properties of the materials.

4.2 Effect of the solvent

Catalytic activity and selectivity can be substantially influenced by the choice of solvent. Solvents can be classified according to their chemical bonds, acid-base behaviour or substrate–solvent interactions.[233, 234] These can impact catalysts due to high polarity, their hydrogen-bond accepting or donating ability.[235] For instance, in the enantioselective cyclopropanation of styrene, polar solvents can interact with styrene and lead to the formation of an early transition state, far from the chiral environment of the Rh catalyst reducing the selectivity of the catalyst.[233, 234, 236] Solvent effects in catalytic reactions can comprise not only of interactions and solubility of reactants and the catalyst, but also impact solubility of gases in liquid reaction media (hydrogenation), affect diffusion of reactants or even react or interact with the substrates (hydrogen bonds) and products.[233, 234, 237] Furthermore, solvents can bind to the catalysts and compete with the substrate over catalytically active sites (competitive adsorption) or serve as a substrate in a reaction (e.g. methanolysis and ethanolysis).[233]

Given the strong influence of the solvent in the performance of a catalyst, determining how the choice of solvent affects the reaction is crucial. Hence, solvents that are not inert and change the selectivity should be avoided, such as, most protic solvents, this way avoiding side reactions such as dehydrogenation.[235] Highly functionalised solvents that can decompose should also be excluded. In a similar way, low boiling point solvents (e. g. diethylether) should not be used as these will reduce the temperature window for the studied transformation. Some solvents also bind strongly to the catalyst surface thus altering the catalytic activity.

Consequently, tetrahydrofuran (THF) and long-chain alkanes are, due to their chemical inertness and high boiling point, the most suitable choices for testing the reaction. In this study n-hexane was used due to its high dissolution of hydrogen.[238] Methanol was also tested, even though reactive, it usual requires considerably higher temperatures to participate in the reaction.[239] The results obtained for the three different solvents, are presented in Table 2.

Table 2 - The effect of the solvent.

Entry	Catalyst	Solvent	Conversion (%)[b]	TON	Selectivity (%)[c](2:3:4)
1	Au_1	THF	0	-	-
2	Au_1	*n*-Hexane	0	-	-
3	Au_1	Methanol	0	-	-
4	Pd_1	THF	36 ± 4	357	14:74:12
5	Pd_1	*n*-Hexane	54 ± 3	536	10:80:10
6	Pd_1	Methanol	59 ± 7	591	12:72:16
7	$Au_{0.4}Pd_{0.6}$	THF	77 ± 3	770	10:86:4
8	$Au_{0.4}Pd_{0.6}$	*n*-Hexane	>99	>999	2:80:18
9	$Au_{0.4}Pd_{0.6}$	Methanol	>99	>999	8:76:16
10	Blank	THF	0	-	-
11	Blank	*n*-Hexane	0	-	-
12	Blank	Methanol	0	-	-

[a] Reagents and conditions: 0.1 mol % catalyst, 5 bar H_2, solvent (2 mL), 323 K, 0.5 M of CAL. [b] Conversions determined by GC-FID after 24 h and refer to the selective conversion of CAL (average of three runs). [c] 2 = COH, 3 = HCAL, 4 = HCOH.

The catalytic activity of the Au_1, Pd_1 and $Au_{0.4}Pd_{0.6}$ NPs in IL towards the hydrogenation of CAL was evaluated for all three solvents (Table 2). All the AuPd NPs in IL compounds performed differently. The Au_1 (entry 1-3) displayed no activity in any of the assayed solvents. This was expected as Au based catalysts typically require much harsher conditions (348 – 423 K and 25 bar of H_2) to be active.[14] The Pd_1 (entry 4-6) presents mediocre conversion,

whilst with the $Au_{0.4}Pd_{0.6}$ (entry 7-9) achieved high conversions under all tested conditions. Blank tests (entries 10-12) were also performed. These used only IL without the addition of AuPd NPs and presented no catalytic activity. Blank tests without AuPd NP in IL or using neat IL were also performed between reactions to exclude cross-contamination between reactions and ensure good practice. These presented no any activity either.

Given the palladium containing AuPd NPs compounds being catalytic active towards the hydrogenation of CAL, presenting a TON over 300 in all cases, they can be henceforth designated as catalysts. Surprisingly, for both Pd_1 and $Au_{0.4}Pd_{0.6}$ using *n*-hexane (entry 5 and 8), reached high conversions, although the reaction media was not homogenous. Due to the insolubility of the IL in *n*-hexane a biphasic system was formed. After the reaction, the solvent phase presented a dark colouration. ICP analysis of the organic phase and the IL, demonstrated that the AuPd NPs leached into the organic phase. Given these findings, *n*-hexane was not further used as solvent for the system. In methanol the completion of the reaction was reached. Therefore the polarity of the solvent does not seem to play a role in the activity and selectivity of the catalysts as we no difference in between methanol (polar) and hexane (apolar) was observed.

The following studies were undertaken in THF, avoiding the strong absorption of the solvent, as in the case of methanol, whilst maintaining the polarity of the solvent media. The utilisation of THF presented no miscibility constraints as observed with *n*-hexane. Also the utilisation of THF as a solvent produced lower conversions enabling the better study of the kinetics of the reaction and the performance of the different catalysts.

4.3 Effect of the temperature

The reaction temperature can have profound effect onto the reaction outcome. A very typical example includes the hydrogenation of CO_2 to formic acid and CO. Hereby the formation of formic acid is typically achieved at temperature < 373 K, whilst the formation of CO involves elevated temperatures (T > 473 K).[240, 241] In a similar fashion the hydrogenation of CAL could result in various products, which are depicted in Figure 4.1.

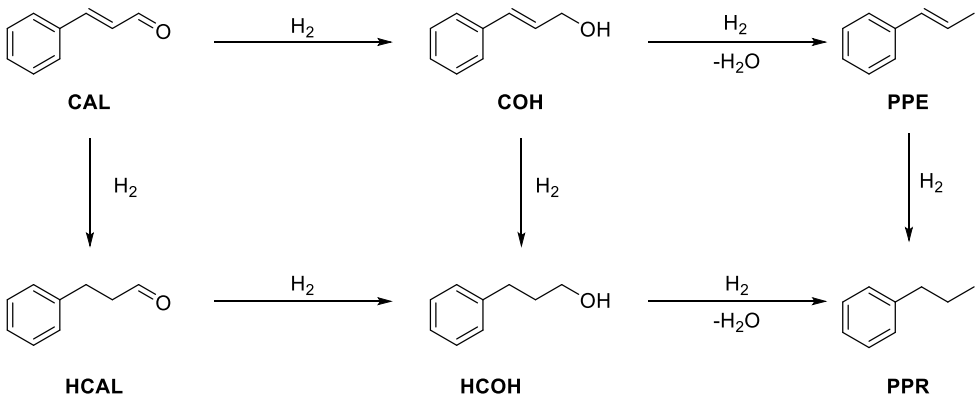

Figure 4.1 - CAL hydrogenation pathways.

Consequently, evaluating the effect of the temperature on a reaction is crucial. Hereby the product distribution in chemoselective hydrogenation is typically dictated either by kinetic control or thermodynamic control. For example, in the selective hydrogenation of CAL, two competing products can be formed: HCAL and COH. Consequently, the product ratio is determined by the rate coefficients (kinetic control) and the thermodynamic stability of the product (thermodynamic control).[242] At higher temperatures, HCAL is favoured (thermodynamic product), whilst COH can only be obtained by kinetic control.[34, 242, 243] The decrease in temperature will lead to a decrease in the reaction rate and conversion according to the Arrhenius equation and the

activation energy of the compounds (kinetic control), thus possibly enabling the formation COH.[34] Hence, the selectivity of the catalytic system could be significantly influenced by the temperature. In Table 3 the results obtained for different temperatures are presented.

Table 3 - The effect of temperature.

Entry	Catalyst	T (K)	Conversion (%)[b]	TON	Selectivity (%) [c](2:3:4)
1	Au_1	R.T.	0	-	-
2	Au_1	323	0	-	-
3	Pd_1	R.T.	18 ± 4	177	28:67:5
4	Pd_1	323	36 ± 4	357	14:74:12
5	$Au_{0.4}Pd_{0.6}$	R.T.	65 ± 3	651	7:83:10
6	$Au_{0.4}Pd_{0.6}$	323	77 ± 7	770	10:86:4

[a] Reagents and conditions: 0.1 mol % catalyst, 5 bar H_2, THF (2 mL), 0.5 M of CAL.[b] Conversions determined by GC-FID after 24 h and refer to the selective conversion of CAL (average of three runs). [c] 2 = COH, 3 = HCAL, 4 = HCOH.

In Table 3, the results for the effect of the temperature are presented. Generally, the increase of temperature from R.T. to 323 K led to an increase in conversion in the reactions tested. For instance, an increased temperature lead to a significant increase in conversion with Pd_1 from 18% conversion to 36% (entries 3 and 4, respectively). Similar tendency is also observed with the $Au_{0.4}Pd_{0.6}$ yielding a moderate increase of 12% (entries 5 and 6, respectively). Surprisingly, no significant change in selectivity is observed when comparing both active catalysts, at 323 K (entries 4 and 6), suggesting that the thermodynamic product is favoured in both cases and the difference in the composition of both catalysts does not affect the thermodynamic control of the reaction. The exception to aforementioned observation is the reaction outcome obtained with Au_1 catalyst. As already observed in Table 3, entry 1 and 2, no

catalytic activity is observed with Au_1. Reiterating, this was expected as Au based catalysts typically require much harsher conditions (348 – 423 K and 25 bar of H_2).[14]

4.4 Effect of the pressure

The pressure of hydrogen and the respective effect on the activity and selectivity of a catalytic process is of utmost importance. Given the H_2 importance as reagent, the pressure of H_2 will directly affect the H_2 solubilized in the liquid phase at a given temperature, according to Henry's law.[244] The increase of a reactant will drive the reaction forwards and towards the lower gas volume. The pressure of hydrogen can affect the gas convection within the liquid phase, which can increase the activity of a reaction at the cost of selectivity, hence the conditions must be improved beforehand.[21] In Table 4 the conversions, activity and selectivity of the tested $Au_{0.4}Pd_{0.6}$ and Pd_1 catalyst are presented.

Table 4 - The effect of pressure.

Entry	Catalyst	Pressure (bar)	Conversion (%)[b]	TON	Selectivity (%) [c](2:3:4)
1	$Au_{0.4}Pd_{0.6}$	1	78 ± 8	780	9:85:6
2	$Au_{0.4}Pd_{0.6}$	5	77 ± 7	770	10:86:4
3	$Au_{0.4}Pd_{0.6}$	7	69 ± 3	690	13:82:5
4	$Au_{0.4}Pd_{0.6}$	10	83 ± 3	904	5:88:7
5	Pd_1	1	23 ± 3	227	11:79:10
6	Pd_1	5	36 ± 4	357	14:74:12
7	Pd_1	7	90 ± 2	904	12:77:11
8	Pd_1	10	90 ± 4	895	10:80:10

[a] Reagents and conditions: 0.1 mol % catalyst, THF (2 mL), 323 K, 0.5 M of CAL. [b] Conversions determined by GC-FID after 24 h and refer to the selective conversion of CAL (average of three runs). [c] 2 = COH, 3 = HCAL, 4 = HCOH.

As shown before, the Au_1 catalyst presents no activity in the previously tested conditions and at higher pressures of H_2 (not presented). The increase of pressure in the tested conditions, for $Au_{0.4}Pd_{0.6}$ (Table 4, entry 1-4) presented no alteration of the conversion and selectivity. In the case of the Pd_1 catalyst (Table 4, entry 5-8) the effect of the increase of pressure is considerable, with an increase from 23% to 90% (entry 5 and 8). The divergent behavior of Pd_1 and $Au_{0.4}Pd_{0.6}$ at differing H_2 pressures suggest that $Au_{0.4}Pd_{0.6}$ are either significantly more active than Pd_1 or that $Au_{0.4}Pd_{0.6}$ could reach completion before the reaction is stopped. Alternatively, Pd_1 could deactivate at lower pressures of H_2 thus increasing the pressure of H_2 and thereby the rate, could lead to a higher conversion before Pd_1 losses activity. Finally the difference between both catalysts could also be explained by different mechanisms of hydrogenation. For instance Pd_1 could hydrogenate CAL by a Langmuir-Hinshelwood type mechanism, whilst $Au_{0.4}Pd_{0.6}$ could hydrogenate CAL by an Eley-Rideal type mechanism. The Eley-Rideal mechanism could allow for a 0^{th} order in respect of H_2 when hydrogen is readily absorbed onto the surface, creating a high concentration of H_{ads} species. The allowing of Pd and Au has been previously reported to increase the d-charge maximum gain when using a composition with 33–50 at% Pd in AuPd NP by differences in the strength of H binding (H_{ads}) in alloy surfaces that can lead to up to 9 times improvement in the reaction rate compared to pure Pd catalysts.[48, 52, 56, 57] Consequently, the reaction was further studied using THF as a solvent, at 323 K and under 5 bar of H_2 to investigate the influence of different ratios of Pd/Au in the conversion and selectivity towards the hydrogenation of CAL.

4.5 Effect of the metal ratio

Different ratios of Pd and Au can enhance the catalytic activity towards the hydrogenation of CAL[48], levulinic acid[54], benzyl alcohol[40], in AuPd catalysts prepared by standard wet chemistry methodology and sol immobilized in diverse supports. Alloying induces a synergistic effect in both hydrogenation and oxidation reactions. The synergetic effect can alter the activity of the catalyst by changes on the d band. Furthermore, this can impact the adsorbate – catalyst interaction leading to changes in activity, selectivity for the reduction of the C=O or C=C double bond or even catalyst poisoning by strongly binding to the substrate or product.

Alloying Pd with Au contributes to the stabilisation of H_2, increasing the stabilisation of H in the NPs structure leading to higher activation rates of the H_2.[48, 52] In this way, given the evidence provided by previous reports and the dissimilar effect of the pressure of H_2 in both Pd_1 and $Au_{0.4}Pd_{0.6}$, the conversion and selectivity dependence of the ratio of Pd/Au was investigated for the AuPd NPs in IL produced by magnetron co-deposition. The results obtained are presented in Table 5.

Table 5 - The effect of the metal ratio.

Entry	Catalyst	Conversion (%)[b]	TON	Selectivity (%) [c](2:3:4)
1	Au_1	0 ± 0	-	-
2	$Au_{0.80}Pd_{0.20}$	61 ± 4	612	7:85:8
3	$Au_{0.50}Pd_{0.50}$	85 ± 1	848	5:90:5
4	$Au_{0.40}Pd_{0.60}$	77 ± 7	770	10:86:4
5	$Au_{0.25}Pd_{0.75}$	75 ± 5	904	4:90:6
6	Pd_1	36 ± 4	364	3:90:7

[a] Reagents and conditions: 0.1 mol % catalyst, 5 bar H_2, THF (2 mL), 323 K, 0.5 M of CAL. [b] Conversions determined by GC-FID after 24 h and refer to the selective conversion of CAL (average of three runs). [c] 2 = COH, 3 = HCAL, 4 = HCOH.

In Table 5, the conversion, TON and selectivity are presented for all the AuPd NPs in IL catalysts. As presented previously, the Au_1 presents no conversion (entry 1) and the Pd_1 presents mediocre conversion values (entry 6). As the ratio of Pd/Au changes, the conversion values peak with the $Au_{0.5}Pd_{0.5}$ catalyst reaching a maximum of 85%. No significant impact on the selectivity is observed indicating a similar activation mechanism of the H_2 (homolytic) between catalysts and similar selectivity towards the vinyl double bond. These results are comparable to sol immobilized AuPd NPs in TiO_2 for the selective hydrogenation of CAL[48] and to dendrimer-encapsulated NPs in the allyl alcohol hydrogenation.[52] Furthermore, low amounts of HCOH were present using the aforemented AuPd NPs in IL without evidence of further hydrogenation contrasting with several similar AuPs NPs catalysts produced by wet-chemistry.[48, 149] The addition of Au to the already active Pd NPs in IL, suggest a synergistic effect in between Pd and Au, leading to an improvement in conversion after 24 hours, nonetheless, only end times were taken. The inactivity of Au_1 and the lower activity observed with $Au_{0.80}Pd_{0.20}$ (Table 5, entry

1 and 2, respectively) under the assayed reaction conditions, suggests Pd to represent the overall more active component in the selective hydrogenation of CAL and the presence of Au is changing the adsorption strength of the substrates / products or the activation of H_2.

In order to better understand the complex catalytic reaction behaviour, such as activity, initial rate, deactivation mechanisms and curves profiles, kinetic studies must be performed. Such methodology enables the construction of graphical rate equations requiring a minimal number of experiments.

4.6 Effect of the metal ratio (kinetic data)

Kinetic studies of complex reaction allows the investigator to understand crucial fragments of the underlying mechanisms, produce reactants concentration dependencies, equilibrium constants and conversion rates for the diverse fragments that constitute a complex reaction. The analysis of such data is complex and, in the majority of cases, the exact quantification is unnecessary, therefore the representation of kinetic data and their overlapping provides a simplified way to compare and provide insight into a catalyst.[245] In Figure 4.2, the conversion profiles of the AuPd NPs in IL catalysts are presented for the hydrogenation of CAL.

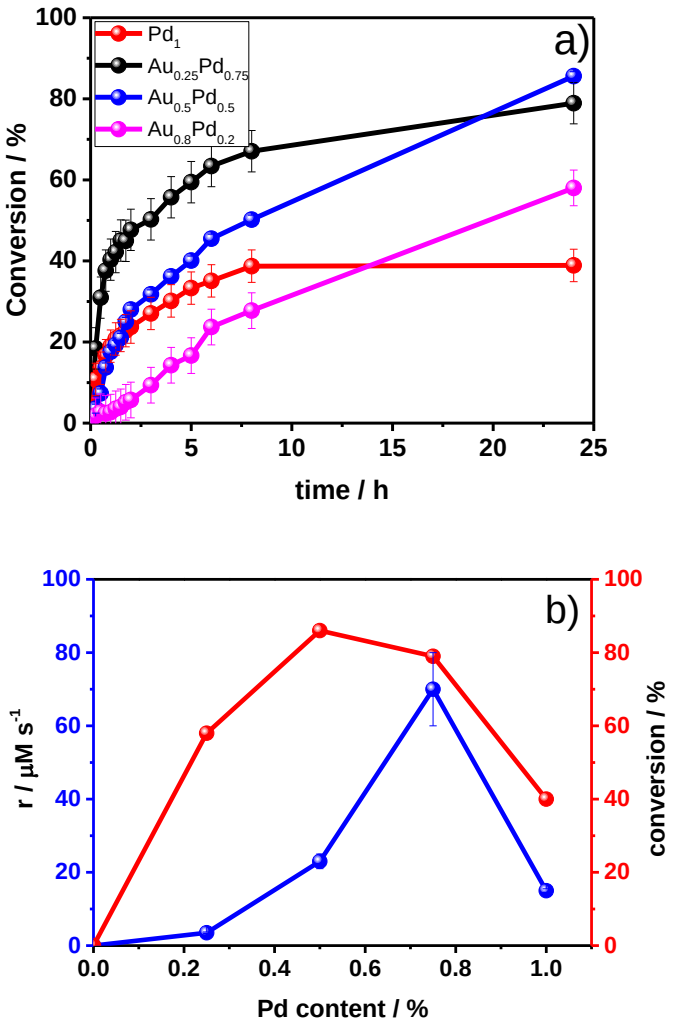

Figure 4.2 – a) Reaction profiles for the AuPd NPs in IL catalysts. At each point of the reaction the selectivity towards HCAL was >90%, thus the selectivity was omitted. b) Comparison in between achieved conversion after 24h and the initial rate. The initial rate was determined by linear regression performed on the consumption of CAL. Reagents and conditions: 0.1 mol % catalyst, under 5 bar H_2, 0.5M of CAL in 10 mL THF at 325 K.

The AuPd NPs in IL were tested in the selective hydrogenation of CAL to HCAL, with the reaction profiles presented in Figure 4.2 a). A more detailed analysis of these profiles reveals that the differences in between the employed catalysts cannot be solely attributed to an enhancement of the rate as previously envisioned.[21, 40, 48, 52, 57] The reaction rates taken from the initial conversion values was determined by linear regression performed on the

consumption of CAL (Figure 4.2 b). All catalysts present dissimilar initial rates with the exception of $Au_{0.5}Pd_{0.5}$ and Pd_1. When comparing these catalysis (Figure 4.2 b), a plateauing of the reaction using Pd_1 is observed at ca. 40% conversion, whereas the $Au_{0.5}Pd_{0.5}$ catalyst remains active and with considerably more activity, reaching over the double of the conversion (ca. 85%) after 24 hours. Such loss of activity is not presented in both the $Au_{0.5}Pd_{0.5}$ and $Au_{0.80}Pd_{0.20}$ catalysts, without evidence of the reaction reaching a plateau stage. Additionally, the $Pd_{0.75}Au_{0.25}$ high reaction rate (Figure 4.2 b) for the transformation of CAL to HCAL is observed, reaching 70% conversion after only 8h of reaction. This rapid reaction rate by the $Pd_{0.75}Au_{0.25}$ makes a precise analysis of the reaction profile rather challenging, i.e. it cannot be deduced whether the reaction is reaching a plateau or full conversion is observed under prolonged reaction times.

In order to deduce a more accurate description for the catalytic behaviour in between Pd NPs and AuPd NPs, further kinetic analysis is required. These analyses will be described in the following chapter.

4.7 Conclusions

This chapter outlined the first steps to evaluate the AuPd NPs in IL catalytic properties. Both the activity and selectivity of the catalysts were investigated, as well as the effects of the solvent, temperature and pressure on their catalytic performance. The $Au_{0.4}Pd_{0.6}$ catalyst presented enhanced catalytic performance in comparison to the Pd_1 catalysts, with the solvent not altering the selectivity of the catalysts. Under the assayed conditions all catalysts seem to favour the thermodynamic product (HCAL), as different temperatures were

tested. The $Au_{0.4}Pd_{0.6}$ presented no dependency on the applied H_2 pressure on the system, nonetheless the same could not be observed for the Pd_1 catalyst. This catalyst displayed a considerable increase in conversion after 24h with the increase in pressure, thus presenting a dependency. The impact of different ratio in Au/Pd in the hydrogenation of CAL was also evaluated, presenting an enhancement of the catalytic activity of the alloyed catalysts. As the ratio of Pd/Au changes, the conversion values reach a maximum with the $Au_{0.5}Pd_{0.5}$ catalyst (85 %). A similar enhancement is observed in the presence of Au, as previously cited by other authors. Nonetheless, most of the publications only report final conversion values and never the reaction profiles. A more detailed analysis of these profiles reveals that the differences in between the employed catalysts cannot be solely attributed to an enhancement of the rate as previously envisioned. The loss of activity for the Pd_1 catalyst, the different kinetic profiles between all tested catalysts and the effect of the pressure on the Pd_1 catalyst indicate a complex process affecting the catalyst performance.

In the next chapter, the dependencies, the effect of substrates and products in the activity of the catalysts and the deactivation mechanisms will be evaluated using Variable Time Normalization Analysis (VTNA).

CHAPTER FIVE

Effect of the different ratios of Pd and Au on rate order and catalyst deactivation

5. Effect of the different ratios of Pd and Au on rate order and catalyst deactivation

5.1 Introduction

The alloying of Pd and Au leads to drastic effects on the catalytic performance in the hydrogenation of CAL. The presence of Au increases the total conversion after 24 hours, however, kinetic data shows similar initial rates for both $Au_{0.5}Pd_{0.5}$ and Pd_1. Under the reaction course, the loss of activity for the Pd_1 catalyst, the different kinetic profile in comparison to $Au_{0.5}Pd_{0.5}$ and the drastic effect of the H_2 pressure in the catalytic properties indicate a complex process demonstrating the synergy of both metals. The presence of Au in the already active Pd catalyst has been shown to enhance mechanistic aspects with Pd catalysts such as increased H_2 activation. Luo *et al.*, report the dissimilar effect of alloying AuPd in comparison to AuPt. In the AuPd NPs, the presence of Au changes the adsorption strength of the substrates / products or the mechanistic activation of H_2. Hence it is reasonable to assume that the difference in kinetic traces are associated with mechanistic differences in between Pd_1 and $Au_{0.5}Pd_{0.5}$, being influenced by mechanistic differences in between these catalysts. Furthermore, the early plateau reached by Pd_1 at 36% conversion could indicate the catalyst agglomeration, leaching and product/reagent poisoning.[246] Usually, catalyst deactivation occurs over time with the loss of catalytic activity, which is a fundamental problem and continuing concern for industrial catalytic processes. Understanding deactivation and catalyst poisoning patterns will enable the life time prediction of a given catalyst and its expected performance, maintaining high throughputs in industrial processes.[246, 247]

In this chapter, the Pd_1 and $Au_{0.5}Pd_{0.5}$ will be further investigated towards the apparent rate orders, poisoning effect of both substrate / product and deactivation patterns in order to capture the mechanistic aspects of both catalysts and determine the effect of the addition of Au.

5.2 Describing the mechanisms for the selective hydrogenation of CAL

5.2.1 Possible mechanisms

Most reactions demand a catalyst to occur, with some reactions happening on a surface and requiring the adsorption of at least one of the reactants.[155, 156] For these heterogeneous bimolecular reactions, two most commonly accepted mechanisms are: the Eley–Rideal and the Langmuir–Hinshelwood mechanisms.[157] In the case of the Eley–Rideal, one of the reactants is required to be chemisorbed on the surface of the catalyst, whilst the other reacts from the gas phase *via* collision with the chemisorbed reactant, whereas, on the Langmuir–Hinshelwood mechanism, both reacting species are required to be chemisorbed on the catalyst surface for the reaction to take place.[157] In both cases, the species are expected to desorb hastily from the catalyst surface, allowing the catalyst to catalyse another reaction. Most reactions are accepted to occur through the Langmuir–Hinshelwood mechanism, with currently no agreeable explanation for this vital preference, taking into consideration the higher energy barriers of the Langmuir–Hinshelwood mechanism in comparison to Eley–Rideal.[248] In Figure 5.1, both mechanisms are exemplified for the hydrogenation of CAL.

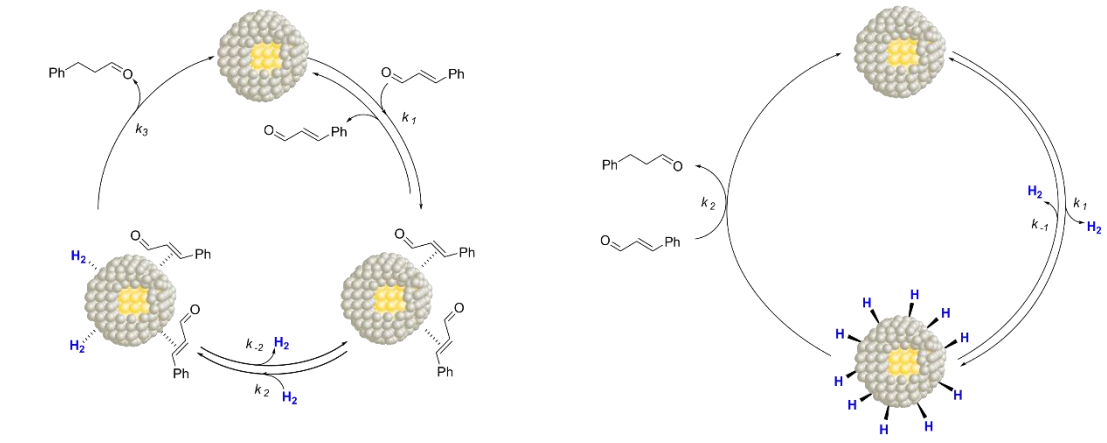

Langmuir-Hinshelwood type mechanism **Eley-Rideal type mechanism**

Figure 5.1 – Langmuir-Hinshelwood (left) and Eley-Rideal (right) mechanisms adapted for the selective hydrogenation of CAL.

The most accepted mechanism for the selective hydrogenation of CAL is through Langmuir-Hinshelwood type mechanism (Figure 5.1 left).[33, 34] This way, the first step will consist in the reversible absorption of H_2 and CAL onto the surface. The molecular H_2 will be activated by homolytic activation, hence obtaining $2H^{\cdot}$ stabilised by the AuPd NPs in IL structure. The initial absorption and activation of H_2 is followed by the irreversible hydrogen transfer onto the substrate, reducing the CAL vinyl bond. Finally, the product (HCAL) is desorbed from the catalyst surface. The free catalyst is able to continue into another catalytic cycle. It is important to note that while, both the hydrogen activation and transfer is presented as a single step, this is commonly accepted, and that both occur in a multiple step mechanism with different adsorption patterns for α,β-unsaturated aldehydes depending on the nature of the catalyst (single atoms, single metal NPs, bimetallic NPs) and the support used.[34] The hypothesised mechanism for the H transfer was presented previously on chapter 1.

Therefore, the two main mechanisms can be present: the Eley-Rideal and the Langmuir-Hinshelwood. In the first case, the rate determining step (RDS) is between the adsorbed H· and the CAL molecule in solution to form HCAL. In the second case, the reaction between the adsorbed CAL and the activated H· is the RDS.

5.3 Different concentrations of CAL and H2

This way, in order to determine the mechanism present, the influence of [CAL] and [H_2] in the reaction rate should be investigated and the rate laws for the selective hydrogenation of CAL developed. Figure 5.2 presents the influence of the CAL and H_2 concentration in the reaction media for the $Au_{0.5}Pd_{0.5}$ and Pd_1 catalysts performance.

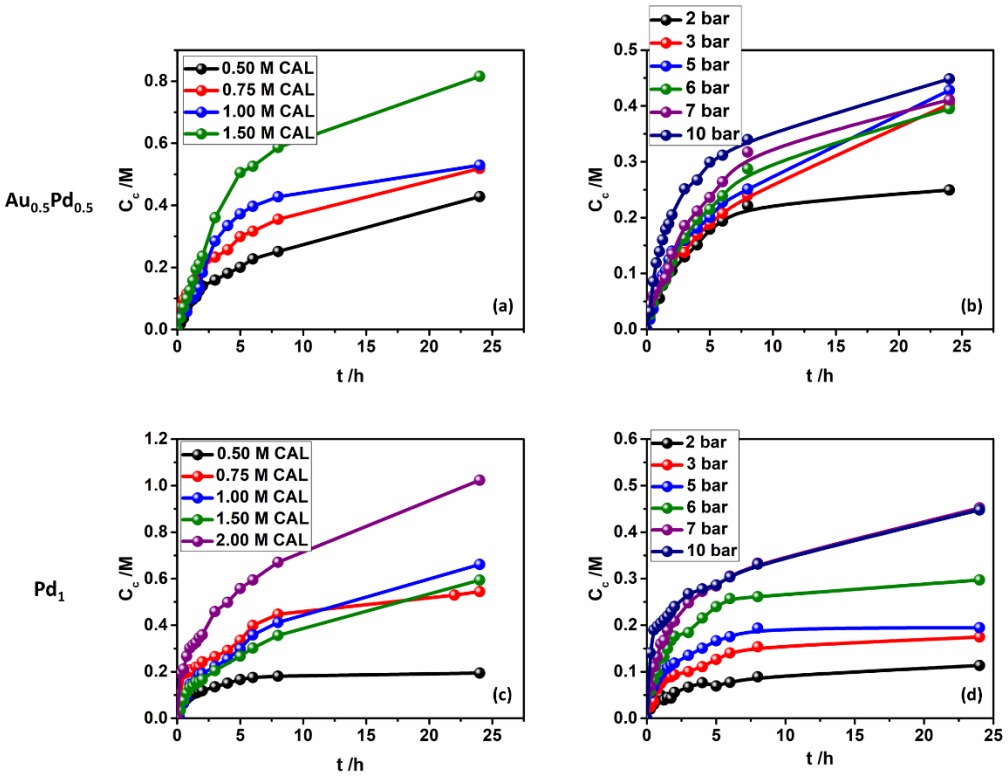

Figure 5.2 - (a) to (b) kinetic analysis undertaken with $Au_{0.5}Pd_{0.5}$ (a and b) and Pd_1 (c and d) catalysts with (a) and (c) depicting the effect of the [CAL] on the catalysts performance whereas (b) and (d) depict the effect of the [H_2]. All the parameters where maintained while the effect of [H_2] and [CAL] is essayed:

0.1 mol % catalyst, under 5 bar H_2 in the presence of 0.5M CAL in 10 mL THF at 323 K. All kinetic traces depicted here are displayed as the consumed concentration of CAL which can be converted into concentration of HCAL, see chapter 2 for further information (Note also under the essayed reaction conditions selectivity > 95; values obtained with a maximum of ± 3% error).

As presented in Figure 5.2 a, in the case of the $Au_{0.5}Pd_{0.5}$ catalyst, the increase of [CAL] leads to enhanced reaction rates. This effect is also observable in Figure 5.2 b, the increase of [H_2] leads to an increase of the reaction rate, showing the rate dependency on the H_2 pressure. Nonetheless, after 24 hours, the conversion values are similar, with the exception of the 2 bar experiment, show a reduced dependency of the [H_2]. In both cases, the increase of the substrate concentration (CAL and H_2), leads to clear increase of reaction rates, obtainable from the derivative of the initial points. This effect is observable over entirety of the essayed time, thus leading to higher conversions after 24 hours.

In comparison, when using the Pd_1 catalyst, the increase of [CAL] (Figure 5.2 c), yields an abrupt increase with the increase from standard conditions to 0.75 M, 1.00 M and 1.50 M leading to a rather large positive effect on the production of HCAL. Nonetheless, when comparing between the [CAL] of 0.75 M, 1.00 M and 1.50 M, no increase can be observed with similar kinetic traces being obtained. This could indicate a substrate poisoning effect hindering the catalytic activity. A further increase of [CAL] above 1.5 M yields a remarkable increase in the reaction rate. In Figure 5.2 d (Pd_1 catalyst), when the pressure of H_2 is increased with this effect is present in the pressure range of 2 bar to 7 bar. A further increase to 10 bar producing no effect, indicating a saturation of the adsorption site for H_2 or the limitation effect from another reactant.

Hence, from the observation of Figure 5.2 a-d, the rate dependency of both catalysts towards [CAL] and [H_2] is apparent, leading to the conclusion that both catalysts hydrogenate CAL through a langmuir-hinshelwood mechanism. Furthermore, the effect of the [CAL] and [H_2] in these results suggest a third competing effect taking place in the Pd_1 case.

In order to evaluate the effects of the [CAL] and [H_2] in the reaction, and thus comparatively quantify rate orders for both reagents, variable time normalized analyses (VTNA) according to methods proposed by Bures and co-workers was applied.[152, 153] This methodology enables the normalisation of the time component towards the investigated component, allowing a visual overlay of the kinetic traces when using different concentrations. This will produce an overlay of the kinetic traces normalised if the substrate is raised to the correct order thus removing the investigated reagent from the kinetic trace, if no substantial degradation of the given component is present.[152-154] In Figure 5.3, the VTNA is presented for the effect of [CAL] and [H_2] on the $Au_{0.5}Pd_{0.5}$ catalyst performance.

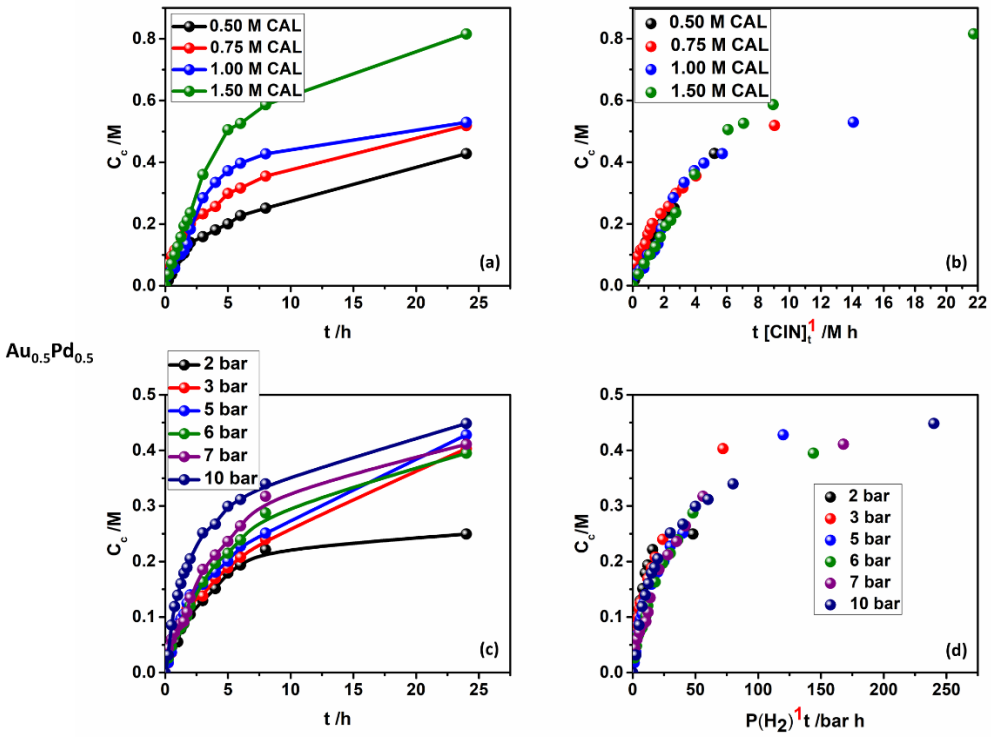

Figure 5.3 - (a) and (c) depict kinetic analysis undertaken with $Au_{0.5}Pd_{0.5}$ catalyst depicting the effect of the [H_2] and [CAL] on the catalyst performance, respectively. (b and d) present the time normalised analysis of kinetic traces obtained in (a and c, respectively). All the parameters where maintained while the effect of [H_2] and [CAL] is essayed: 0.1 mol % catalyst, under 5 bar H_2 in the presence of 0.5M CAL in 10 mL THF at 323 K. All kinetic traces depicted here are displayed as the consumed concentration of CAL which can be converted into concentration of HCAL, see chapter 2 for further information (Note also under the essayed reaction conditions selectivity > 95%; values obtained with a maximum of ± 3% error).

By visually overlaying for the kinetic traces for the effect of the [H_2] and [CAL] in the performance of the $Au_{0.5}Pd_{0.5}$ catalyst (Figure 5.3 b and d) can be found that the investigated reagents can be normalised to the order of 1. These findings suggest the rate dependency for both substrates and their occurrence on the catalyst surface. A thorough mechanistic investigation would probably disclose a more complex mechanism for the activation of H_2 and the hydrogen transfer to the vinyl groups of CAL on the surface of the $Au_{0.5}Pd_{0.5}$ catalyst.[33, 34, 53] Furthermore, these results suggest that neither significant substrate poisoning nor competitive absorption properties are dominating the performance of the $Au_{0.5}Pd_{0.5}$ catalyst. In Figure 5.4, the VTNA is presented for the effect of [CAL] and [H_2] on the Pd_1 catalyst performance.

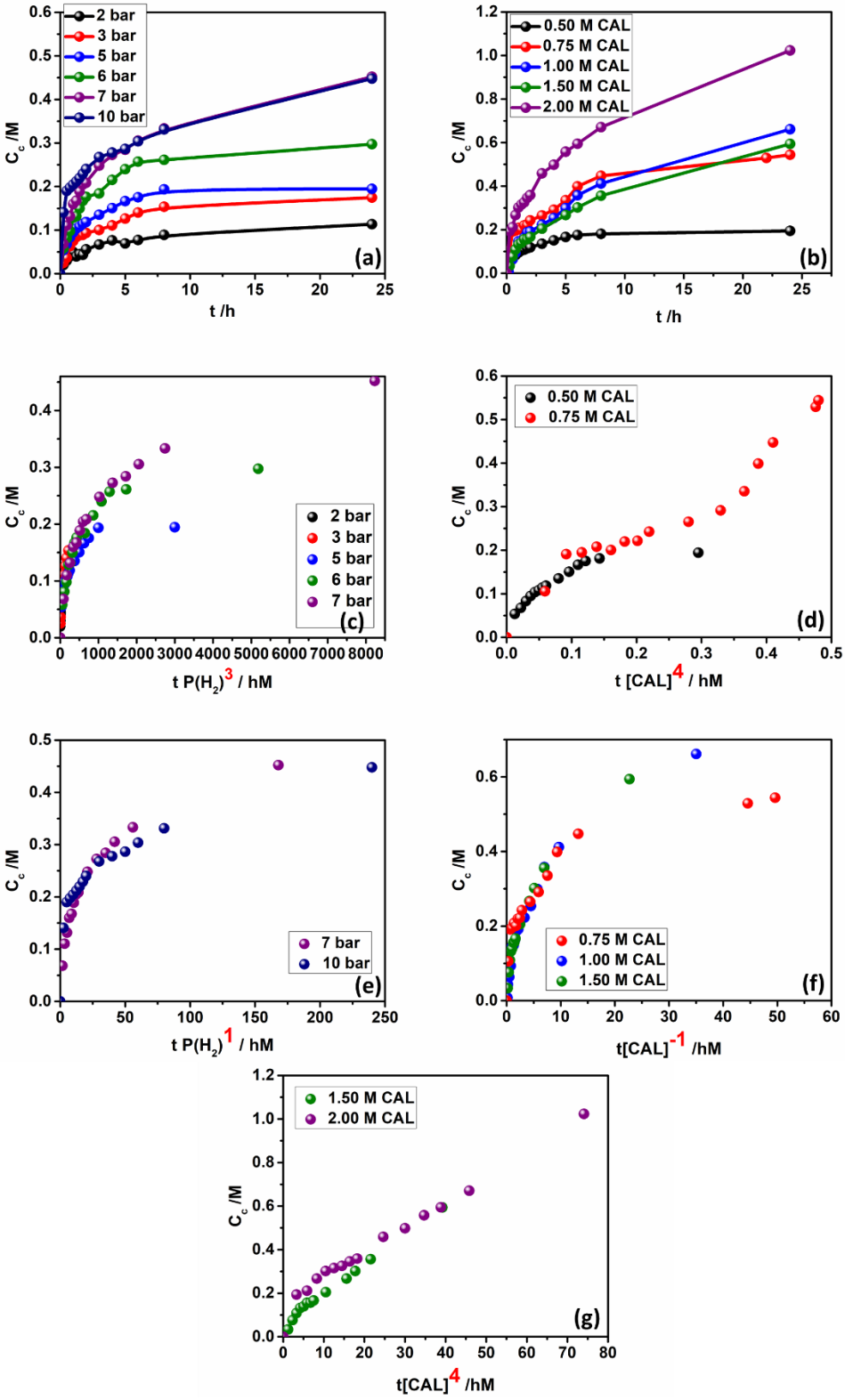

Figure 5.4 - (a) and (b) depict kinetic analysis undertaken with Pd_1 catalyst depicting the effect of the [H_2] and [CAL] on the catalyst performance, respectively. (c and e) present the time normalised analysis of kinetic traces for the effect of [H_2] presented in a. (d, f and g) present the time normalised analysis of kinetic traces for the effect of [CAL] presented in b. All the parameters where maintained while the effect of [H_2] and [CAL] is essayed: 0.1 mol % catalyst, under 5 bar H_2 in the presence of 0.5M CAL in 10 mL

THF at 323 K. All kinetic traces depicted here are displayed as the consumed concentration of CAL, which can be converted into concentration of HCAL, see chapter 2 for further information (Note also under the essayed reaction conditions selectivity > 95%; values obtained with a maximum of ± 3% error).

In Figure 5.4 c to f show that unlike in the case of the $Au_{0.5}Pd_{0.5}$ catalyst, for Pd_1, an acceptable visual overlay of all the kinetic traces cannot be found for the catalyst performance in all assayed reaction conditions. For instance, in the case of the [CAL], 3 differing responses are displayed for the investigated concentration range. At the concentration range of 0.5 M to 0.75 M (Figure 5.4 d) the observed rate effect is affected by two additive factors, i.e. catalyst stability (which is likely increased at higher concentrations of CAL) and the overall beneficial effect of increased concentrations of reagents on the surface. Here an order for CAL ca. 4 is presented. Over 0.75 M, in the range of 0.75 M to 1.5 M the competitive absorption of CAL with H_2 for the active sites appear to dominate the overall reaction rate given an order of ca. -1 was determined. The increase of [CAL] over 1.5 M, the stabilisation effect of the CAL is outweighing all other effects, including substrate inhibition with a CAL producing a rate order of ca. 4. The negative order found in the concentration range of 0.75 M to 1.5 M suggests a Langmuir Hinshelwood type mechanisms, whilst the order >1 suggest that the catalyst concentration is changing over the course of the reaction.

In a similar way, in the case of the effect of the [H_2] in the catalyst performance, 2 differing responses are displayed for the investigated concentration range. An approximate order of 3 for the H_2 pressure range from 2 bar to 7 bar, is presented (Figure 5.4 c). It is important to mention that an order >1, could also suggest that more than one substrate molecule is binding to one surface site,

in this case, 3 H_2 molecules are binding to one surface atom. Increasing the pressure above 7 bar would consequently reduce the H_2 molecules bound in a single step to 1. This would indicate that all bound substrate molecules bounding to the active site must be participating in the same molecular reaction, giving rise to a highly complex transition state in the rate determining step for the reaction. Otherwise, diffusional effects can also influence the rate order for H_2, nonetheless, these would also be present in the case of the $Au_{0.5}Pd_{0.5}$ catalyst. This cannot be supported with experimental results, since a consistent order of 1 for H_2 is present with the $Au_{0.5}Pd_{0.5}$ catalyst. Given the evidence presented by the investigated effect of the [CAL] and [H_2] on the catalysts, other factors are clearly overshadowing the reaction rate in the Pd_1 catalyst with catalyst deactivation and product poisoning as the most plausible effects dominating poor performance of the catalyst.

5.4 Effect of HCAL

One of the most notorious ways for catalyst deactivation is through the chemisorption of reactants, products or impurities in the reaction media onto catalytic sites permanently (poisoning). The strength of the chemisorption dictates the reversibility of the poisoning.[249, 250] This way, the poison will compete with the substrate for the catalytic sites, physically blocking of adsorption sites and inducing changes in the catalyst geometric and electronic surface. This is highly dependent on the metal and the poisonous compound with some compounds being both reactants and poison depending on the metal used to catalyse the reaction.[251, 252] In addition, the strong adsorption of a compound in a catalyst surface can electrically modify not only the atoms involved, but also the neighbouring atoms and their ability to catalyse the

reaction by modifying their adsorption, desorption and diffusion strengths towards reactants and products, such as, H_2.[253] The poison compound can also drastically modify the surface or block the access to catalytic active sites by the reactants.

In order to distinguish in between a catalyst deactivation or a conceivable product inhibition, the effect of the HCAL onto the reaction rate requires investigation. As observed previously, HCAL is the main product (± 95%), and in the case of product inhibition, a decreasing rate, and hence a negative rate order, should be observable given the product competition with the substrate for the catalyst active site. This competing effect would lead to a reduction of the catalytic active sites, hence, a reduction of the reaction rate. In Figure 5.5 the effects for the addition of HCAL to the reactions in t_0 (initial reaction time) to the kinetic traces for the hydrogenation of CAL is presented.

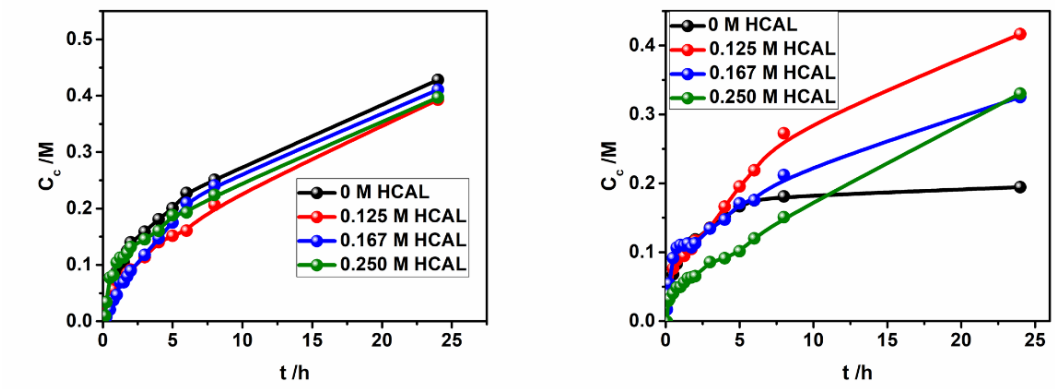

Figure 5.5 - Overlaid comparison of the kinetic profiles for both Pd_1 (right) and $Au_{0.5}Pd_{0.5}$ (left) when HCAL is added at t_0. Reagents and conditions: 0.1 mol % catalyst, under 5 bar H_2 in the presence of 0.5 M CAL in 10 mL THF at 323 K. HCAL amount added is displayed in the graphs. The concentration displayed represented the [HCAL] formed calculated from the [CAL] consumed. See chapter 2 for further information (Note also under the essayed reaction conditions selectivity > 95%; values obtained with a maximum of ± 3% error).

In Figure 5.5, the formation rate of HCAL for the hydrogenation of CAL presented with increasingly amount of HCAL added at t_0 leads to different effects depending on the catalyst used. In neither of the cases a complete overlay is possible suggesting an underlying deactivation mechanism is dominating the reaction outcome. In the case of the $Au_{0.5}Pd_{0.5}$ catalyst, a VTNA analysis would present a zero order for the addition of HCAL given the close kinetic traces values. Nonetheless, in the case of the Pd_1 catalyst, a positive effect and a negative effect can be observed (Figure 5.6).

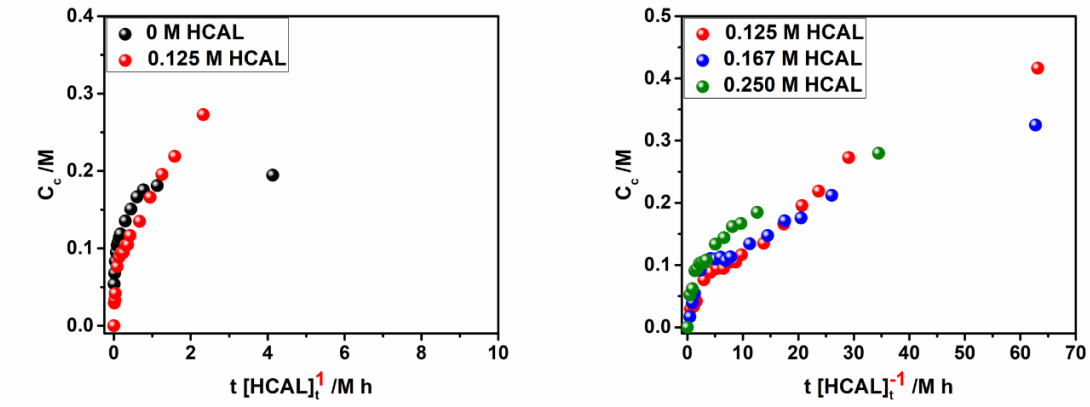

Figure 5.6 - Time normalised analysis of kinetic traces for the effect of the addition of HCAL to the reaction mixture at t_0. Comparison between the standard conditions and with [HCAL]=0.125 M (a) and comparison between the [HCAL]=0.125 M; [HCAL]=0.167 M; [HCAL]=0.250 M (b) Reagents and conditions: 0.1 mol % catalyst, under 5 bar H_2 in the presence of 0.5M CAL in 10 mL THF at 323 K. HCAL amount added is displayed in the graphs. The concentration displayed represented the [HCAL] formed calculated from the [CAL] consumed. See chapter 2 for further information (Note also under the essayed reaction conditions selectivity > 95%; values obtained with a maximum of ± 3% error).

The addition of small amounts of HCAL significantly increase the conversion of CAL whilst using Pd_1 (Figure 5.6, left) with an order of HCAL equal to 1. However, the further increase of HCAL at t_0 leads to a decrease in activity, as presented in Figure 5.6 (right) with the respective negative order of 1. Hence, it can be concluded, that the addition of HCAL presents a mixed influence on

the catalyst activity, with a low [HCAL] at t_0 being beneficial towards the catalytic activity, nonetheless, at concentration > 0.13 M negative effects due to product inhibition are more pronounced, thus leading to decreased rates when using Pd_1. Furthermore, in the case of the Pd_1 catalyst, the initial rate of the reaction is apparently not influenced by the addition of HCAL at t_0, up to a concentration of 0.25 M HCAL. In the case of $Au_{0.5}Pd_{0.5}$, the addition of HCAL to the reaction initial time, presents no significant effect onto the rate in the concentration range of 0.13 M to 0.5 M (Figure 5.6, left). These findings indicate that the rate of reaction is mostly governed by CAL and H_2 and that it can be attributed to both the nullification of detrimental effects rising by product inhibition and positive effects by catalyst stabilisation. Hence, the influence of HCAL onto the hydrogentation of CAL might be best described by the equation 6:

$$\frac{d[HCAL]}{dt} = \frac{ae^{-\frac{bt}{1+[HCAL]}}}{(1+c+[HCAL])^2}$$ *Equation6 –Derivative of the concentration of HCAL over time.*

Whereby a, b and c are constants representing k constants and concentration of reactants such as CAL and H_2. The denominator presents the form of a Langmuir Hinshelwood mechanism using the c to represent "k_1[CAL]+k_2[H_2]" Given the mixed influence of HCAL into the reaction rate, the deactivation of the catalyst can be expressed in terms of an exponential in the numerator.

Using an VTNA, kinetic traces for reactions with different concentration can be compared at similar conditions.[152, 245] This methodology compares concentration curves for the given compound formation or consumption using

reactions with different time points. Simply put, if the reactions with initial addition of HCAL are shifted in time to match the concentration HCAL to the experimental conditions for the experiments starting without initial concentrations of HCAL but with higher concentration of CAL, an overlay of the kinetic traces should be possible. In this case, both experiments will possess the same initial concentration of reactants and catalyst, but different concentrations of the target product or poison. The only difference will be the number of cycles done by the catalyst (turnovers), the concentration of HCAL (in this case) and the time of reaction. If the VTNA reaction profiles do not overlay, it would indicate product inhibition or a significant catalyst deactivation process. The results obtained for both catalysts is presented in Figure 5.7.

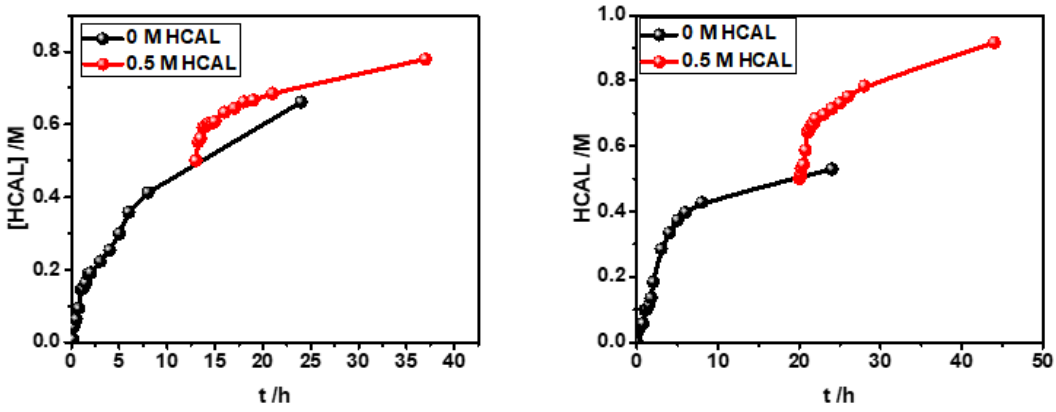

Figure 5.7 - Overlay experiments undertaken with $Au_{0.5}Pd_{0.5}$ (left) and Pd_1 (right). Hereby, reactions undertaken with initial addition of HCAL (red) are shifted by the time t, to the time t using VTNA, where the reaction condition match the experimental conditions matching the concentrations present with experiments starting without initial concentrations of HCAL but with higher concentration of CAL (black). Reagents and conditions: 0.1 mol % catalyst, under 5 bar H_2 in the presence of 0.5M CAL in 10 mL THF at 323 K. HCAL amount added is displayed in the graphs. The concentration displayed represented the [HCAL] formed calculated from the [CAL] consumed. See chapter 2 for further information (Note also under the essayed reaction conditions selectivity > 95%; values obtained with a maximum of ± 3% error).

By the VTNA analysis, neither the kinetic traces for $Au_{0.5}Pd_{0.5}$ nor Pd_1 are able to overlay for the bespoke reactions. This indicates that further underlining

catalyst deactivation is dominating the reaction outcome. It is important to note that a lacking of overlay for these reactions is not indicative of an absence of product inhibition but rather is evidence for catalyst deactivation. Furthermore, the HCAL as a sole catalyst poison can be excluded. If the sole side effect would be the poisoning of the catalyst by HCAL (that is product inhibition), so an overlay of reaction curves would produce an overlay.

5.5 Conclusions

This chapter takes a deeper look at the catalysts produced, focusing on the $Au_{0.5}Pd_{0.5}$ and Pd_1 catalysts. This decision was instigated by the discrepancy observed in the kinetic traces of both catalysts and the absence of substantial studies of the catalytic performance / stability of AuPd NPs. Therefore, mechanistic studies evaluating the effect of the [CAL] and [H_2] on the catalysts kinetic traces were performed presenting the dependency on both substrates and concluding that their mechanism follows a Langmuir-Hinshelwood mechanism. Due to their dependency on both substrates being adsorbed on the catalyst surface for the reaction to proceed, a typical of a Langmuir-Hinshelwood mechanism is expected. Nonetheless, the effect of both CAL and H_2 was evaluated using VTNA and found considerable differences in their effect in both catalysts and their dependencies. The Pd_1 catalyst rate and conversion can be significantly enhanced by increasing the concentration of the substrates.

The effect of the HCAL (poisoning effect) on the catalytic activity was also studied, determining that an underlining catalyst deactivation is dominating the reaction outcome. This result did not exclude the presence or absence of product poisoning, however it uncovers a predominant catalyst deactivation

effect that is controlling the outcome of the catalytic activity. This effect can be further substantiated by the increase of substrate concentration, leading to longer catalyst life and hindering their deactivation with the adsorption of the substrates.

Most importantly, it demonstrates for the first time that the addition of Au to Pd catalysts by co-deposition besides increasing the stabilisation and activation of H_2, can additionally lead to increase stabilisation of the catalyst preventing their deactivation. Unfortunately, due to the Covid-19 pandemic, the deactivation studies were halted before their conclusion. Nonetheless the stability of the catalysts was being evaluated by delaying the addition of H_2 to the reaction media containing catalyst and solvent and evaluating the effect on the catalytic properties of the catalyst. Separated experiments were also being performed with CAL added to the initial mixture to evaluate the substrate adsorption effect on the catalyst deactivation.

CHAPTER SIX

Overall Conclusions and Future Work

5. Overall conclusions and future work

5.1 Overall conclusions

In this work, mono– and bimetallic AuPd NPs (Au_1; $Au_{0.75}Pd_{0.25}$; $Au_{0.50}Pd_{0.50}$; $Au_{0.40}Pd_{0.60}$; $Au_{0.25}Pd_{0.75}$; Pd_1) were produced by magnetron sputtering. The magnetron sputtering deposition system presented high reproducibility for the deposition of both for Au and Pd in deposition and co-deposition mode. The AuPd NPs in IL were obtained with high reproducibility with the characterisation methodologies (TEM, UV-vis, XPS, and EXAFS) supporting the formation of a core-shell structure. The increase of Au content lead to an increase of a 1 nm, which can be related to the stabilisation mechanism of the AuPd NPs due to the higher affinity of the SO_2 groups present in the IL anion towards the Pd atoms in the incoming dimers and trimers. This interaction results in the formation of Au@Pd NPs stabilised in the IL, with Pd atoms on the surface interacting with the IL and Au atoms in the NPs core. This was concluded by using a combination of characterisation techniques such as electron microscopy, UV-Vis, XPS, and XAS.

In terms of catalysis, all AuPd NPs in IL presented activity towards the conversion of CAL with the exception of the Au_1, as expected. The changed in solvent did not altered the selectivity of the catalysts and the increase of temperature reinforced the themodinamic control with the increase of selectivity towards HCAL. The Pd_1 catalyst exhibited a clear dependency on the H_2 pressure, presenting considerable increase in conversion after 24h with the increase in pressure unlike the $Au_{0.4}Pd_{0.6}$ catalyst, which presented no

apparent dependency. The impact of different ratio in Au/Pd in the hydrogenation of CAL was also evaluated reaching a maximum with the $Au_{0.5}Pd_{0.5}$ catalyst (85%). This results corroborate the previous reports by other authors on the effect of AuPd NP, nonetheless, more detailed analysis of these profiles reveals that the differences in between the employed catalysts cannot be solely attributed to an enhancement of the rate as previously envisioned. A more complex process involving the loss of activity of the Pd_1 catalyst affecting the catalyst performance. This discrepancy was worth a deeper look at the catalysts produced, focusing on the $Au_{0.5}Pd_{0.5}$ and Pd_1. The mechanistic studies evaluating the effect of the substrates, [CAL] and [H_2] on the catalysts kinetic traces presented the dependency on both substrates and a Langmuir-Hinshelwood mechanism for the hydrogenation of CAL. The increase in both substrate concentration when Pd_1 presented to enhanced catalyst rate and conversion. These findings, in association with the results obtained for the product poisoning effect (HCAL) indicate an underlining catalyst deactivation dominating the reaction outcome. Both $Au_{0.5}Pd_{0.5}$ and Pd_1 catalysts present deactivation mechanism that are more predominant in the Pd_1 catalyst, that can diminished by increasing the substrate concentration, thus, stabilising the catalyst.

5.2 Future work

The work presented in this thesis demonstrate the use of IL as simple and quick method for the stabilisation of highly active core-shell AuPd NPs, that decrease the instability and deactivation effects present in monometallic Pd NPs in IL. As follow-up work, the investigation of the deactivation mechanisms in these catalysts should be performed. Before the interruption of this work, due to the Covid-19 pandemic, the deactivation studies were being performed showing the deactivation of the $Au_{0.5}Pd_{0.5}$ and Pd_1 catalysts with delayed start experiments. In these experiments, the introduction of H_2 is delayed from 2h to 24h. During this delayed time, the catalyst is left stirring in inert atmosphere, dissolved in THF, at 323 K and with or without CAL. After the delay time, H_2 is introduced and samples obtained in regular intervals (as in previously experiments). Preliminary results are presented in Figure 6.1 a) and b) for the delays where CAL is also introduced initially. This experiment presents the clear deactivation of both catalysts over time, showing that a phenomena is occurring leading to the deactivation of both catalysts in the absence of H_2. If the deactivation experiments are performed in the absence of both H_2 and CAL, the deactivation is more evident (Figure 6.2 a and b). The absence of CAL during the delay experiments, presents no evident difference on the catalytic performance of $Au_{0.5}Pd_{0.5}$ catalyst (Figure 6.2 a) in comparison to the results obtained in Figure 6.1 a. These results demonstrate the reduced influence of the presence of CAL in the deactivation mechanism / stabilisation of the $Au_{0.5}Pd_{0.5}$ catalyst. However, in the case of the Pd_1 catalyst (Figure 6.2 b) the absence of CAL during the delay time, leads to an increase of the

catalyst deactivation. Most importantly, these results, demonstrate, for the first time, that the addition of Au to Pd catalysts by co-deposition increases the stability of the catalysts and decreases their stability dependency on the substrate presence. This effect can lead to a decrease in the deactivation mechanism, thus leading to the increased conversion over time, as observed by several authors. These results are preliminary, performed in duplicate, and should be repeated promptly. In addition, delay experiments in the presence of HCAL should also be performed in order to evaluate the poisoning or stabilisation effect of the main product.

The effect of another IL, with a different anions (i.e. PF_6) should be tested. This experiments would provide further evidence on the stabilisation mechanism leading to core-shell structures in the presence of the $[NTf_2]^-$ anion and in the absence of the SO_2 groups, could lead to a random distribution of Pd and Au atoms on the NPs and therefore different catalytic properties.

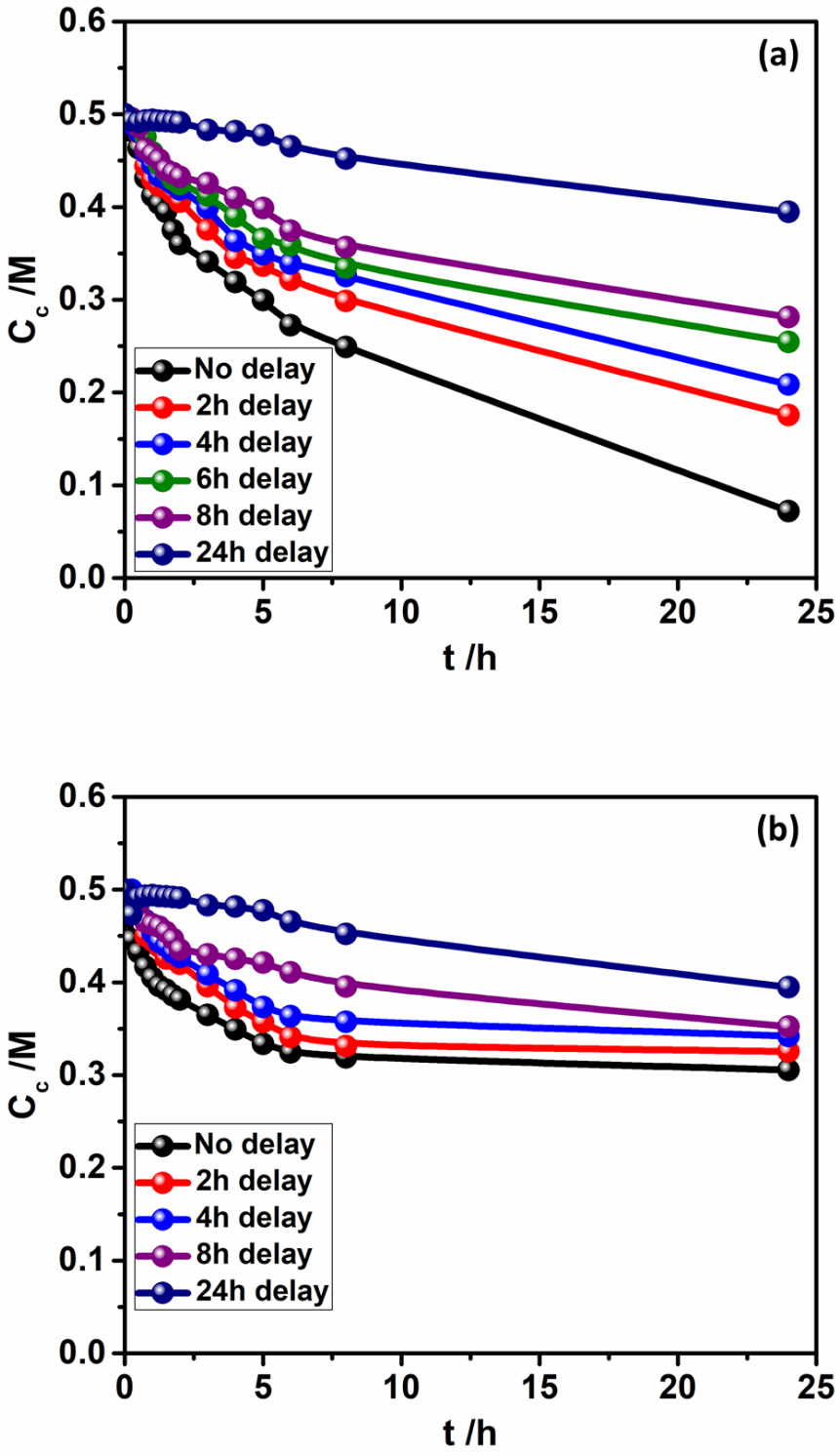

Figure 6.1 - Kinetic analysis undertaken with $Au_{0.5}Pd_{0.5}$ (a) and Pd_1 (b) catalysts depicting the effect of the delaying the introduction of H_2 on the catalysts performance. CAL introduced in the at t_0. All the parameters where maintained while the effect of [H_2] and [CAL] is essayed: 0.1 mol % catalyst, under 5 bar H_2 in the presence of 0.5M CAL in 10 mL THF at 323 K. All kinetic traces depicted here are displayed as [CAL], see chapter 2 for further information (Note also under the essayed reaction conditions selectivity > 95).

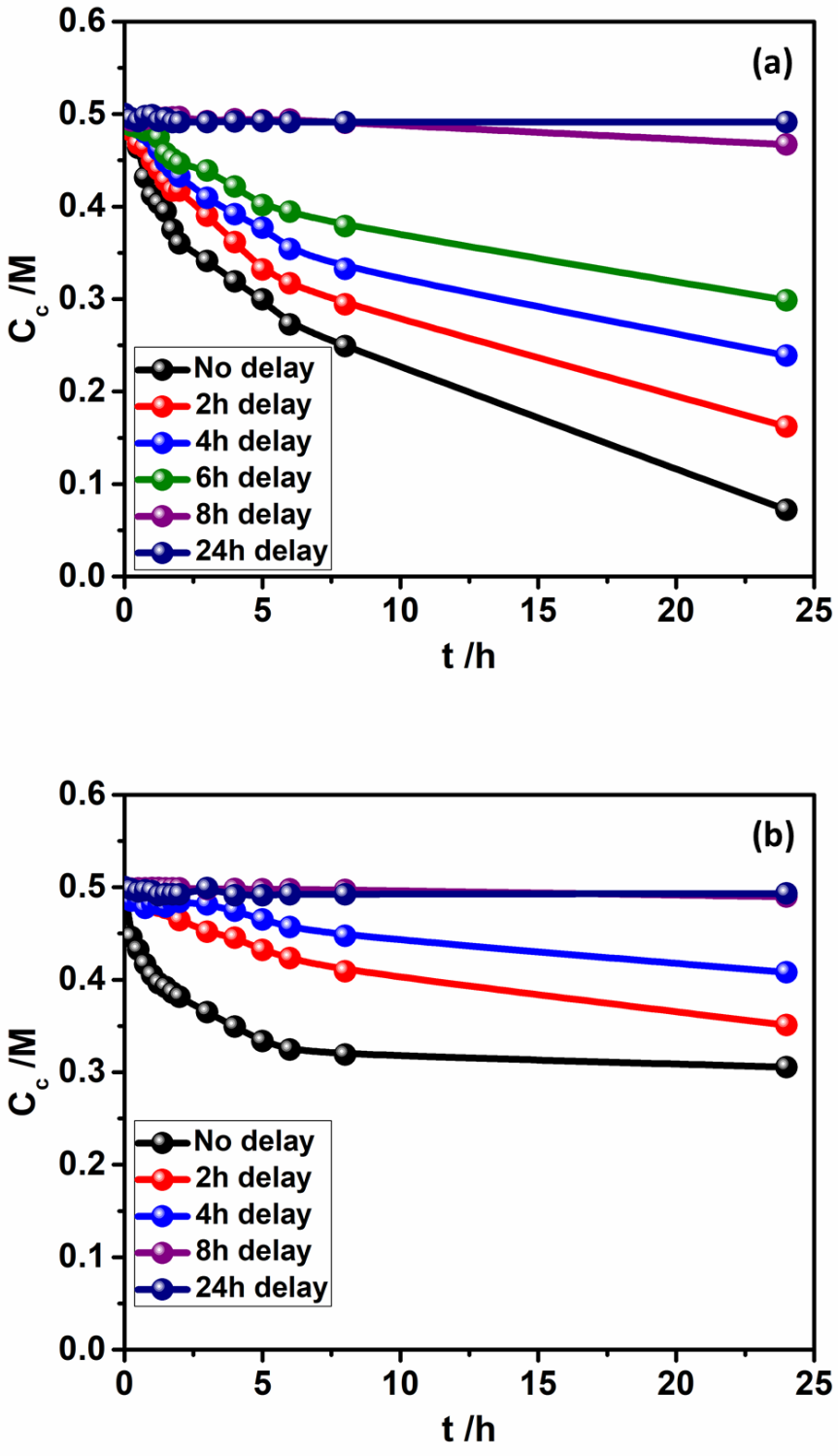

Figure 6.2 - Kinetic analysis undertaken with $Au_{0.5}Pd_{0.5}$ (a) and Pd_1 (b) catalysts depicting the effect of the delaying the introduction of H_2 on the catalysts performance. CAL introduced at the same time as H_2. All the parameters where maintained while the effect of [H_2] and [CAL] is essayed: 0.1 mol % catalyst, under 5 bar H_2 in the presence of 0.5M CAL in 10 mL THF at 323 K. All kinetic traces depicted here are displayed as [CAL], see chapter 2 for further information (Note also under the essayed reaction conditions selectivity > 95).

6. References

1. E. Roduner, *Chemical Society Reviews*, 2014, **43**, 8226-8239.
2. L. Lloyd, in *Handbook of Industrial Catalysts*, ed. L. Lloyd, Springer US, Boston, MA, 2011, pp. 1-22.
3. T. Bligaard and J. K. Nørskov, in *Chemical Bonding at Surfaces and Interfaces*, eds. A. Nilsson, L. G. M. Pettersson and J. K. Nørskov, Chemical Bonding at Surfaces and Interfaces, Amsterdam, 2008, pp. 255-321.
4. J. A. Dumesic, G. W. Huber and M. Boudart, in *Handbook of Heterogeneous Catalysis*.
5. A. Akah, *Journal of Rare Earths*, 2017, **35**, 941-956.
6. W. Zhan, Y. Guo, X. Gong, Y. Guo, Y. Wang and G. Lu, *Chinese Journal of Catalysis*, 2014, **35**, 1238-1250.
7. C. M. A. Parlett, K. Wilson and A. F. Lee, *Chemical Society Reviews*, 2013, **42**, 3876-3893.
8. G. A. Somorjai, *Langmuir*, 1991, **7**, 3176-3182.
9. I. Favier, D. Pla and M. Gómez, *Chemical Reviews*, 2020, **120**, 1146-1183.
10. Z. Li, S. Ji, Y. Liu, X. Cao, S. Tian, Y. Chen, Z. Niu and Y. Li, *Chemical Reviews*, 2020, **120**, 623-682.
11. E. Roduner, *Chemical Society Reviews*, 2006, **35**, 583-592.
12. A. Gazsi, T. Bánsági and F. Solymosi, *The Journal of Physical Chemistry C*, 2011, **115**, 15459-15466.
13. L. Luza, A. Gual, J. A. Fernandes, D. Eberhardt and J. Dupont, *Physical Chemistry Chemical Physics*, 2019, **21**, 16615-16622.
14. L. Luza, C. P. Rambor, A. Gual, J. Alves Fernandes, D. Eberhardt and J. Dupont, *ACS Catalysis*, 2017, **7**, 2791-2799.
15. G. C. Bond and P. A. Sermon, *Gold Bulletin*, 1973, **6**, 102-105.

16. P. Chaudhuri, C. N. Verani, E. Bill, E. Bothe, T. Weyhermüller and K. Wieghardt, *Journal of the American Chemical Society*, 2001, **123**, 2213-2223.

17. J. Zaanen, G. A. Sawatzky and J. W. Allen, *Physical Review Letters*, 1985, **55**, 418-421.

18. K. L. Kelly, E. Coronado, L. L. Zhao and G. C. Schatz, *The Journal of Physical Chemistry B*, 2003, **107**, 668-677.

19. S. Schauermann, J. Hoffmann, V. Johánek, J. Hartmann, J. Libuda and H.-J. Freund, *Angewandte Chemie International Edition*, 2002, **41**, 2532-2535.

20. X. Zhu, Q. Guo, Y. Sun, S. Chen, J.-Q. Wang, M. Wu, W. Fu, Y. Tang, X. Duan, D. Chen and Y. Wan, *Nature Communications*, 2019, **10**, 1428.

21. X. Lan and T. Wang, *ACS Catalysis*, 2020, **10**, 2764-2790.

22. J. Zhu, J. Wood, K. Deplanche, I. Mikheenko and L. E. Macaskie, *Applied Catalysis B: Environmental*, 2016, **199**, 108-122.

23. J. Liu, J. Shan, F. R. Lucci, S. Cao, E. C. H. Sykes and M. Flytzani-Stephanopoulos, *Catalysis Science & Technology*, 2017, **7**, 4276-4284.

24. D. Teschner, Z. Révay, J. Borsodi, M. Hävecker, A. Knop-Gericke, R. Schlögl, D. Milroy, S. D. Jackson, D. Torres and P. Sautet, *Angewandte Chemie International Edition*, 2008, **47**, 9274-9278.

25. Q.-A. Chen, Z.-S. Ye, Y. Duan and Y.-G. Zhou, *Chemical Society Reviews*, 2013, **42**, 497-511.

26. P. J. Miedziak, Q. He, J. K. Edwards, S. H. Taylor, D. W. Knight, B. Tarbit, C. J. Kiely and G. J. Hutchings, *Catalysis Today*, 2011, **163**, 47-54.

27. Z. Hou, N. Theyssen and W. Leitner, *Green Chemistry*, 2007, **9**, 127-132.

28. K. Mori, T. Hara, T. Mizugaki, K. Ebitani and K. Kaneda, *Journal of the American Chemical Society*, 2004, **126**, 10657-10666.

29. B. Karimi, S. Abedi, J. H. Clark and V. Budarin, *Angewandte Chemie International Edition*, 2006, **45**, 4776-4779.

30. M. Bahadori, S. Tangestaninejad, M. Moghadam, V. Mirkhani, A. Mechler, I. Mohammadpoor-Baltork and F. Zadehahmadi, *Microporous and Mesoporous Materials*, 2017, **253**, 102-111.

31. A. Ghorbani-Choghamarani, B. Tahmasbi, R. H. E. Hudson and A. Heidari, *Microporous and Mesoporous Materials*, 2019, **284**, 366-377.

32. Z. Chen, E. Vorobyeva, S. Mitchell, E. Fako, M. A. Ortuño, N. López, S. M. Collins, P. A. Midgley, S. Richard, G. Vilé and J. Pérez-Ramírez, *Nature Nanotechnology*, 2018, **13**, 702-707.

33. L. Zhang, M. Zhou, A. Wang and T. Zhang, *Chemical Reviews*, 2020, **120**, 683-733.

34. P. Gallezot and D. Richard, *Catalysis Reviews*, 1998, **40**, 81-126.

35. J. Dupont and J. D. Scholten, *Chemical Society Reviews*, 2010, **39**, 1780-1804.

36. J. D. Scholten, B. C. Leal and J. Dupont, *ACS Catalysis*, 2012, **2**, 184-200.

37. Y. Ptushinskiĭ, *Low Temperature Physics*, 2004, **30**.

38. R. Venkatesan, M. H. G. Prechtl, J. D. Scholten, R. P. Pezzi, G. Machado and J. Dupont, *Journal of Materials Chemistry*, 2011, **21**, 3030-3036.

39. Q. Zhang, W. Deng and Y. Wang, *Chemical Communications*, 2011, **47**, 9275-9292.

40. D. I. Enache, J. K. Edwards, P. Landon, B. Solsona-Espriu, A. F. Carley, A. A. Herzing, M. Watanabe, C. J. Kiely, D. W. Knight and G. J. Hutchings, *Science*, 2006, **311**, 362-365.

41. H. Zhang, T. Watanabe, M. Okumura, M. Haruta and N. Toshima, *Nature Materials*, 2012, **11**, 49-52.

42. N. Agarwal, S. J. Freakley, R. U. McVicker, S. M. Althahban, N. Dimitratos, Q. He, D. J. Morgan, R. L. Jenkins, D. J. Willock, S. H. Taylor, C. J. Kiely and G. J. Hutchings, *Science*, 2017, **358**, 223-227.

43. J. K. Edwards, B. E. Solsona, P. Landon, A. F. Carley, A. Herzing, C. J. Kiely and G. J. Hutchings, *Journal of Catalysis*, 2005, **236**, 69-79.

44. J. K. Edwards, B. Solsona, P. Landon, A. F. Carley, A. Herzing, M. Watanabe, C. J. Kiely and G. J. Hutchings, *Journal of Materials Chemistry*, 2005, **15**, 4595-4600.

45. D. W. Flaherty, *ACS Catalysis*, 2018, **8**, 1520-1527.

46. P. Landon, P. J. Collier, A. J. Papworth, C. J. Kiely and G. J. Hutchings, *Chemical Communications*, 2002, 2058-2059.

47. N. Agarwal, S. J. Freakley, R. U. McVicker, S. M. Althahban, N. Dimitratos, Q. He, D. J. Morgan, R. L. Jenkins, D. J. Willock, S. H. Taylor, C. J. Kiely and G. J. Hutchings, *Science*, 2017.

48. S. Cattaneo, S. J. Freakley, D. J. Morgan, M. Sankar, N. Dimitratos and G. J. Hutchings, *Catalysis Science & Technology*, 2018, **8**, 1677-1685.

49. M. Mavrikakis, B. Hammer and J. K. Nørskov, *Physical Review Letters*, 1998, **81**, 2819-2822.

50. J. R. Kitchin, J. K. Nørskov, M. A. Barteau and J. G. Chen, *The Journal of Chemical Physics*, 2004, **120**, 10240-10246.

51. D. A. Dowden, *Journal of the Chemical Society (Resumed)*, 1950, 242-265.

52. L. Luo, Z. Duan, H. Li, J. Kim, G. Henkelman and R. M. Crooks, *Journal of the American Chemical Society*, 2017, **139**, 5538-5546.

53. A. Wang, X. Y. Liu, C.-Y. Mou and T. Zhang, *Journal of Catalysis*, 2013, **308**, 258-271.

54. W. Luo, M. Sankar, A. M. Beale, Q. He, C. J. Kiely, P. C. A. Bruijnincx and B. M. Weckhuysen, *Nature Communications*, 2015, **6**, 6540.

55. A. J. Medford, A. Vojvodic, J. S. Hummelshøj, J. Voss, F. Abild-Pedersen, F. Studt, T. Bligaard, A. Nilsson and J. K. Nørskov, *Journal of Catalysis*, 2015, **328**, 36-42.

56. A. Villa, N. Dimitratos, C. E. Chan-Thaw, C. Hammond, G. M. Veith, D. Wang, M. Manzoli, L. Prati and G. J. Hutchings, *Chemical Society Reviews*, 2016, **45**, 4953-4994.

57. L. Liu and A. Corma, *Chemical Reviews*, 2018, **118**, 4981-5079.

58. Y. Yang, X. Shen and Y.-F. Han, *Applied Surface Science*, 2019, **483**, 991-1005.

59. C. T. Campbell, S. C. Parker and D. E. Starr, *Science*, 2002, **298**, 811-814.

60. C. T. Campbell, *Accounts of Chemical Research*, 2013, **46**, 1712-1719.

61. Y. Du, H. Sheng, D. Astruc and M. Zhu, *Chemical Reviews*, 2020, **120**, 526-622.

62. T. W. Hansen, A. T. DeLaRiva, S. R. Challa and A. K. Datye, *Accounts of Chemical Research*, 2013, **46**, 1720-1730.

63. K. Wettergren, F. F. Schweinberger, D. Deiana, C. J. Ridge, A. S. Crampton, M. D. Rötzer, T. W. Hansen, V. P. Zhdanov, U. Heiz and C. Langhammer, *Nano Letters*, 2014, **14**, 5803-5809.

64. S. T. Gentry, S. F. Kendra and M. W. Bezpalko, *The Journal of Physical Chemistry C*, 2011, **115**, 12736-12741.

65. S. R. Challa, A. T. Delariva, T. W. Hansen, S. Helveg, J. Sehested, P. L. Hansen, F. Garzon and A. K. Datye, *Journal of the American Chemical Society*, 2011, **133**, 20672-20675.

66. S. B. Simonsen, I. Chorkendorff, S. Dahl, M. Skoglundh, J. Sehested and S. Helveg, *Journal of Catalysis*, 2011, **281**, 147-155.

67. Á. Imre, D. L. Beke, E. Gontier-Moya, I. A. Szabó and E. Gillet, *Applied Physics A*, 2000, **71**, 19-22.

68. Y. Lei, H. Zhao, R. D. Rivas, S. Lee, B. Liu, J. Lu, E. Stach, R. E. Winans, K. W. Chapman, J. P. Greeley, J. T. Miller, P. J. Chupas and J. W. Elam, *Journal of the American Chemical Society*, 2014, **136**, 9320-9326.

69. J. Sá, S. F. R. Taylor, H. Daly, A. Goguet, R. Tiruvalam, Q. He, C. J. Kiely, G. J. Hutchings and C. Hardacre, *ACS Catalysis*, 2012, **2**, 552-560.

70. D. Kim, N. Becknell, Y. Yu and P. Yang, *Nano Letters*, 2017, **17**, 2732-2737.

71. X. Duan, X. Tian, J. Ke, Y. Yin, J. Zheng, J. Chen, Z. Cao, Z. Xie and Y. Yuan, *Chemical Science*, 2016, **7**, 3181-3187.

72. K. Morgan, A. Goguet and C. Hardacre, *ACS Catalysis*, 2015, **5**, 3430-3445.

73. H. Tsunoyama, H. Sakurai, Y. Negishi and T. Tsukuda, *Journal of the American Chemical Society*, 2005, **127**, 9374-9375.

74. R. P. Briñas, M. Hu, L. Qian, E. S. Lymar and J. F. Hainfeld, *Journal of the American Chemical Society*, 2008, **130**, 975-982.

75. R. Zanella, A. Sandoval, P. Santiago, V. A. Basiuk and J. M. Saniger, *The Journal of Physical Chemistry B*, 2006, **110**, 8559-8565.

76. E. N. Kusumawati and T. Sasaki, *The Chemical Record*, 2019, **19**, 2058-2068.

77. C. Kim and H. Lee, *Catalysis Communications*, 2009, **10**, 1305-1309.

78. J. Y. Park, C. Aliaga, J. R. Renzas, H. Lee and G. A. Somorjai, *Catalysis Letters*, 2009, **129**, 1-6.

79. P. G. Jessop, *Green Chemistry*, 2011, **13**, 1391-1398.

80. M. Freemantle, *Chemical & Engineering News Archive*, 1998, **76**, 32-37.

81. N. V. Plechkova and K. R. Seddon, *Chemical Society Reviews*, 2008, **37**, 123-150.

82. M. Petkovic, K. R. Seddon, L. P. N. Rebelo and C. Silva Pereira, *Chemical Society Reviews*, 2011, **40**, 1383-1403.

83. M. V. S. Oliveira, B. T. Vidal, C. M. Melo, R. d. C. M. de Miranda, C. M. F. Soares, J. A. P. Coutinho, S. P. M. Ventura, S. Mattedi and Á. S. Lima, *Chemosphere*, 2016, **147**, 460-466.

84. A. Jordan and N. Gathergood, *Chemical Society Reviews*, 2015, **44**, 8200-8237.

85. M. E. Heckenbach, F. N. Romero, M. D. Green and R. U. Halden, *Chemosphere*, 2016, **150**, 266-274.

86. D. O. Hartmann and C. S. Pereira, in *Ionic Liquids in Lipid Processing and Analysis*, eds. X. Xu, Z. Guo and L.-Z. Cheong, AOCS Press, 2016, pp. 403-421.

87. B. Wu, C. Dai, B. Chen, G. Yu, N. Liu and R. Xu, *ACS Sustainable Chemistry & Engineering*, 2019, **7**, 19194-19201.

88. T. J. S. Schubert, in *Ionic Liquids: Current State and Future Directions*, American Chemical Society, 2017, vol. 1250, ch. 3, pp. 35-65.

89. S. Anu Mary Ealia and M. P. Saravanakumar, *IOP Conference Series: Materials Science and Engineering*, 2017, **263**, 032019.

90. K. Manojkumar, A. Sivaramakrishna and K. Vijayakrishna, *Journal of Nanoparticle Research*, 2016, **18**, 103.

91. Z. He and P. Alexandridis, *Physical Chemistry Chemical Physics*, 2015, **17**, 18238-18261.

92. T. Welton, *Coordination Chemistry Reviews*, 2004, **248**, 2459-2477.

93. in *Handbook of Green Chemistry*, DOI: 10.1002/9783527628698.hgc085, pp. 1-31.

94. V. Campisciano, F. Giacalone and M. Gruttadauria, *The Chemical Record*, 2017, **17**, 918-938.

95. B. B. Polesso, F. L. Bernard, H. Z. Ferrari, E. A. Duarte, F. D. Vecchia and S. Einloft, *Heliyon*, 2019, **5**, e02183.

96. L. Zhu, L. Guo, Z. Zhang, J. Chen and S. Zhang, *Science China Chemistry*, 2012, **55**, 1479-1487.

97. C. P. Mehnert, R. A. Cook, N. C. Dispenziere and M. Afeworki, *Journal of the American Chemical Society*, 2002, **124**, 12932-12933.

98. A. Riisager, B. Jørgensen, P. Wasserscheid and R. Fehrmann, *Chemical Communications*, 2006, 994-996.

99. R. Kukawka, A. Pawlowska-Zygarowicz, J. Dzialkowska, M. Pietrowski, H. Maciejewski, K. Bica and M. Smiglak, *ACS Sustainable Chemistry & Engineering*, 2019, **7**, 4699-4706.

100. B. Wu, W. Liu, Y. Zhang and H. Wang, *Chemistry – A European Journal*, 2009, **15**, 1804-1810.

101. A. Stark, P. Behrend, O. Braun, A. Müller, J. Ranke, B. Ondruschka and B. Jastorff, *Green Chemistry*, 2008, **10**, 1152-1161.

102. J. Dupont and P. A. Z. Suarez, *Physical Chemistry Chemical Physics*, 2006, **8**, 2441-2452.

103. J. Dupont, P. A. Z. Suarez, R. F. De Souza, R. A. Burrow and J.-P. Kintzinger, *Chemistry – A European Journal*, 2000, **6**, 2377-2381.

104. M. Yang, P. S. Campbell, C. C. Santini and A.-V. Mudring, *Nanoscale*, 2014, **6**, 3367-3375.

105. P. Migowski and J. Dupont, *Chemistry – A European Journal*, 2007, **13**, 32-39.

106. J. P. Hallett and T. Welton, *Chemical Reviews*, 2011, **111**, 3508-3576.

107. H. Wender, P. Migowski, A. F. Feil, S. R. Teixeira and J. Dupont, *Coordination Chemistry Reviews*, 2013, **257**, 2468-2483.

108. L. Foppa, L. Luza, A. Gual, D. E. Weibel, D. Eberhardt, S. R. Teixeira and J. Dupont, *Dalton Transactions*, 2015, **44**, 2827-2834.

109. L. Luza, C. P. Rambor, A. Gual, F. Bernardi, J. B. Domingos, T. Grehl, P. Brüner and J. Dupont, *ACS Catalysis*, 2016, **6**, 6478-6486.

110. I. J. Villar-Garcia, K. R. J. Lovelock, S. Men and P. Licence, *Chemical Science*, 2014, **5**, 2573-2579.

111. M. M. Hassan, in *Handbook of Antimicrobial Coatings*, ed. A. Tiwari, Elsevier, 2018, pp. 321-355.

112. T. Suzuki, K.-i. Okazaki, S. Suzuki, T. Shibayama, S. Kuwabata and T. Torimoto, *Chemistry of Materials*, 2010, **22**, 5209-5215.

113. O. Ken-ichi, K. Tomonori, S. Toshimasa, K. Susumu and T. Tsukasa, *Chemistry Letters*, 2009, **38**, 330-331.

114. H. Wender, L. F. de Oliveira, P. Migowski, A. F. Feil, E. Lissner, M. H. G. Prechtl, S. R. Teixeira and J. Dupont, *The Journal of Physical Chemistry C*, 2010, **114**, 11764-11768.

115. E. Vanecht, K. Binnemans, J. W. Seo, L. Stappers and J. Fransaer, *Physical Chemistry Chemical Physics*, 2011, **13**, 13565-13571.

116. D. Sugioka, T. Kameyama, S. Kuwabata and T. Torimoto, *Physical Chemistry Chemical Physics*, 2015, **17**, 13150-13159.

117. T. Torimoto, K.-i. Okazaki, T. Kiyama, K. Hirahara, N. Tanaka and S. Kuwabata, *Applied Physics Letters*, 2006, **89**, 243117.

118. S. Suzuki, T. Suzuki, Y. Tomita, M. Hirano, K.-i. Okazaki, S. Kuwabata and T. Torimoto, *CrystEngComm*, 2012, **14**, 4922-4926.

119. L. Deng, M. T. Nguyen, J. Shi, Y.-t. R. Chau, T. Tokunaga, M. Kudo, S. Matsumura, N. Hashimoto and T. Yonezawa, *Langmuir*, 2020, **36**, 3004-3015.

120. D. Sugioka, T. Kameyama, S. Kuwabata, T. Yamamoto and T. Torimoto, *ACS Applied Materials & Interfaces*, 2016, **8**, 10874-10883.

121. H. Wender, R. V. Gonçalves, A. F. Feil, P. Migowski, F. S. Poletto, A. R. Pohlmann, J. Dupont and S. R. Teixeira, *The Journal of Physical Chemistry C*, 2011, **115**, 16362-16367.

122. S. Kuwabata, T. Tsuda and T. Torimoto, *The Journal of Physical Chemistry Letters*, 2010, **1**, 3177-3188.

123. J. Charpentier, R. Emter, H. Koch, D. Lelièvre, X. Pannecoucke, S. Couve-Bonnaire, A. Natsch and A. Bombrun, *Chemistry & Biodiversity*, 2018, **15**, e1800013.

124. J. Cocchiara, C. S. Letizia, J. Lalko, A. Lapczynski and A. M. Api, *Food and Chemical Toxicology*, 2005, **43**, 867-923.

125. A. Z. El-Sonbati, A. A. El-Bindary, M. A. Diab, M. A. El-Ela and S. A. Mazrouh, *Polymer Degradation and Stability*, 1993, **42**, 1-11.

126. K. R. Zodrow, J. D. Schiffman and M. Elimelech, *Langmuir*, 2012, **28**, 13993-13999.

127. K. A. Rieger and J. D. Schiffman, *Carbohydrate Polymers*, 2014, **113**, 561-568.

128. M. Harada and S. Yano, *CHEMICAL & PHARMACEUTICAL BULLETIN*, 1975, **23**, 941-947.

129. P. Khare, S. Jagtap, Y. Jain, R. K. Baboota, P. Mangal, R. K. Boparai, K. K. Bhutani, S. S. Sharma, L. S. Premkumar, K. K. Kondepudi, K. Chopra and M. Bishnoi, *BioFactors*, 2016, **42**, 201-211.

130. L. d. C. Fardelone, J. Augusto, R. Rodrigues and P. J. S. Moran, *Journal of Molecular Catalysis B: Enzymatic*, 2004, **29**, 41-45.

131. P. Mäki-Arvela, J. Hájek and T. Salmi, *Applied Catalysis A-general - APPL CATAL A-GEN*, 2005, **292**, 1-49.

132. L. Liu, B. Lukose, P. Jaque and B. Ensing, *Green Energy & Environment*, 2019, **4**, 20-28.

133. I. G. Yefremenko, I. L. Zilberberg, G. M. Zhidomirov and A. M. Pak, *Reaction Kinetics and Catalysis Letters*, 1995, **56**, 77-86.

134. D. G. Narehood, S. Kishore, H. Goto, J. H. Adair, J. A. Nelson, H. R. Gutiérrez and P. C. Eklund, *International Journal of Hydrogen Energy*, 2009, **34**, 952-960.

135. S. Fantasia, J. D. Egbert, V. Jurcík, C. S. Cazin, H. Jacobsen, L. Cavallo, D. M. Heinekey and S. P. Nolan, *Angewandte Chemie (International ed. in English)*, 2009, **48**, 5182-5186.

136. S. Mousavi, B. Nazari, M. H. Keshavarz and A.-K. Bordbar, *Industrial & Engineering Chemistry Research*, 2020, **59**, 1862-1874.

137. S. Wang, Z.-J. Zhao, X. Chang, J. Zhao, H. Tian, C. Yang, M. Li, Q. Fu, R. Mu and J. Gong, *Angewandte Chemie International Edition*, 2019, **58**, 7668-7672.

138. T. Mitsudome, Y. Mikami, M. Matoba, T. Mizugaki, K. Jitsukawa and K. Kaneda, *Angewandte Chemie International Edition*, 2012, **51**, 136-139.

139. I. Cano, A. M. Chapman, A. Urakawa and P. W. N. M. van Leeuwen, *Journal of the American Chemical Society*, 2014, **136**, 2520-2528.

140. I. Cano, M. A. Huertos, A. M. Chapman, G. Buntkowsky, T. Gutmann, P. B. Groszewicz and P. W. N. M. van Leeuwen, *Journal of the American Chemical Society*, 2015, **137**, 7718-7727.

141. P. Mäki-Arvela, J. Hájek, T. Salmi and D. Y. Murzin, *Applied Catalysis A: General*, 2005, **292**, 1-49.

142. A. Daimon, T. Kamitanaka, N. Kishida, T. Matsuda and T. Harada, *The Journal of Supercritical Fluids*, 2006, **37**, 215-219.

143. F. Christie, A. Zanotti-Gerosa and D. Grainger, *ChemCatChem*, 2018, **10**, 1012-1018.

144. H. Liu, Q. Mei, S. Li, Y. Yang, Y. Wang, H. Liu, L. Zheng, P. An, J. Zhang and B. Han, *Chemical Communications*, 2018, **54**, 908-911.

145. M. Zhao, K. Yuan, Y. Wang, G. Li, J. Guo, L. Gu, W. Hu, H. Zhao and Z. Tang, *Nature*, 2016, **539**, 76-80.

146. F. R. Lucci, M. T. Darby, M. F. G. Mattera, C. J. Ivimey, A. J. Therrien, A. Michaelides, M. Stamatakis and E. C. H. Sykes, *The Journal of Physical Chemistry Letters*, 2016, **7**, 480-485.

147. H. Liu, Z. Li and Y. Li, *Industrial & Engineering Chemistry Research*, 2015, **54**, 1487-1497.

148. H. Shi, N. Xu, D. Zhao and B.-Q. Xu, *Catalysis Communications*, 2008, **9**, 1949-1954.

149. P. Dash, N. A. Dehm and R. W. J. Scott, *Journal of Molecular Catalysis A: Chemical*, 2008, **286**, 114-119.

150. H. Lineweaver and D. Burk, *Journal of the American Chemical Society*, 1934, **56**, 658-666.

151. M. Freemantle, *Chemical & Engineering News Archive*, 2003, **81**, 27-30.

152. C. D. T. Nielsen and J. Burés, *Chemical Science*, 2019, **10**, 348-353.

153. J. Burés, *Angewandte Chemie International Edition*, 2016, **55**, 16084-16087.

154. J. Burés, *Angewandte Chemie International Edition*, 2016, **55**, 2028-2031.

155. M. Bowker, *Chemical Vapor Deposition*, 1995, **1**, 90-90.

156. G. Heiland, *Berichte der Bunsengesellschaft für physikalische Chemie*, 1975, **79**, 641-641.

157. P. W. Atkins and J. De Paula, *Atkins' Physical Chemistry*, Macmillan Higher Education, 2006.

158. E. F. Borra, O. Seddiki, R. Angel, D. Eisenstein, P. Hickson, K. R. Seddon and S. P. Worden, *Nature*, 2007, **447**, 979-981.

159. K.-i. Okazaki, T. Kiyama, T. Suzuki, S. Kuwabata and T. Torimoto, *Chemistry Letters*, 2009, **38**, 330-331.

160. D. M. Mattox, *Journal of Vacuum Science & Technology A*, 1989, **7**, 1105-1114.

161. P. J. Kelly and R. D. Arnell, *Vacuum*, 2000, **56**, 159-172.

162. U. Helmersson, M. Lattemann, J. Bohlmark, A. P. Ehiasarian and J. T. Gudmundsson, *Thin Solid Films*, 2006, **513**, 1-24.

163. K. Yoshii, T. Tsuda, T. Arimura, A. Imanishi, T. Torimoto and S. Kuwabata, *RSC Advances*, 2012, **2**, 8262-8264.

164. D. Wang, Dordrecht, 2006.

165. D. Su, *Green Energy & Environment*, 2017, **2**, 70-83.

166. M. Asadi Asadabad and M. Jafari Eskandari, *Synthesis and Reactivity in Inorganic, Metal-Organic, and Nano-Metal Chemistry*, 2015, **45**, 323-326.

167. W. D. Pyrz and D. J. Buttrey, *Langmuir*, 2008, **24**, 11350-11360.

168. W. Zhou and H. F. Greer, *European Journal of Inorganic Chemistry*, 2016, **2016**, 941-950.

169. J. L. Fenton, J. M. Hodges and R. E. Schaak, *Chemistry of Materials*, 2017, **29**, 6168-6177.

170. Y. Leng, in *Transmission Electron Microscopy. In Materials Characterization*, 2013, ch. Chapter 3, pp. 83-126.

171. Y. Leng, in *Transmission Electron Microscopy. In Electron Spectroscopy for Surface Analysis*, 2013, ch. Chapter 7, pp. 221-251.

172. C. Hetherington, *Materials Today*, 2004, **7**, 50-55.

173. C. Aliaga, C. S. Santos and S. Baldelli, *Physical Chemistry Chemical Physics*, 2007, **9**, 3683-3700.

174. C. Verma, E. E. Ebenso and M. A. Quraishi, *Journal of Molecular Liquids*, 2019, **276**, 826-849.

175. S. Wegner and C. Janiak, *Topics in Current Chemistry*, 2017, **375**, 65.

176. C. Valdebenito, J. Pinto, M. Nazarkovsky, G. Chacón, O. Martínez-Ferraté, K. Wrighton-Araneda, D. Cortés-Arriagada, M. B. Camarada, J. Alves Fernandes and G. Abarca, *Nanoscale Advances*, 2020, **2**, 1325-1332.

177. T. Carlson, *Photoelectron and Auger Spectroscopy*, Springer US, 2013.

178. A. G. Shard, *Surface and Interface Analysis*, 2014, **46**, 175-185.

179. in *An Introduction to Surface Analysis by XPS and AES. Comparison of XPS and AES with Other Analytical Techniques*, ch. Chapter 6, pp. 165-182.

180. I. J. Villar-Garcia, E. F. Smith, A. W. Taylor, F. Qiu, K. R. J. Lovelock, R. G. Jones and P. Licence, *Physical Chemistry Chemical Physics*, 2011, **13**, 2797-2808.

181. C. S. S. C. Ridgway, *X-Ray Absorption Spectroscopy of Semiconductors*, Springer, Berlin, Heidelberg, 2015.

182. D. C. Koningsberger, *X-ray absorption: principles, applications, techniques of EXAFS, SEXAFS, and XANES*, John Wiley and Sons, United States, 1988.

183. H. Kohlmann, in *Encyclopedia of Physical Science and Technology (Third Edition)*, ed. R. A. Meyers, Academic Press, New York, 2003, pp. 441-458.

184. J. G. Parsons, M. V. Aldrich and J. L. Gardea-Torresdey, *Applied Spectroscopy Reviews*, 2002, **37**, 187-222.

185. P. Paufler, *Journal of Synchrotron Radiation*, 2011, **18**, 818.

186. M. Wang, L. Árnadóttir, Z. J. Xu and Z. Feng, *Nano-Micro Letters*, 2019, **11**, 47.

187. J. G. Huddleston, A. E. Visser, W. M. Reichert, H. D. Willauer, G. A. Broker and R. D. Rogers, *Green Chemistry*, 2001, **3**, 156-164.

188. P. Bonhôte, A.-P. Dias, N. Papageorgiou, K. Kalyanasundaram and M. Grätzel, *Inorganic Chemistry*, 1996, **35**, 1168-1178.

189. J. Yano and V. K. Yachandra, *Photosynth Res*, 2009, **102**, 241-254.

190. D. Kim, J. Resasco, Y. Yu, A. M. Asiri and P. Yang, *Nature Communications*, 2014, **5**, 4948.

191. G. Sharma, A. Kumar, S. Sharma, M. Naushad, R. Prakash Dwivedi, Z. A. Alothman and G. T. Mola, *Journal of King Saud University - Science*, 2019, **31**, 257-269.

192. R. Izumi, Y. Yao, T. Tsuda, T. Torimoto and S. Kuwabata, *Journal of Materials Chemistry A*, 2018, **6**, 11853-11862.

193. C.-H. Liu, B.-H. Mao, J. Gao, S. Zhang, X. Gao, Z. Liu, S.-T. Lee, X.-H. Sun and S.-D. Wang, *Carbon*, 2012, **50**, 3008-3014.

194. M. T. Nguyen and T. Yonezawa, *Science and Technology of Advanced Materials*, 2018, **19**, 883-898.

195. B. Ramalingam, S. Mukherjee, C. J. Mathai, K. Gangopadhyay and S. Gangopadhyay, *Nanotechnology*, 2013, **24**, 205602.

196. M. Yun, B. Ramalingam and S. Gangopadhyay, *Nanotechnology*, 2011, **22**, 465201.

197. T. Cremer, M. Stark, A. Deyko, H. P. Steinrück and F. Maier, *Langmuir*, 2011, **27**, 3662-3671.

198. H. Zheng, R. K. Smith, Y.-w. Jun, C. Kisielowski, U. Dahmen and A. P. Alivisatos, *Science*, 2009, **324**, 1309-1312.

199. T. Uematsu, M. Baba, Y. Oshima, T. Tsuda, T. Torimoto and S. Kuwabata, *Journal of the American Chemical Society*, 2014, **136**, 13789-13797.

200. K.-i. Okazaki, T. Kiyama, K. Hirahara, N. Tanaka, S. Kuwabata and T. Torimoto, *Chemical Communications*, 2008, 691-693.

201. K. Loza, M. Heggen and M. Epple, *Advanced Functional Materials*, 2020, **30**, 1909260.

202. H. T. Beyene, V. S. K. Chakravadhanula, C. Hanisch, M. Elbahri, T. Strunskus, V. Zaporojtchenko, L. Kienle and F. Faupel, *Journal of Materials Science*, 2010, **45**, 5865-5871.

203. K. M. Kosuda, J. Wiester, K. L. Wustholz, R. P. Duyne and R. J. Groarke, 2016.

204. W. Haiss, N. T. K. Thanh, J. Aveyard and D. G. Fernig, *Analytical Chemistry*, 2007, **79**, 4215-4221.

205. V. Amendola and M. Meneghetti, *The Journal of Physical Chemistry C*, 2009, **113**, 4277-4285.

206. O. Metin, X. Sun and S. Sun, *Nanoscale*, 2013, **5**, 910-912.

207. H. Guo, Y. Chen, X. Chen, R. Wen, G.-H. Yue and D.-L. Peng, *Nanotechnology*, 2011, **22**, 195604.

208. A. R. Santos, R. K. Blundell and P. Licence, *Physical chemistry chemical physics : PCCP*, 2015, **17**, 11839-11847.

209. L. Chen, A. Yelon and E. Sacher, *The Journal of Physical Chemistry C*, 2011, **115**, 7896-7905.

210. M. G. Mason, S. T. Lee, G. Apai, R. F. Davis, D. A. Shirley, A. Franciosi and J. H. Weaver, *Physical Review Letters*, 1981, **47**, 730-733.

211. J. Kua and W. A. Goddard, *The Journal of Physical Chemistry B*, 1998, **102**, 9481-9491.

212. M. G. Mason, L. J. Gerenser and S. T. Lee, *Physical Review Letters*, 1977, **39**, 288-291.

213. J. Radnik, C. Mohr and P. Claus, *Physical Chemistry Chemical Physics*, 2003, **5**, 172-177.

214. A. S. Pensado and A. A. H. Pádua, *Angewandte Chemie International Edition*, 2011, **50**, 8683-8687.

215. M. W. Tew, J. T. Miller and J. A. van Bokhoven, *The Journal of Physical Chemistry C*, 2009, **113**, 15140-15147.

216. Y. Lei, J. Jelic, L. C. Nitsche, R. Meyer and J. Miller, *Topics in Catalysis*, 2011, **54**, 334-348.

217. Y. Nagai, T. Yamamoto, T. Tanaka, S. Yoshida, T. Nonaka, T. Okamoto, A. Suda and M. Sugiura, *Catalysis Today*, 2002, **74**, 225-234.

218. V. V. Srabionyan, A. L. Bugaev, V. V. Pryadchenko, L. A. Avakyan, J. A. van Bokhoven and L. A. Bugaev, *Journal of Physics and Chemistry of Solids*, 2014, **75**, 470-476.

219. S. Krüger, S. Vent and N. Rösch, *Berichte der Bunsengesellschaft für physikalische Chemie*, 1997, **101**, 1640-1643.

220. A. W. Pelzer, J. Jellinek and K. A. Jackson, *The Journal of Physical Chemistry A*, 2013, **117**, 10407-10415.

221. S. Nayab, H.-I. Lee and J. H. Jeong, *Acta Crystallogr Sect E Struct Rep Online*, 2013, **69**, m238-m239.

222. Y. Sun, A. I. Frenkel, R. Isseroff, C. Shonbrun, M. Forman, K. Shin, T. Koga, H. White, L. Zhang, Y. Zhu, M. H. Rafailovich and J. C. Sokolov, *Langmuir*, 2006, **22**, 807-816.

223. Y. Nagai, K. Dohmae, Y. Ikeda, N. Takagi, T. Tanabe, N. Hara, G. Guilera, S. Pascarelli, M. A. Newton, O. Kuno, H. Jiang, H. Shinjoh and S. i. Matsumoto, *Angewandte Chemie International Edition*, 2008, **47**, 9303-9306.

224. D. Chen, J. Li, P. Cui, H. Liu and J. Yang, *Journal of Materials Chemistry A*, 2016, **4**, 3813-3821.

225. A. Agarwal, M. K. Singh and A. N. Vishnoi, *Indian Journal of Physics*, 2010, **84**, 199-204.

226. J. Ohyama, K. Teramura, T. Shishido, Y. Hitomi, K. Kato, H. Tanida, T. Uruga and T. Tanaka, *Chemical Physics Letters*, 2011, **507**, 105-110.

227. Y. Suo and I. M. Hsing, *Electrochimica Acta*, 2011, **56**, 2174-2183.

228. X. Huang, H. Wu, S. Pu, W. Zhang, X. Liao and B. Shi, *Green Chemistry*, 2011, **13**, 950-957.

229. L. Lu, G. Burkey, I. Halaciuga and D. V. Goia, *Journal of Colloid and Interface Science*, 2013, **392**, 90-95.

230. K.-T. Yong, Y. Sahoo, M. T. Swihart and P. N. Prasad, *Colloids and Surfaces A: Physicochemical and Engineering Aspects*, 2006, **290**, 89-105.

231. P. Vámosi, K. Matsuo, T. Masuda, K. Sato, T. Narumi, K. Takeda and N. Mase, *The Chemical Record*, 2019, **19**, 77-84.

232. Z. Zhou, X. Li and R. N. Zare, *ACS Central Science*, 2017, **3**, 1337-1344.

233. L. Červenýa and V. Rûržička, in *Advances in Catalysis*, eds. D. D. Eley, H. Pines and P. B. Weisz, Academic Press, 1981, vol. 30, pp. 335-377.

234. P. J. Dyson and P. G. Jessop, *Catalysis Science & Technology*, 2016, **6**, 3302-3316.

235. D. Y. Murzin, *Catalysis Science & Technology*, 2016, **6**, 5700-5713.

236. H. M. L. Davies, P. R. Bruzinski, D. H. Lake, N. Kong and M. J. Fall, *Journal of the American Chemical Society*, 1996, **118**, 6897-6907.

237. L. Gilbert and C. Mercier, in *Studies in Surface Science and Catalysis*, eds. M. Guisnet, J. Barbier, J. Barrault, C. Bouchoule, D. Duprez, G. Pérot and C. Montassier, Elsevier, 1993, vol. 78, pp. 51-66.

238. E. Brunner, *Journal of Chemical & Engineering Data*, 1985, **30**, 269-273.

239. M. Bäumer, J. Libuda, K. M. Neyman, N. Rösch, G. Rupprechter and H.-J. Freund, *Physical Chemistry Chemical Physics*, 2007, **9**, 3541-3558.

240. S. Moret, P. J. Dyson and G. Laurenczy, *Nature Communications*, 2014, **5**, 4017.

241. A. Weilhard, S. P. Argent and V. Sans, *Nature Communications*, 2021, **12**, 231.

242. K.-C. Lin, *Journal of Chemical Education*, 1988, **65**, 857.

243. M. Khan, S. Joshi and V. Ranade, *Chemical Engineering Journal*, 2019, **377**, 120512.

244. T. Katayama and T. Nitta, *Journal of Chemical & Engineering Data*, 1976, **21**, 194-196.

245. D. G. Blackmond, *Angewandte Chemie International Edition*, 2005, **44**, 4302-4320.

246. C. H. Bartholomew, *Applied Catalysis A: General*, 2001, **212**, 17-60.

247. G. Boskovic and M. Baerns, in *Basic Principles in Applied Catalysis*, ed. M. Baerns, Springer Berlin Heidelberg, Berlin, Heidelberg, 2004, pp. 477-503.

248. R. J. Baxter and P. Hu, *The Journal of Chemical Physics*, 2002, **116**, 4379-4381.

249. I. Tkatchenko, in *Comprehensive Organometallic Chemistry*, eds. G. Wilkinson, F. G. A. Stone and E. W. Abel, Pergamon, Oxford, 1982, pp. 101-223.

250. V. M. Chernyshev, A. V. Astakhov, I. E. Chikunov, R. V. Tyurin, D. B. Eremin, G. S. Ranny, V. N. Khrustalev and V. P. Ananikov, *ACS Catalysis*, 2019, **9**, 2984-2995.

251. in *Studies in Surface Science and Catalysis*, ed. J. M. Berty, Elsevier, 1999, vol. 124, pp. 261-268.

252. P. Albers, J. Pietsch and S. F. Parker, *Journal of Molecular Catalysis A: Chemical*, 2001, **173**, 275-286.

253. J. L. Figueiredo and F. R. Ribeiro, in *Combinatorial Catalysis and High Throughput Catalyst Design and Testing*, eds. E. G. Derouane, F. Lemos, A. Corma and F. R. Ribeiro, Springer Netherlands, Dordrecht, 2000, pp. 145-173.

Appendices

Appendix 1

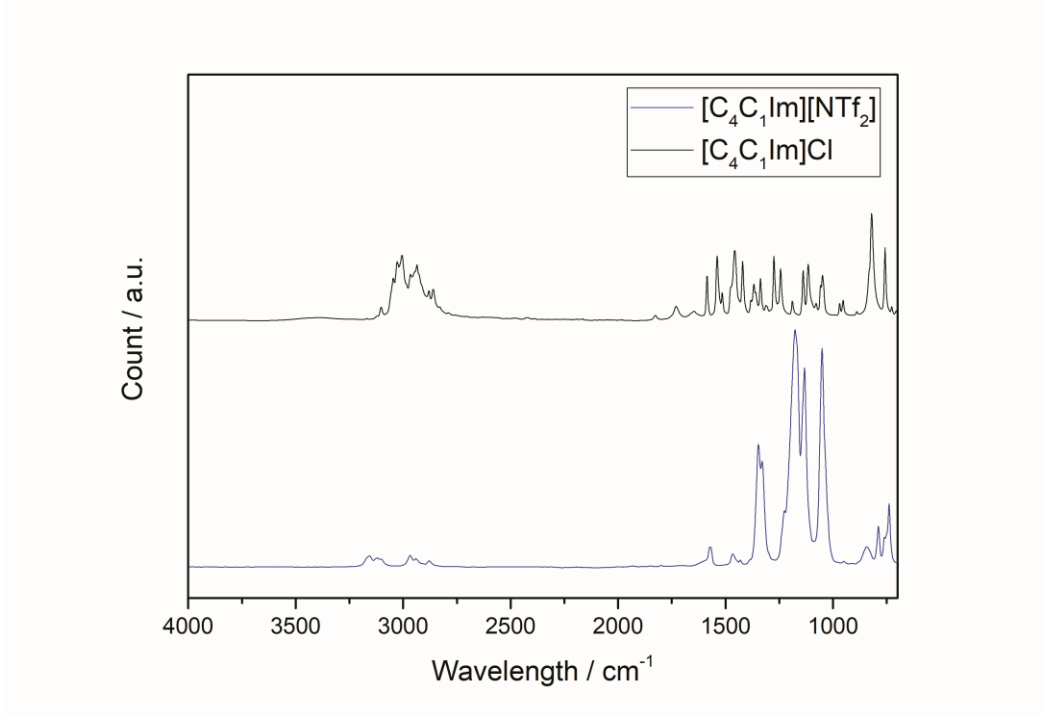

Figure S1 - IR spectra of the ILs produced.

Appendix 2

Table S6 - Magnetron sputtering parameters for Au NPs deposition in IL. Depositions were performed in triplicate.

Sample	Au (wt%)	Pd (wt%)	Pd (atomic %)	Au (atomic %)	Power Pd (W)	Voltage Pd (V)	Current Pd (Amp)	Power Au (W)	Voltage Au (V)	Current Au (Amp)	Deposition time (min)
Au_1	0.94 (±0.035)	0.00	0.0	100	0	-	-	30	343	0.083	50
$Au_{0.80}Pd_{0.20}$	6.82 (±0.040)	0.85 (±0.041)	18.7	81.3	30	342	0.083	120	397	0.29	180
$Au_{0.50}Pd_{0.50}$	1.43 (0.035)	0.85 (±0.024)	52.4	47.6	60	311	0.19	90	383	0.24	50
$Au_{0.40}Pd_{0.60}$	0.94 (±0.022)	0.85 (±0.023)	62.6	37.4	60	329	0.19	30	342	0.083	50
$Au_{0.25}Pd_{0.75}$	0.53 (±0.015)	0.87 (±0.034)	75.3	24.7	60	328	0.19	15	302	0.058	50
Pd_1	0	0.85 (±0.022)	100	0.0	60	335	0.18	0	-	-	50

Appendix 3

The survey and high resolution scans of all the described AuPd NPs in IL are presented in this section. The binding energies and full width at half maximum (FWHM) values are presented in *Appendix 4*.

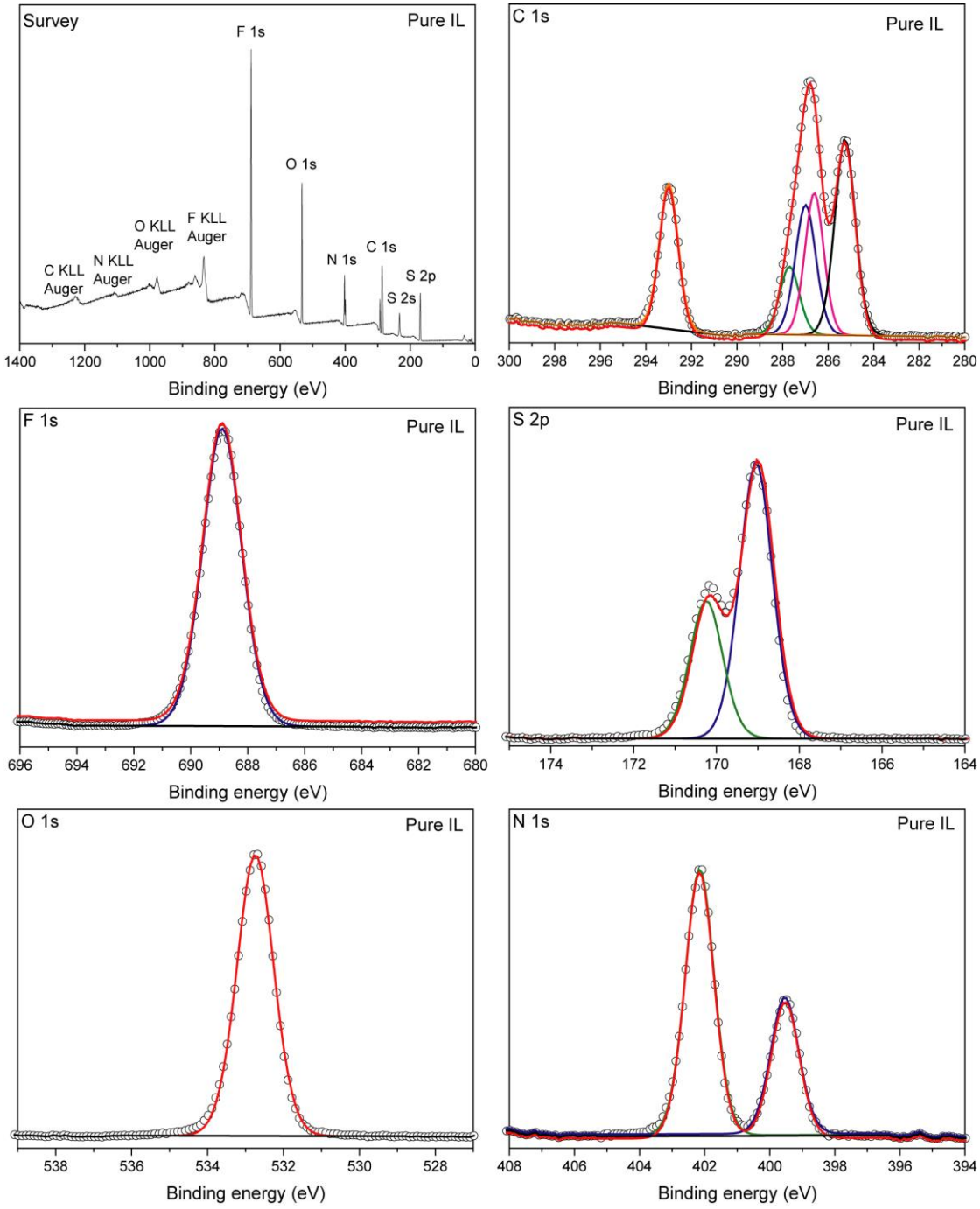

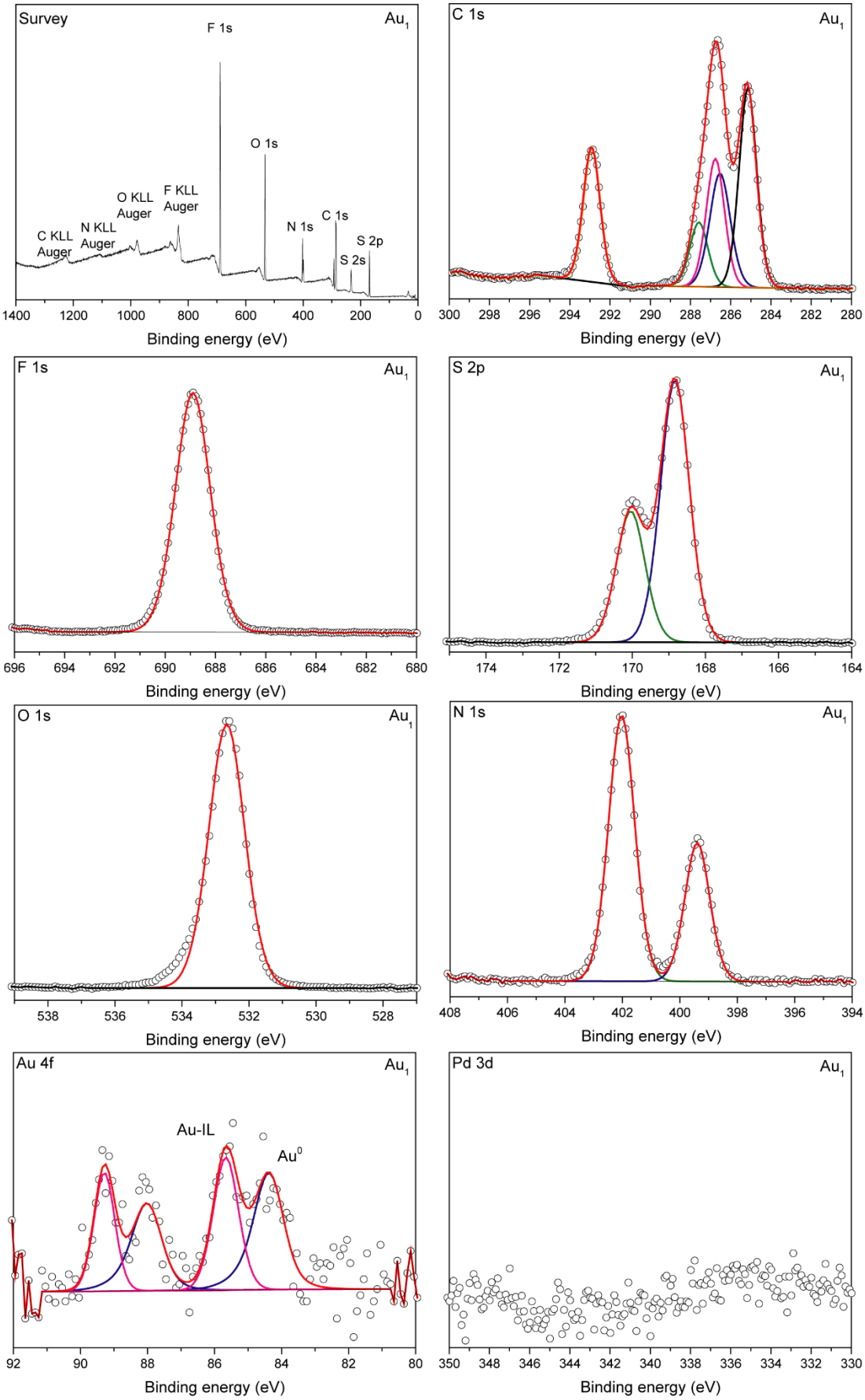
Survey
Au1
F 1s
O 1s
O KLL Auger
F KLL Auger
C KLL Auger
N KLL Auger
N 1s
C 1s
S 2p
S 2s
1400 1200 1000 800 600 400 200 0
Binding energy (eV)
C 1s
Au1
300 298 296 294 292 290 288 286 284 282 280
Binding energy (eV)
F 1s
Au1
696 694 692 690 688 686 684 682 680
Binding energy (eV)
S 2p
Au1
174 172 170 168 166 164
Binding energy (eV)
O 1s
Au1
538 536 534 532 530 528
Binding energy (eV)
N 1s
Au1
408 406 404 402 400 398 396 394
Binding energy (eV)
Au 4f
Au1
Au-IL
Au0
92 90 88 86 84 82 80
Binding energy (eV)
Pd 3d
Au1
350 348 346 344 342 340 338 336 334 332 330
Binding energy (eV)

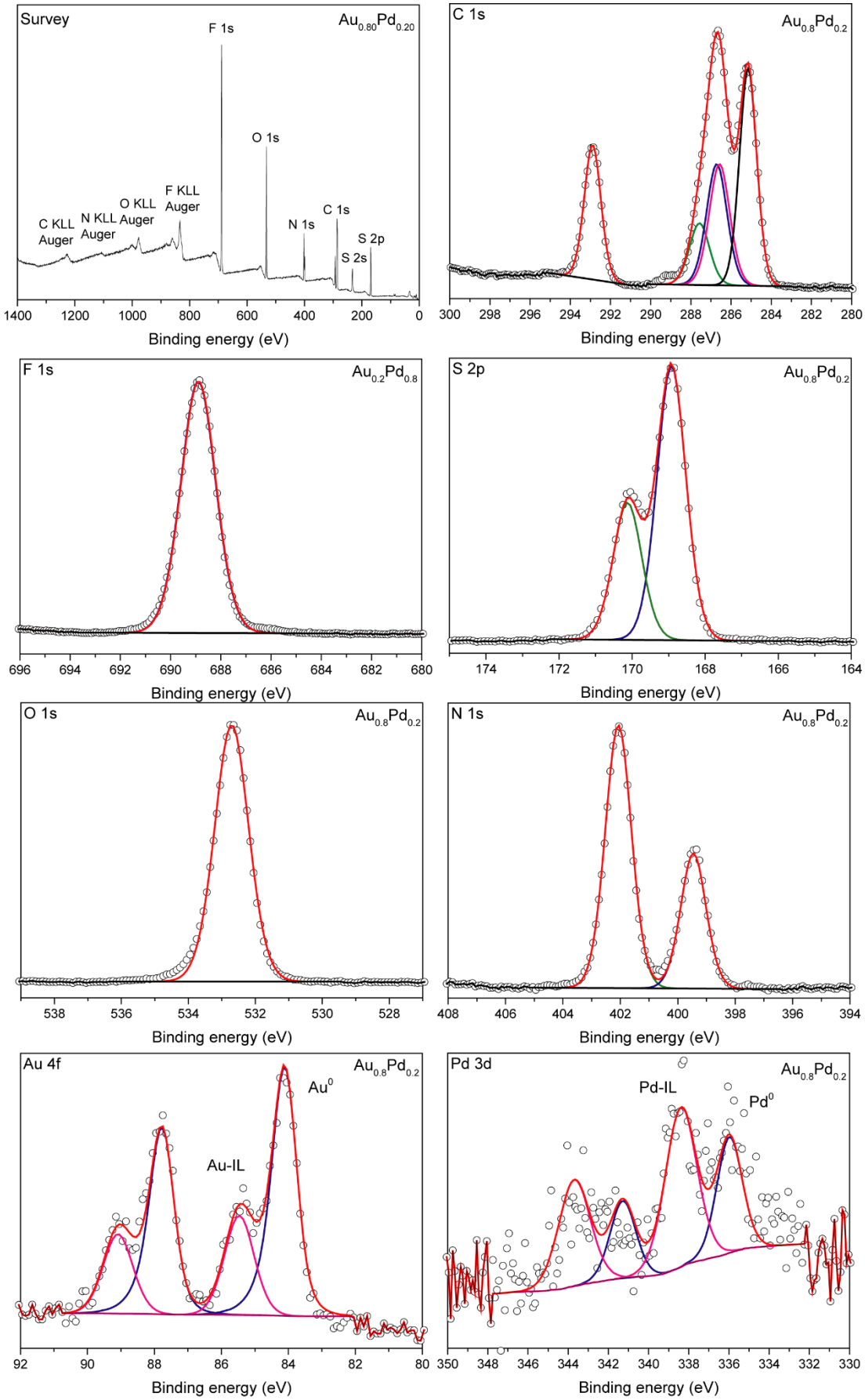
Survey
$Au_{0.80}Pd_{0.20}$
F 1s
O 1s
C KLL Auger
N KLL Auger
O KLL Auger
F KLL Auger
N 1s
C 1s
S 2p
S 2s
Binding energy (eV)
C 1s
$Au_{0.8}Pd_{0.2}$
Binding energy (eV)
F 1s
$Au_{0.2}Pd_{0.8}$
Binding energy (eV)
S 2p
$Au_{0.8}Pd_{0.2}$
Binding energy (eV)
O 1s
$Au_{0.8}Pd_{0.2}$
Binding energy (eV)
N 1s
$Au_{0.8}Pd_{0.2}$
Binding energy (eV)
Au 4f
$Au_{0.8}Pd_{0.2}$
Au^0
Au-IL
Binding energy (eV)
Pd 3d
$Au_{0.8}Pd_{0.2}$
Pd-IL
Pd^0
Binding energy (eV)

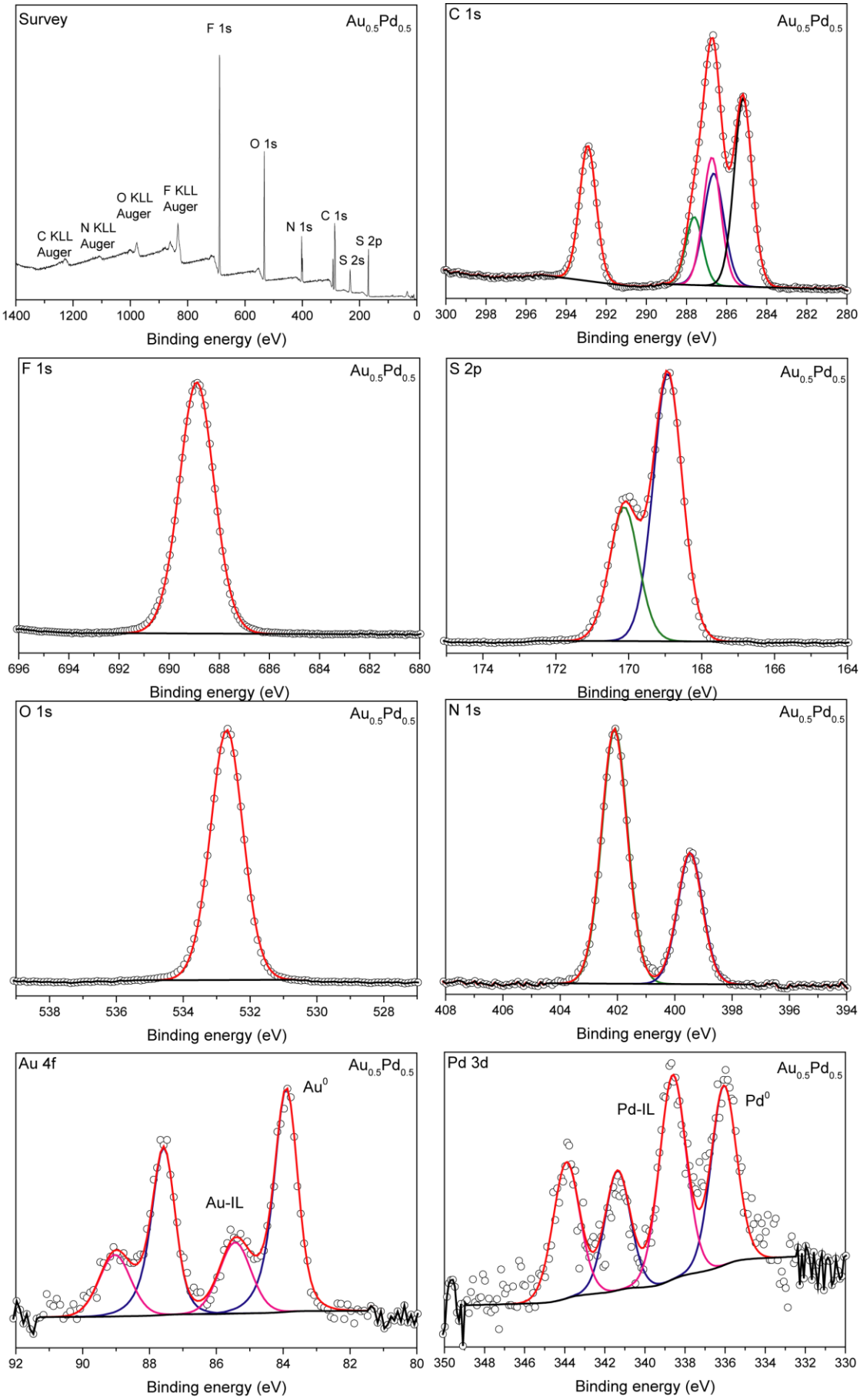
Survey
Au0.5Pd0.5
F 1s
O 1s
O KLL Auger
F KLL Auger
C KLL Auger
N KLL Auger
N 1s
C 1s
S 2p
S 2s
1400 1200 1000 800 600 400 200 0
Binding energy (eV)
C 1s
Au0.5Pd0.5
300 298 296 294 292 290 288 286 284 282 280
Binding energy (eV)
F 1s
Au0.5Pd0.5
696 694 692 690 688 686 684 682 680
Binding energy (eV)
S 2p
Au0.5Pd0.5
174 172 170 168 166 164
Binding energy (eV)
O 1s
Au0.5Pd0.5
538 536 534 532 530 528
Binding energy (eV)
N 1s
Au0.5Pd0.5
408 406 404 402 400 398 396 394
Binding energy (eV)
Au 4f
Au0.5Pd0.5
Au0
Au-IL
92 90 88 86 84 82 80
Binding energy (eV)
Pd 3d
Au0.5Pd0.5
Pd-IL
Pd0
350 348 346 344 342 340 338 336 334 332 330
Binding energy (eV)

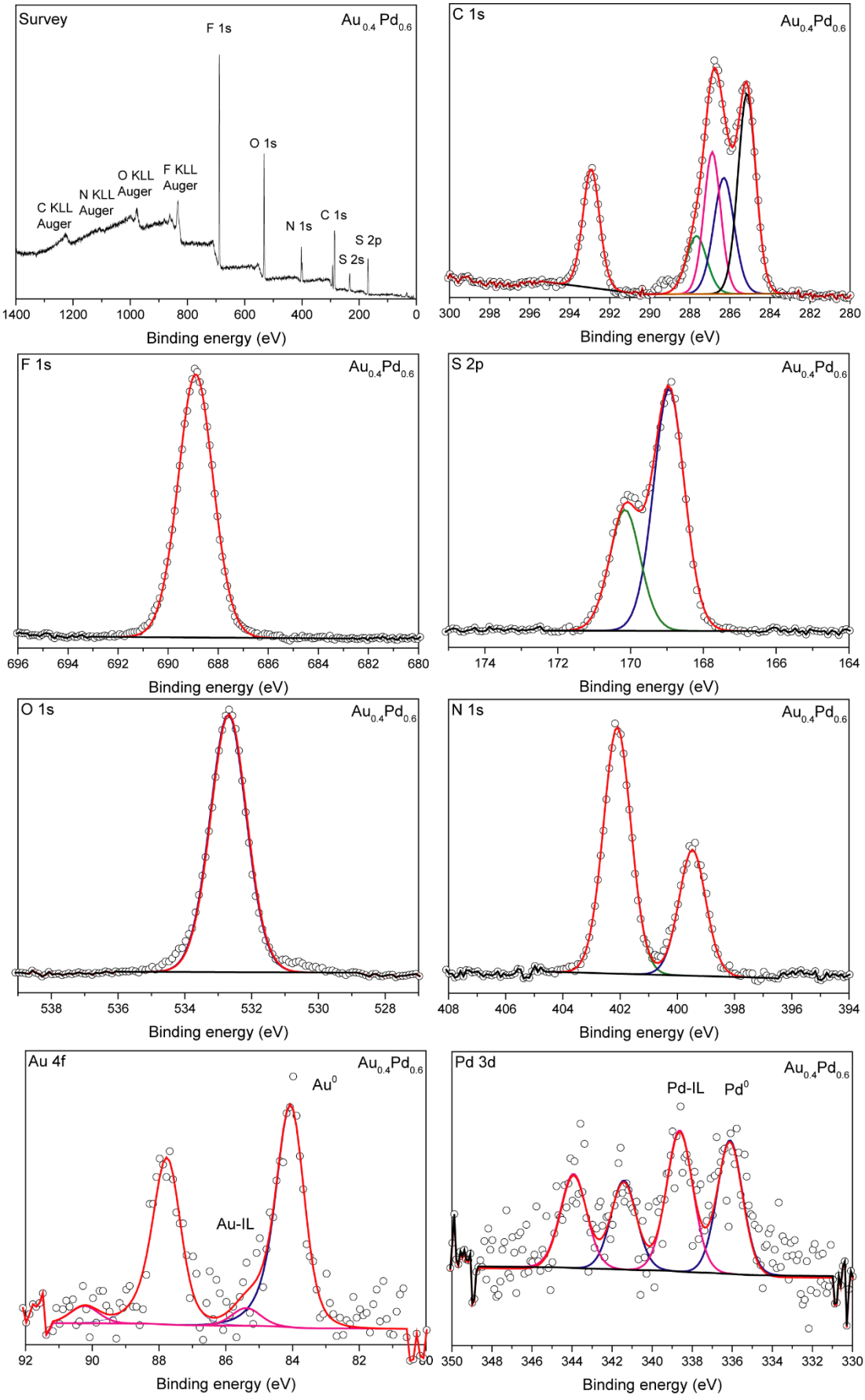
Survey
Au0.4 Pd0.6
F 1s
O 1s
O KLL Auger
F KLL Auger
N KLL Auger
C KLL Auger
N 1s
C 1s
S 2p
S 2s
1400 1200 1000 800 600 400 200 0
Binding energy (eV)
C 1s
Au0.4Pd0.6
300 298 296 294 292 290 288 286 284 282 280
Binding energy (eV)
F 1s
Au0.4Pd0.6
696 694 692 690 688 686 684 682 680
Binding energy (eV)
S 2p
Au0.4Pd0.6
174 172 170 168 166 164
Binding energy (eV)
O 1s
Au0.4Pd0.6
538 536 534 532 530 528
Binding energy (eV)
N 1s
Au0.4Pd0.6
408 406 404 402 400 398 396 394
Binding energy (eV)
Au 4f
Au0.4Pd0.6
Au0
Au-IL
92 90 88 86 84 82 80
Binding energy (eV)
Pd 3d
Au0.4Pd0.6
Pd-IL
Pd0
350 348 346 344 342 340 338 336 334 332 330
Binding energy (eV)

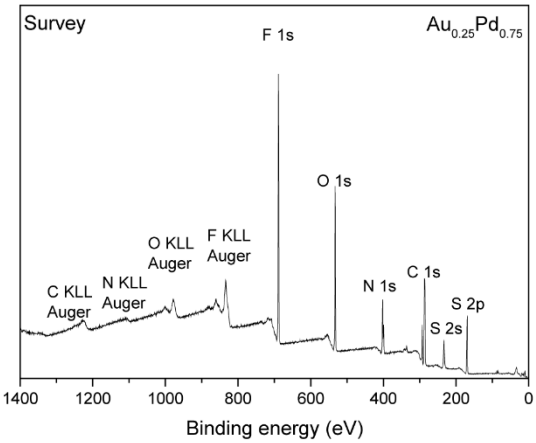
Survey
$Au_{0.25}Pd_{0.75}$
F 1s
O 1s
O KLL Auger
F KLL Auger
C KLL Auger
N KLL Auger
N 1s
C 1s
S 2p
S 2s
1400 1200 1000 800 600 400 200 0
Binding energy (eV)

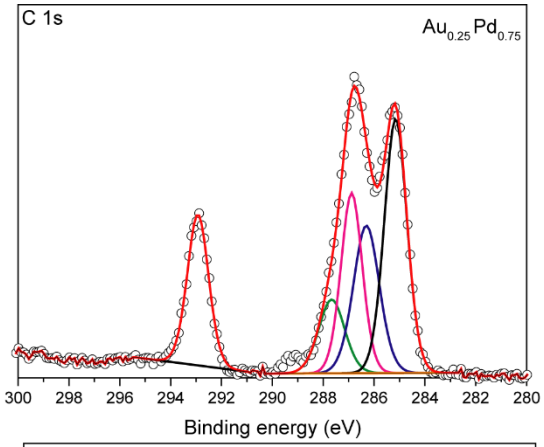
C 1s
$Au_{0.25}Pd_{0.75}$
300 298 296 294 292 290 288 286 284 282 280
Binding energy (eV)

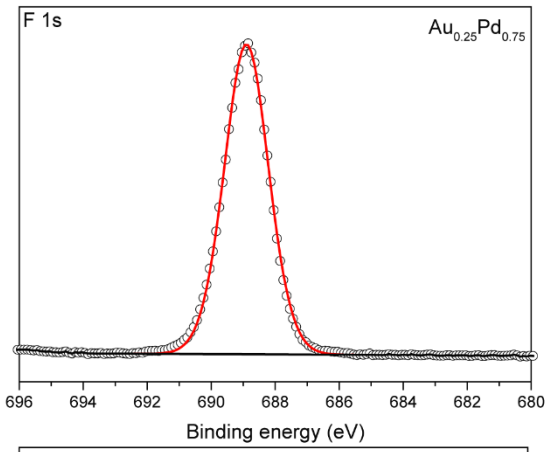
F 1s
$Au_{0.25}Pd_{0.75}$
696 694 692 690 688 686 684 682 680
Binding energy (eV)

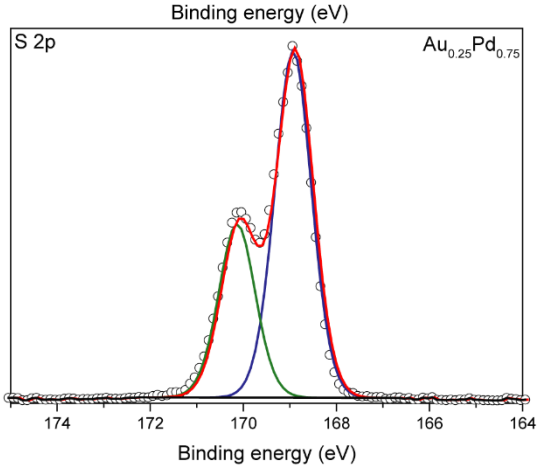
S 2p
$Au_{0.25}Pd_{0.75}$
174 172 170 168 166 164
Binding energy (eV)

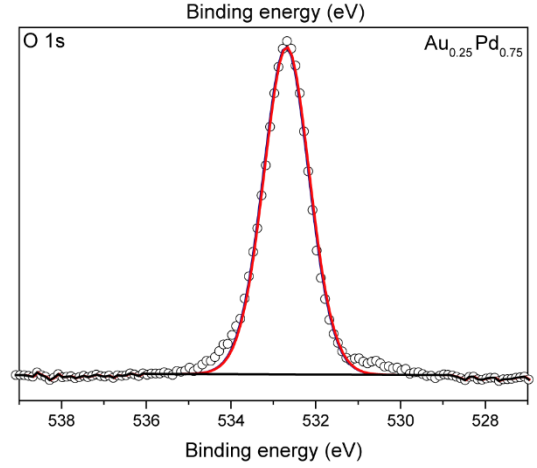
O 1s
$Au_{0.25}Pd_{0.75}$
538 536 534 532 530 528
Binding energy (eV)

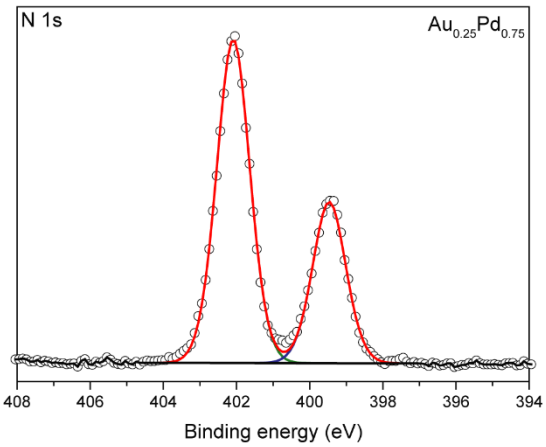
N 1s
$Au_{0.25}Pd_{0.75}$
408 406 404 402 400 398 396 394
Binding energy (eV)

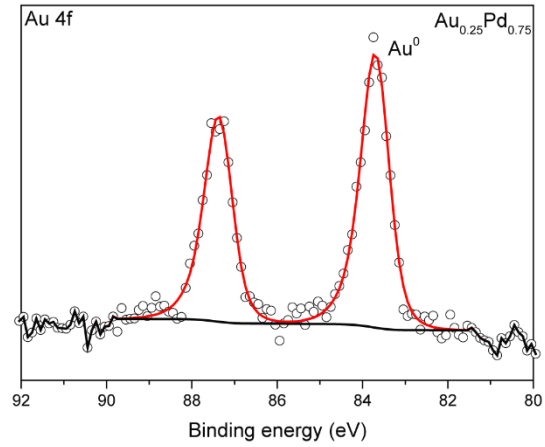
Au 4f
$Au_{0.25}Pd_{0.75}$
Au^0
92 90 88 86 84 82 80
Binding energy (eV)

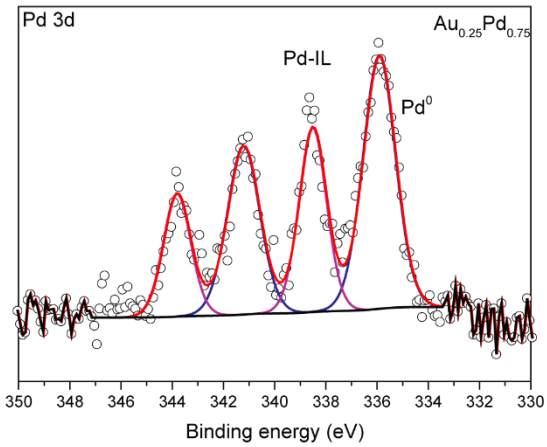
Pd 3d
$Au_{0.25}Pd_{0.75}$
Pd-IL
Pd^0
350 348 346 344 342 340 338 336 334 332 330
Binding energy (eV)

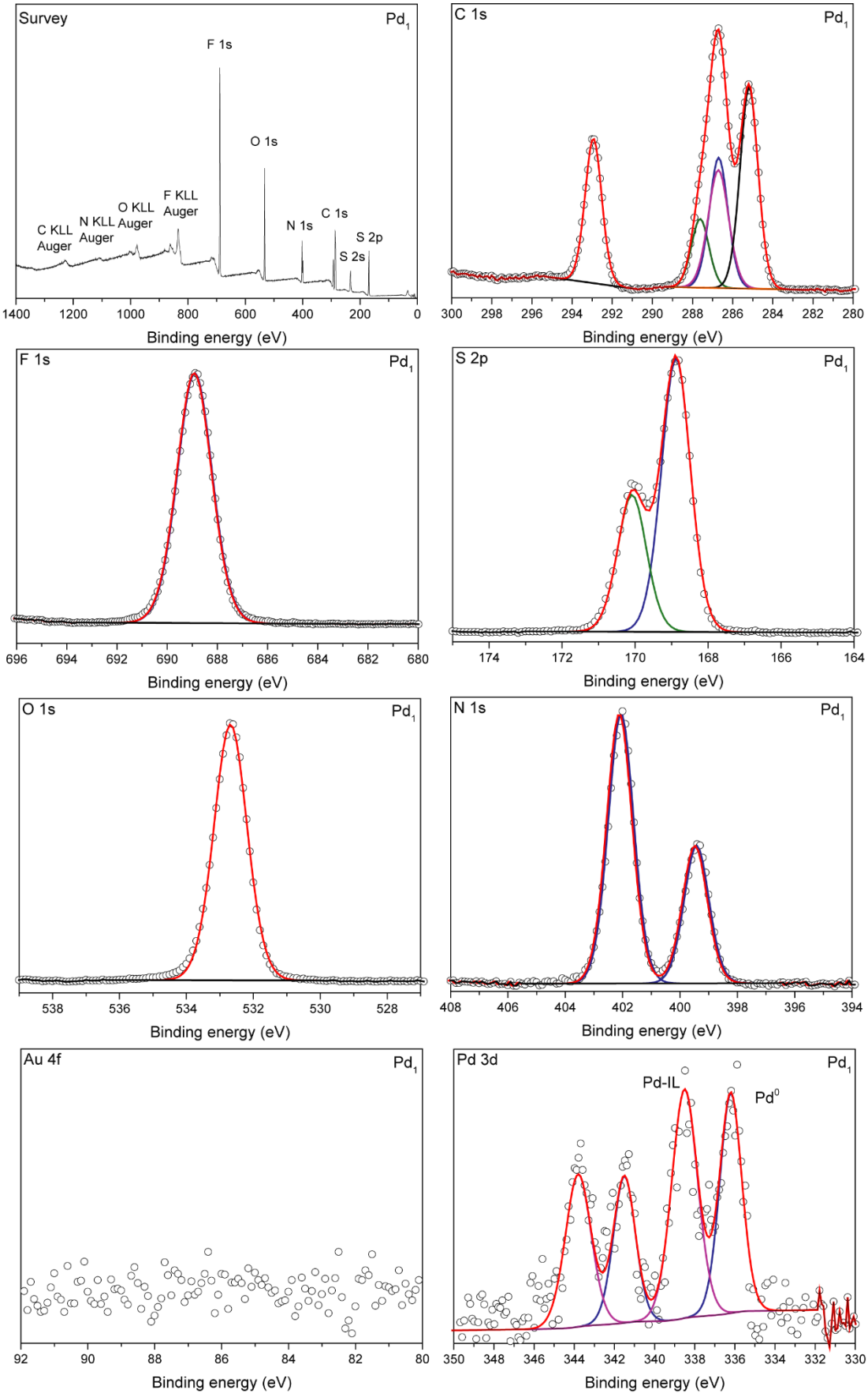
Survey
Pd1
F 1s
O 1s
C KLL Auger
N KLL Auger
O KLL Auger
F KLL Auger
N 1s
C 1s
S 2p
S 2s
1400 1200 1000 800 600 400 200 0
Binding energy (eV)
C 1s
Pd1
300 298 296 294 292 290 288 286 284 282 280
Binding energy (eV)
F 1s
Pd1
696 694 692 690 688 686 684 682 680
Binding energy (eV)
S 2p
Pd1
174 172 170 168 166 164
Binding energy (eV)
O 1s
Pd1
538 536 534 532 530 528
Binding energy (eV)
N 1s
Pd1
408 406 404 402 400 398 396 394
Binding energy (eV)
Au 4f
Pd1
92 90 88 86 84 82 80
Binding energy (eV)
Pd 3d
Pd1
Pd-IL
Pd0
350 348 346 344 342 340 338 336 334 332 330
Binding energy (eV)

Appendix 4

Catalyst	(%) Metal present		Au $4f_{7/2}$		Pd $3d_{5/2}$		F 1s	O 1s	S $2p_{1/2}$	S $2p_{3/2}$	N 1 S_{Cation}	N 1 S_{anion}	C_{NTf2}	$C_{2/core}$	$C_{6,7/hetero}$	$C_{4,5/inter}$	$C_{aliphatic}$
	Pd	Au	Au^0	Au-IL	Pd^0	Pd-IL											
Au_1	0	100	84.3	85.7	-	-	688.9	532.7	170	168.8	402	399.4	293	287.8	286.9	286.3	285.2
$Au_{0.8}Pd_{0.20}$	19	81	84.1	85.5	336	338.4	688.9	532.7	170.1	168.9	402.1	399.5	292.9	287.6	286.7	286.6	285.1
$Au_{0.5}Pd_{0.50}$	52	48	83.9	85.4	336.1	338.6	688.9	532.7	170.1	168.9	402.1	399.5	292.9	287.6	286.7	286.6	285.2
$Au_{0.4}Pd_{0.60}$	63	37	84	85.4	336.2	338.6	688.9	532.7	170.2	168.9	402.1	399.5	292.9	287.7	286.9	286.3	285.2
$Au_{0.25}Pd_{0.75}$	75	25	83.7	-	335.9	338.5	688.9	532.7	170.1	168.9	402.1	399.5	292.9	287.6	286.9	286.4	285.2
Pd_1	100	0	-	-	336.1	338.4	688.9	532.7	170.1	168.9	402.1	399.4	292.9	287.6	286.7	286.6	285.2

Table S7 – Binding energies (eV) for all the elements present in the AuPd NPs in IL, including simulated components for deconvoluted complex spectra.

Catalyst	(%) Metal present		Au $4f_{7/2}$		Pd $3d_{5/2}$		F 1s	O 1s	S $2p_{1/2}$	S $2p_{3/2}$	N 1 S_{Cation}	N 1 S_{anion}	C_{NTf2}	$C_{2/core}$	$C_{6,7/hetero}$	$C_{4,5/inter}$	$C_{aliphatic}$
	Pd	Au	Au^0	Au-IL	Pd^0	Pd-IL											
Au_1	0	100	0.9	0.9	-	-	1.6	1.3	0.9	0.9	1.1	1	1	1.2	0.9	1.2	1
$Au_{0.8}Pd_{0.20}$	19	81	0.9	1	1.5	1.5	1.6	1.2	0.9	0.9	1.1	1	1	1.2	1.2	1.2	1.1
$Au_{0.5}Pd_{0.50}$	52	48	0.8	1.1	1.7	1.6	1.6	1.1	0.9	0.9	1.1	1	1	1	1	1.2	1.1
$Au_{0.4}Pd_{0.60}$	63	37	1	1	1.5	1.7	1.6	1.3	1	1	1.1	1.1	1	1.2	1	1.2	1
$Au_{0.25}Pd_{0.75}$	75	25	0.8	-	1.5	1.3	1.6	1.2	0.9	0.9	1.1	1.1	1	1.1	1	1.2	1
Pd_1	100	0	-	-	1.4	1.3	1.6	1.2	0.9	0.9	1	1	1	1	1.2	1.1	1.1

Table S8 – FWHM (eV) for all the elements present in the AuPd NPs in IL, including simulated components for deconvoluted complex spectra.

Appendix 5

The calculations presented in figure 3.15 c) are produced by calculating the number of atoms in each NP. These calculations take into consideration the atomic radius and volume, the atomic percentage of each element in the NPs, assuming the formation of mixed metal NPs (alloy) with similar metal content as presented by the ICP-OES measurements and their spatial arrangement, or crystal structure in Face Centered Cubic (FCC). The atoms of each metal can be obtained and the percentage of surface atoms for each AuPd NPs in IL. Assuming the formation of a coreshell structure with an outer layer composed, favourably, of Pd atoms, a ratio of Pd atoms/surface atoms can be calculated, with a ratio > 1 indicating a complete outer shell of Pd atoms and the introduction of Pd atoms in the inner shell (Table S9). The ratio of Pd-Pd/Pd-IL interaction presented in figure 3.15 a) is obtained by the integration of the areas of the k3-weighted and Fourier transformed magnitudes of the EXAFS spectra for each of the AuPd NPs in IL at 1.5 Å and 2.5 Å for the Pd-IL bond distance and Pd-Pd bond distance, respectively (Figure S2).

Table S9 - Calculation of the surface atoms on the AuPd NPs in IL and the maximum number of Pd atoms in the outer shell of the NP assuming a face-centered cubic (fcc) and the migration of the Pd atoms to the outer layers of the NPs.

Sample	Size of particles (nm)	Atoms on the each NP	Atoms on surface	surface area atomic (%)	Pd atoms on NP	Au atoms on NP	Pd atoms/surface atoms	Pd %
Au_{100}	2.84	469	258	55	0	469	0.00	0
$Au_{80}Pd_{20}$	2.35	295	180	61	59	236	0.33	20
$Au_{50}Pd_{50}$	1.58	72	57	79	36	36	0.63	50
$Au_{40}Pd_{60}$	2.17	227	148	65	136	91	0.92	60
$Au_{25}Pd_{75}$	1.81	125	93	74	94	31	1.01	75
Pd_{100}	1.62	87	69	79	87	0	1.27	100

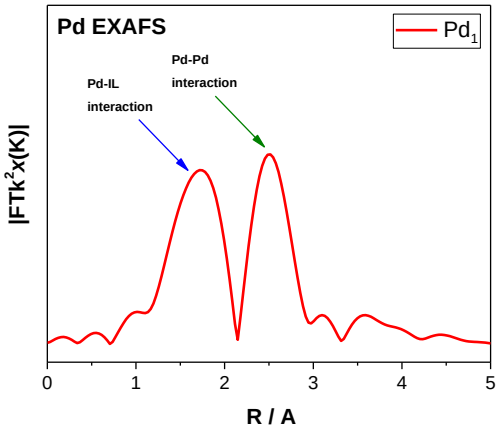

Figure S2 - k3-weighted and Fourier transformed magnitudes of the EXAFS spectra (|FT(k2χ(k))|) of the Pd K-edge of the Pd_1 sample.